THE PROGENITORS OF TYPE IIP SUPERNOVAE

Emma R. Beasor

A thesis submitted in partial fulfilment of the requirements of

Liverpool John Moores University

for the degree of

Doctor of Philosophy.

April 2019

Declaration

The work presented in this thesis was carried out at the Astrophysics Research Institute, Liverpool John Moores University. Unless otherwise stated, it is the original work of the author.

While registered as a candidate for the degree of Doctor of Philosophy, for which submission is now made, the author has not been registered as a candidate for any other award. This thesis has not been submitted in whole, or in part, for any other degree.

Emma R. Beasor
Astrophysics Research Institute
Liverpool John Moores University
IC2, Liverpool Science Park
146 Brownlow Hill
Liverpool
L3 5RF
UK

Abstract

Mass-loss prior to core collapse is arguably the most important factor affecting the evolution of a massive star across the Hertzsprung-Russel (HR) diagram, making it the key to understanding what mass-range of stars produce supernova (SN), and how these explosions will appear. It is thought that most of the mass-loss occurs during the red supergiant (RSG) phase, when strong winds dictate the onward evolutionary path of the star and potentially remove the entire H-rich envelope.

Uncertainty in the driving mechanism for RSG winds means the mass-loss rate ($\dot{M}$) cannot be determined from first principles, and instead, stellar evolution models rely on empirical recipes to inform their calculations. At present, the most commonly used $\dot{M}$-prescription comes from a literature study, whereby many measurements of mass-loss were compiled. The sample sizes are small ($<$10 stars), highly heterogeneous in terms of mass and metallicity, and have very uncertain distances from observations and analysis techniques that at best provide order-of-magnitude estimates compared to what is possible today. The relation itself contains large internal scatter, which could be the difference between a star losing its entire H-envelope, or none of it at all. More modern efforts to update the RSG mass-loss rate prescription rely on samples which suffer from statistical biases, for example by selecting objects based on mid-IR brightness or circumstellar maser emission, and hence are inevitably biased towards higher mass-loss rate objects.

It is the aim of this thesis to overhaul our understanding of RSG mass-loss. By selecting RSGs in clusters, where the initial mass and metallicity are known, I will be able to observe how mass-loss changes as the star approaches SN and compare this to

what is currently implemented in stellar evolutionary models. Ultimately, I will measure $\dot{M}$ values and luminosities for RSGs in 5 different clusters of varying ages, thus targeting RSGs of different initial masses. I will then combine these mass-loss rate-luminosity relations to derive a new initial mass-dependent mass-loss rate, which can be implemented into stellar evolutionary models.

Publications

In the course of completing the work presented in this thesis, the following papers have been submitted for publication in a refereed journal:

1. *The evolution of red supergiants to supernova in NGC 2100*

   Beasor, E. R. & Davies, B. , 2016, MNRAS, 463, 1269

2. *Red Supergiants as Cosmic Abundance Probes: Massive Star Clusters in M83 and the Mass-Metallicity Relation of Nearby Galaxies*

   Davies, B., Kudritzki, R. P., Lardo, C., Bergemann, M., **Beasor, E. R.,** Plez, B., Evans, C., Bastian, N., Patrick, L., 2017, ApJ, 847, 112

3. *The evolution of red supergiant mass loss rates*

   Beasor, E. R. & Davies, B. , 2018, MNRAS, 475, 55

4. *The initial masses of the red supergiant progenitors to Type II supernovae*

   Davies, B. & **Beasor, E. R.**, 2018, MNRAS, 474, 2116

5. *The luminosities of cool supergiants in the Magellanic Clouds, and the Humphreys-Davidson limit revisited*

   Davies, B., Crowther, P. J., **Beasor, E. R.,** 2018, MNRAS, 478, 3138

6. *A critical re-evalution of Thorne-Żytkow Object candidate HV 2112*

   Beasor, E. R., Davies, B., Cabrera-Ziri, I., Hurst, G., 2018, MNRAS, 479, 3101

7. *Age discrepancies in young clusters; evidence for mergers?*

   Beasor, E. R., Davies, B., Smith, N., Bastian, N., 2019, MNRAS

8. *The distances to star-clusters hosting Red Supergiants; χ Per, NGC 7419 and Weesterlund 1*

   Davies, B. & **Beasor, E. R.,** 2019, MNRAS

Acknowledgements

I want to begin by thanking my supervisor, Ben Davies, for providing such an interesting project in the first place and for unwavering support since then. I've had a fair few wobbles throughout the PhD and you always knew the right moments to push me and the right moments to say "lets get a coffee". I feel lucky to have come out of this process with not only a great scientific collaborator, but a great friend.

Not forgetting of course many other members of staff at the ARI, in particular Nate Bastian, Phil James and Steve Longmore, who were always willing to read drafts, write references and run mock interviews. A huge thanks also has to go to all my friends in the department, especially Ted, Lawrence and Ashley. Thanks for all the laughs fellas.

Next, I thank my parents for always believing in me and supporting me, and for providing good roasts whenever I've needed them.

Finally, Caela. Thanks for all the silliness and for being the person who makes me laugh the most in the world. I truly couldn't have done this without you.

Contents

List of Tables

List of Figures

Chapter 1

Introduction

Red supergiants (RSGs) are the end point in evolution for massive stars with initial masses of between $\sim$8 – 25 $M_{\odot}$ before they end their lives as core collapse supernovae[1]. The enriched material expelled from the dying star enriches the interstellar medium and drives subsequent galaxy evolution, ultimately determining many fundamental observational properties, including the mass-metallicity relation (e.g. Zahid et al., 2014) and the low-mass end of the galaxy mass function (e.g. Crain et al., 2017). Large scale cosmological simulations of galaxies require knowledge of the supernova (SN) rate (the number of SN per unit mass of star formed per unit time) which itself is derived from stellar evolutionary theory. Crucially, it is imperative we know the evolutionary end-state of massive stars as a function of their initial mass in order to predict whether or not they will produce a SN, and if they do, what kind of SN (i.e. H-rich or H-poor). It is the aim of this thesis to improve our understanding of how massive stars end their lives by focusing on their mass-loss behaviour prior to death. In the following section, I will summarize the evolution of massive stars before discussing the impact mass-loss can have on a star's evolutionary path.

[1]There is some evidence that some stars within this mass range may end their lives by collapsing directly to black holes with no supernova event, e.g. Kochanek et al. (2008), but the rate of this is unclear.

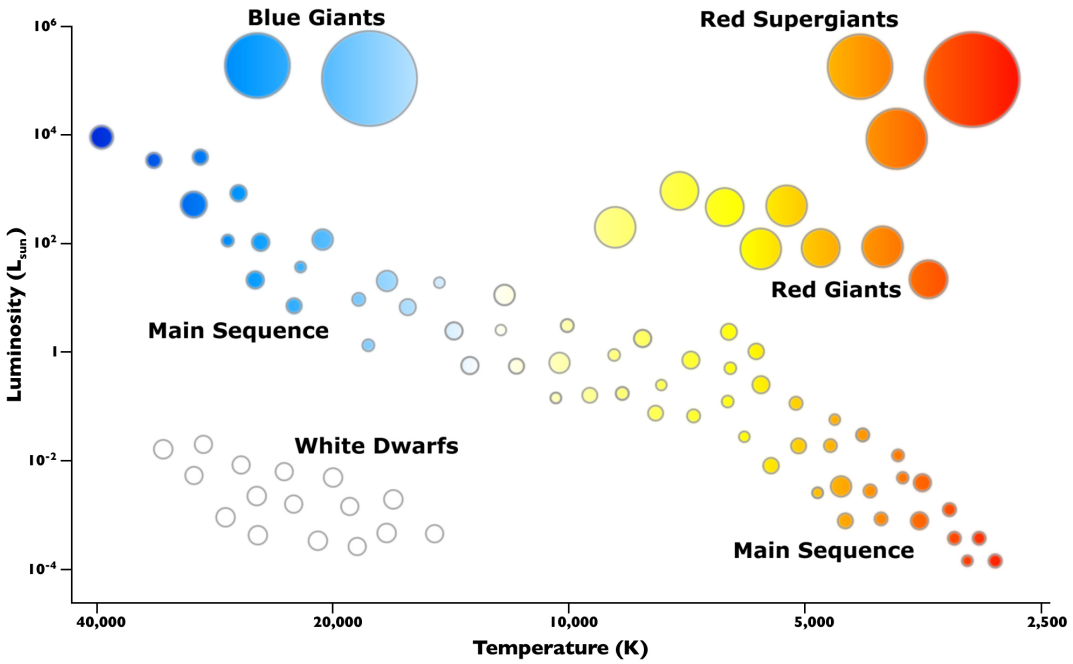

Figure 1.1: A simplified HRD. Taken from http://lcogt.net/spacebook/h-r-diagram/

1.1 Massive star evolution

An early step in understanding stellar evolution came from the creation of the Hertzsprung-Russell diagram (HRD), in which the effective temperature of a star ($T_{\rm eff}$) is plotted against its luminosity ($L_{\rm bol}$), clearly showing that stars tend to sit in well defined groups (see Fig. 1.1 for an example). Stars spend the majority of their lives on the Main Sequence (MS) before the core hydrogen is exhausted, and the exact time spent here depends on the initial mass of the star. For intermediate and low mass stars ($M_{\rm ini}$<$8M_{\odot}$), MS lifetime is on the order of 10^8yrs, while for high mass stars ($M_{\rm ini}$>$8M_{\odot}$) the MS lifetime is shorter, with MS lifetimes for the highest mass stars being on the order of 10^7 yrs (Meynet et al., 2015). RSGs occupy the upper right region of the HR diagram, as some of the most luminous objects in the Universe. Indeed, at infrared wavelengths RSGs dominate the flux output of young clusters and galaxies (Gazak et al., 2014).

1.1.1 Core Evolution

Early studies of massive star evolution (e.g. Stothers & Chin, 1968; Stothers, 1969) showed that a star's position on the HR diagram can shed light on the interior structure of the star. Under the assumption the outer convective envelope of the star does not mix with the layers below, early models (Stothers & Chin, 1968) suggested that the RSG phase is where core helium burning is initiated. Since then, much progress has been made on the study of RSGs, with many stellar models focusing on the evolution of massive stars (e.g. Meynet et al., 1994; Georgy et al., 2013; Ekström et al., 2012; Brott et al., 2011). I now will describe the current understanding of the evolution of a massive star ($M_{\rm ini} > 8M_{\odot}$) from MS to SN.

Throughout the MS a star undergoes hydrogen fusion within the convective core, generating energy and helium. Once the H core is exhausted, due to the efficient convective mixing, the entire core is depleted of its fuel almost instantaneously (compared to the contraction/expansion timescale). From here, the evolutionary path followed by a massive star differs greatly to the path followed by a lower mass star. Without core H fusion, the core of the star contracts, causing the envelope to expand via the mirror principle. The effective and surface temperatures of the star decrease, crossing the HRD, through the 'Yellow Void' to join the RSG branch. Lower mass stars tend to cross the HRD more quickly than higher mass stars, but the exact crossing timescale depends on many factors, including metallicity, convection, mass-loss and the treatment of mixing. For stars at the lower end of the RSG initial mass range ($\sim 8M_{\odot}$), the evolution towards the RSG branch happens on a thermal timescale, which for a typical RSG is $\sim 10^3 - 10^4$yrs. Since this timescale is extremely short compared to the lifetime of the star, virtually no energy is lost during this time, and the expansion of the envelope is almost adiabatic. The luminosity of these stars decreases during the red-ward evolution. As the star does work converting thermal energy into potential energy, it gets fainter while it is expanding. This reduction in luminosity can be seen in evolutionary tracks, for example see the $9M_{\odot}$ track in Fig 1.2 (Meynet & Maeder, 2003; Ekström et al., 2012). The star then returns to a luminosity comparable to that when it left the MS, and continues to get brighter as the He core mass grows. For the

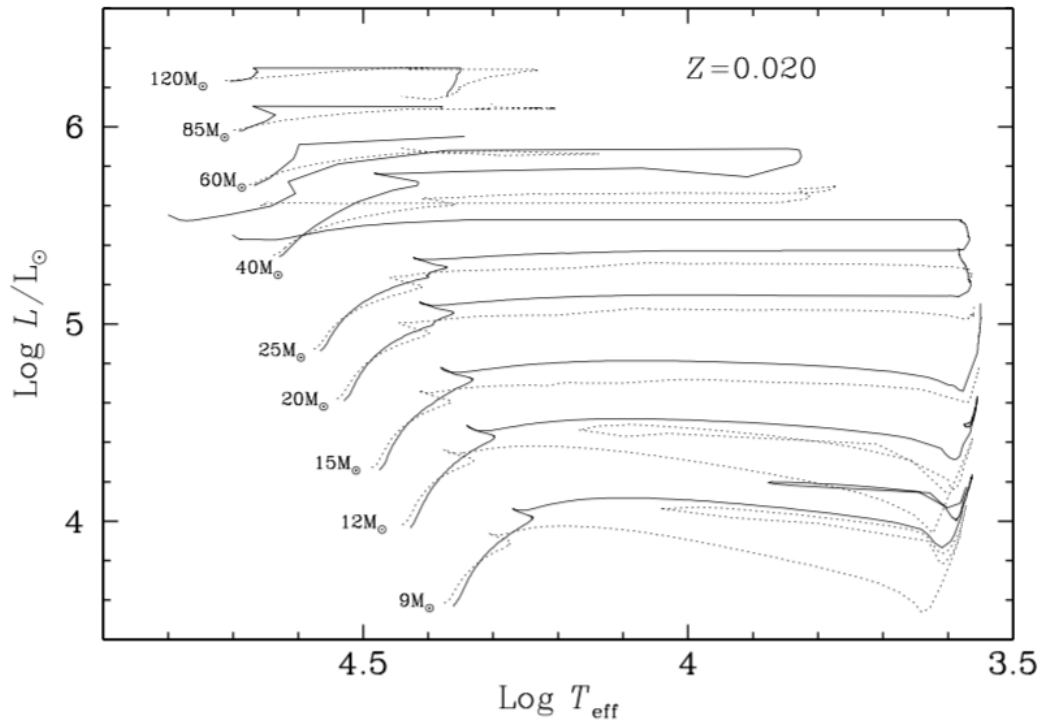

Figure 1.2: Evolutionary tracks for rotating and non-rotating models at Z = 0.020 (Meynet & Maeder, 2003).

higher mass stars, see e.g. the $20M_{\odot}$ track in Fig. 1.2, the expansion is slower than for the lower mass stars and He burning begins in the blue phase.

The star has now smoothly transitioned to He burning[2], and is made up of a He burning core surrounded by a radiative H-burning shell and a highly convective envelope. Eventually, the He in the core is depleted, leaving a convective C-burning core surrounded by He and H shells in the radiative zone above the core. This process continues, with nuclear burning in the core fusing successively heavier metals in short lived phases. The final stage is when the core has fused to become inert iron, and further nuclear fusion can no longer take place. At this point, the star can no longer support itself against gravitational collapse and the outer layers of the star crash onto the core producing a supernova.

[2]unlike for lower mass stars ($<8M_{\odot}$) there is no Helium flash as the core is not degenerate

1.1.2 Effect of mass-loss on evolution

Mass-loss prior to and during the RSG phase has significant effects on the onward evolution of a star. For stars with initial masses greater than $60M_{\odot}$, the mass-loss rates can be significant enough that a large fraction of the outer envelope is removed during the MS[3]. Thus, without enough envelope left to swell up, the most massive stars do not undergo an RSG phase (e.g. Stothers & Chin, 1968, 1978) and instead remain in the blue region of the HR diagram, as either blue supergiants (BSGs) or luminous blue variables (LBVs). This in turn means that high mass-loss on the MS causes a maximum possible luminosity for RSGs, this is discussed in greater detail in Section 1.2.

The final fate of stars that do experience an RSG phase is largely driven by mass-loss during this time. As demonstrated by Maeder (1981), in the case of no mass-loss, a star of $60M_{\odot}$ reaches the RSG phase and remains there until SN, whereas even moderate mass-loss causes a blueward motion in the HR diagram by removing the H-rich envelope. This is shown in a Kippenhahn diagram in Fig. 1.3, taken from Maeder (1981). The star undergoes a brief RSG phase before the stellar winds peel away the envelope and leave a WR star (between ages of log(6.8)yrs and log(6.9)yrs in the diagram) which in turn will end its life as a H-poor SN.

For lower mass RSGs, their mass-loss rates are not thought to be high enough to remove the envelope (e.g. Maeder, 1981; Meynet & Maeder, 2003) and instead these stars remain in the RSG phase until SN. Despite the brevity of the RSG phase ($\sim$$10^6$yrs, e.g. Georgy et al., 2013) the high mass-loss rates mean that a substantial fraction of the envelope may be lost during this phase, affecting the stars final position on the HR diagram. Many studies have explored the effect of increasing mass-loss during the RSG phase by arbitrary amounts for lower mass stars(e.g. Meynet et al., 1994; Georgy, 2012). This is of particular importance for predicting what mass-range of star will explode in the RSG phase, see Section 1.3.2.

[3]Note that at extremely low metallicities mass-loss can be so weak that even the highest mass stars ($>60M_{\odot}$) do not lose much mass on the MS.

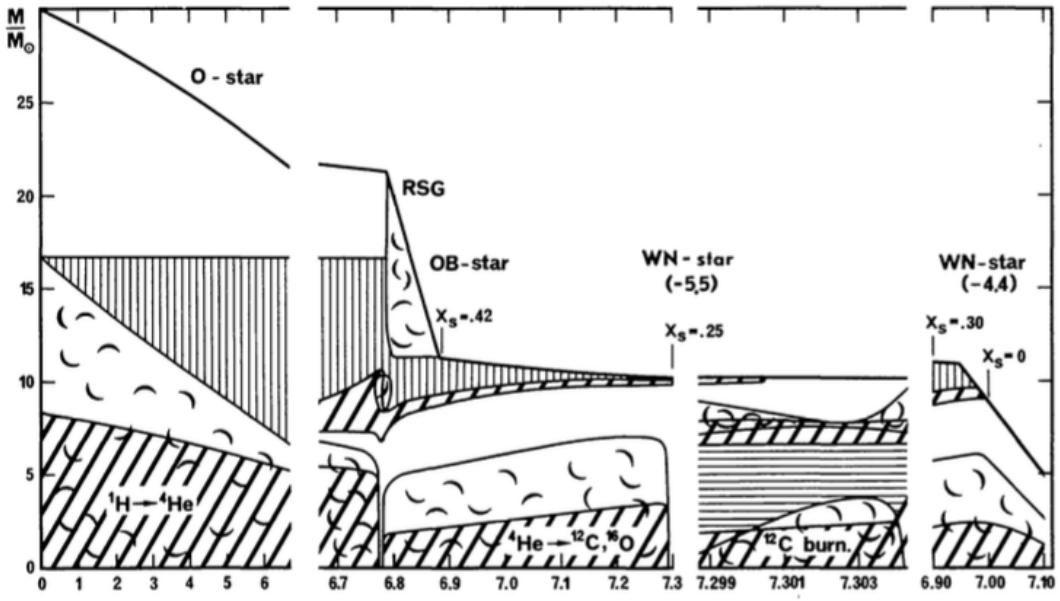

Figure 1.3: Kippenhahn diagram for a $30M_{\odot}$ star undergoing strong mass-loss, taken from Maeder (1981). In this diagram the cloudy regions represent fully convective zones, diagonal hatched zones represent areas of nuclear burning where the energy production rate is high and vertical hatched zones represent convectively mixed zones.

1.2 Observations I: The Humphreys-Davidson Limit

An important empirical constraint on massive star evolution comes from the maximum observed luminosity limit for RSGs. This upper limit for the luminosities ($L_{\rm max}$) of RSGs has long been observed (e.g. Stothers, 1969; Sandage & Tammann, 1974), and later was termed the Humphreys-Davidson (H-D) limit (Humphreys & Davidson, 1979). In Humphreys & Davidson (1979) and Humphreys (1983) the observed HR diagrams for supergiants in the Galaxy, Large Magellanic Cloud (LMC) and Small Magellanic Cloud (SMC) were compared (see Fig. 1.4), finding that while distribution of spectral types differed (stars evolve to earlier spectral types at lower metallicities), the luminosities for each galaxy were comparable, with a maximum observed luminosity limit of $\log(L/L_{\odot})$= 5.8.

Humphreys & Davidson (1979) proposed that the maximum luminosity threshold for supergiants is determined by the mass-loss a star experiences during its lifetime, via strong winds or eruptive mass-loss episodes, such as those seen for luminous blue

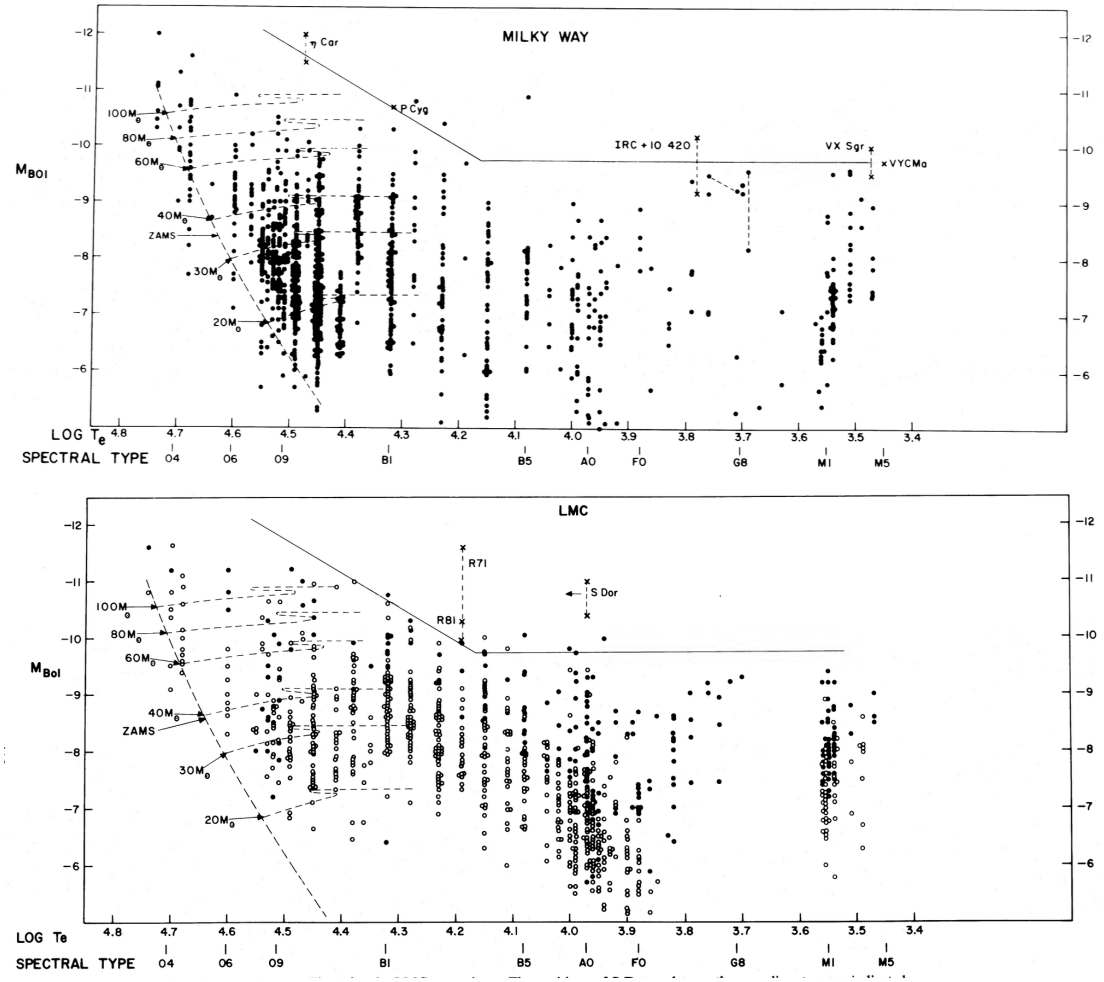

Figure 1.4: *Top panel:* Figure showing the bolometric magnitudes for stars in the Milky Way across spectral types O to M. The solid line defines the approximate maximum brightness for supergiants. *Bottom panel:* same as above but for LMC stars. Taken from Humphreys & Davidson (1979)

variables (LBVs). As mass-loss rate depends on the initial mass of the star, above some initial mass the winds are strong enough that the H-envelope is removed by the time the star leaves the MS. These objects remain on the blue side of the HRD, becoming Wolf-Rayet (WR) stars. Thus, strong mass-loss prevents the highest initial mass stars from becoming RSGs, causing the observed maximum luminosity.

To calculate $L_{\max}$ Humphreys & Davidson used optical photometry and converted to a bolometric magnitude using a V-band bolometric correction (BC_V). For RSGs in particular, using the V-band magnitude to select objects may result in the dust enshrouded stars (such as those studies in Van Loon et al. (2005)) having their luminosities under-

estimated. In the most extreme cases, heavily dust enshrouded objects may be totally extinguished at optical wavelengths and hence be missed from the sample altogether. Further uncertainty comes from the assumed bolometric corrections for RSGs, difficulty in estimating the distances to Galactic RSGs and an outdated distance modulus to the LMC, all of which create large systematic uncertainties on $L_{\rm max}$.

The H-D limit was revisited in Davies et al. (2018), this time focusing solely on the Small and Large Magellanic Clouds (MCs), for which the distances are better constrained than for Galactic RSGs (Pietrzyński et al., 2013). Using a more complete data set and calculating $L_{\rm bol}$ by using the entire SED for each star, Davies et al. (2018) found that value of $L_{\rm max}$ is in fact lower than proposed by Humphreys & Davidson (1979), at around $\log(L/L_{\odot})$= 5.5. This result suggests that single-star models dramatically over predict the number of RSGs at the highest luminosities.

Stellar winds may provide a plausible explanation for this reduction in $L_{\rm max}$. Stronger winds during the MS would allow lower mass stars to peel off their envelopes before reaching the RSG phase, thus reducing $L_{\rm max}$. An increase in mass-loss during the RSG phases themselves would reduce the amount of time a star of a given initial mass would spend in this phase of evolution, as strong winds drive evolution back to the blue. Shorter lifetimes in the RSG phase would reduce the number of objects observed in this region, and again reduce $L_{\rm max}$. However, later in this thesis I will show that increasing mass-loss during the RSG phase has little empirical justification, see Chapters 2,3 and 5. Davies et al. (2018) speculated that a short period of enhanced mass-loss in the final 10^4yrs of a star's life could remove a significant fraction of the total mass, see Section 5.5 for further discussion.

1.3 Observations II: Type IIP Progenitors

Another observational constraint on the evolutionary path followed by massive stars comes from observations of SN progenitors. Specifically, SN have been observed with long plateau light curves (known as IIP SNe), indicative of the core collapse of a pro-

genitor with an extended hydrogen envelope (e.g. Doggett & Branch, 1985). When an explosion site has been imaged prior to SN (e.g. see Fig. 1.5) it is possible to directly confirm SN progenitors and estimate their final luminosities. Smartt et al. (2004) were the first to directly confirm an RSG progenitor to a Type IIP SN, and since then, there have been 14 confirmed RSG progenitors (e.g. Maund et al., 2011; Fraser, 2016).

Once progenitors have been detected in pre-explosion imaging, their masses may be estimated (see later). The next logical step is to compare observed masses to evolutionary predictions. Stellar evolutionary models predict that RSGs with masses between 8-25$M_{\odot}$ will end their lives as Type IIP SN (Meynet & Maeder, 2003; Ekström et al., 2012). Above this mass, stars are expected to evolve back to the blue and die as H-poor SN (e.g. Type Ibc). The first attempt to analyse progenitors in the framework of stellar evolution was in Smartt et al. (2009), later updated in Smartt (2015). Smartt et al. undertook a 10.5-yr, volume limited study (28 Mpc) in which they searched for SNe progenitor stars to further understand what kind of progenitors produce which types of SNe. From this work, the authors argued that there were no progenitors in the higher end of the predicted mass range, with a maximum initial mass cut off of 17$M_{\odot}$. Figure 1.6 shows the most likely minimum and maximum initial mass observed for the SN progenitors in the Smartt et al. (2009) study. These results challenged the predictions made by stellar evolutionary theory at the time (Meynet & Maeder, 2000; Meynet & Maeder, 2003), implying a maximum $\log(L/L_{\odot})$ for RSGs of $\sim$5.2 with stars above this luminosity ending their lives in a different region of the HR diagram (and hence as different type of SN). This friction between observations and theory was termed 'the Red Supergiant Problem'.

1.3.1 The Red Supergiant Problem

One natural question that arises from the Smartt et al. (2009) study was, what is the fate of the massive RSGs between 17 and 25M$_{\odot}$?

Smartt et al. suggested that the vast majority of stars above 17M$_{\odot}$ could collapse to form black holes with either very faint SNe or no explosion at all. Since, many

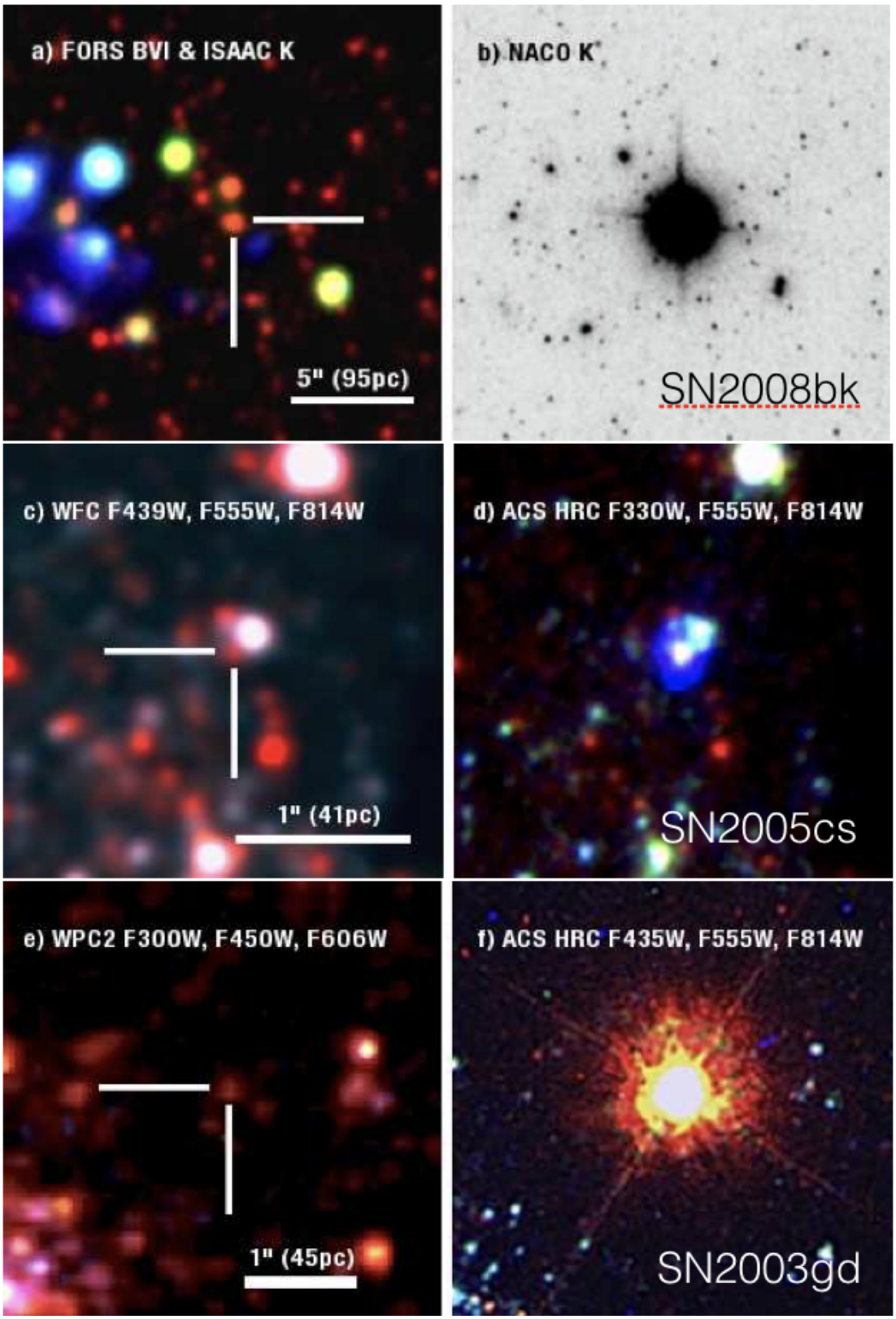

Figure 1.5: Pre-explosion images for 3 SN taken from Smartt (2015).

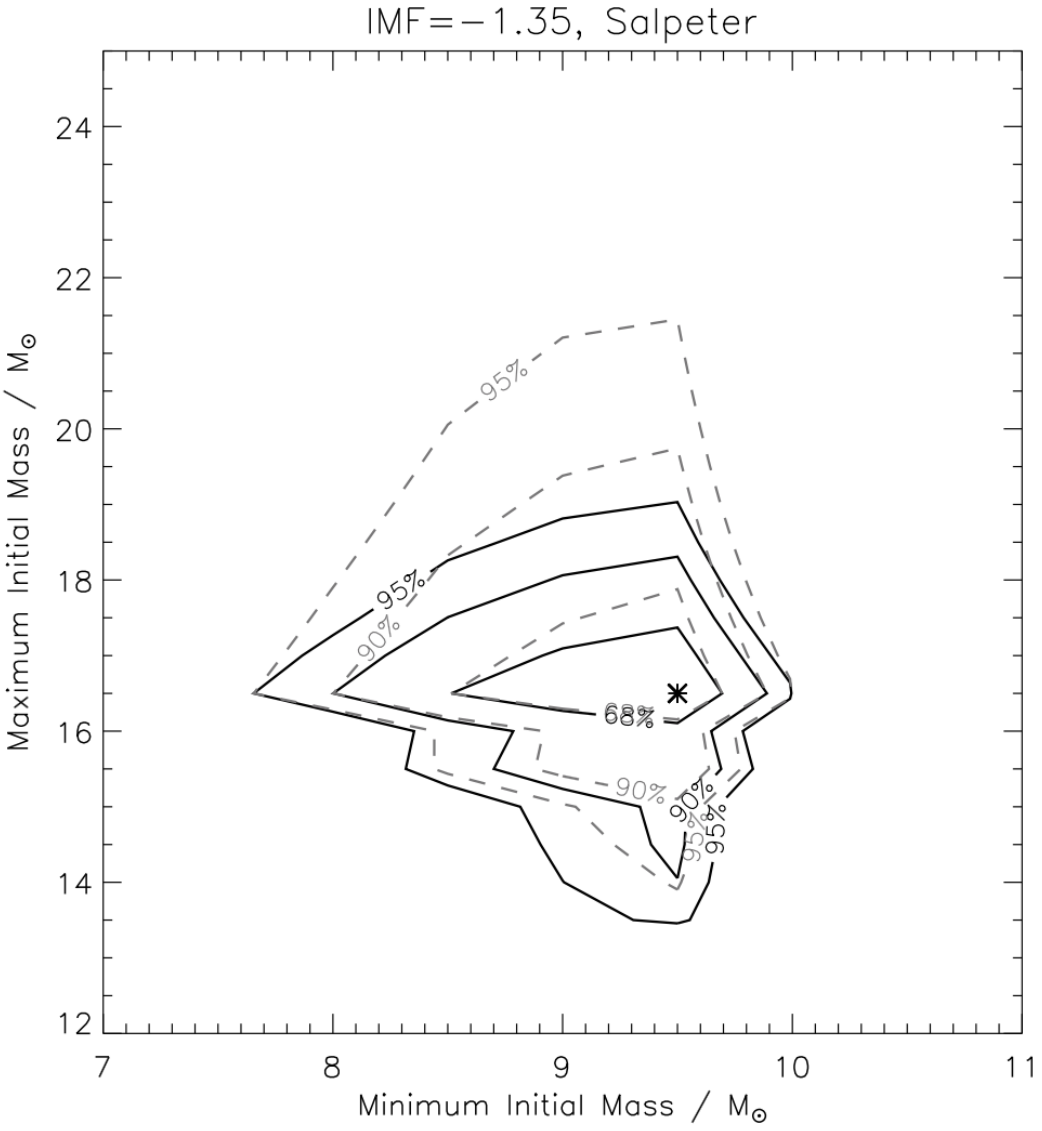

Figure 1.6: Figure showing the range of possible initial masses for Type IIP SN progenitors from Smartt et al. (2009). The contours show the 68%, 90% and 95% confidence limits.

studies have attempted to follow up on this suggestion by searching time-resolved survey data for stars which disappear with no SN (Kochanek et al., 2008; Gerke et al., 2015). At present only 2 promising candidates have been identified (Reynolds et al., 2015; Adams et al., 2017) with all other candidates suggested by Gerke et al. (2015) remaining inconclusive.

It was also discussed whether or not the 'missing' progenitor stars could have exploded as other types of SN; II-n, II-b and II-L. The fraction of stars born with high masses (between 17 and 25$M_{\odot}$) is comparable to the combined rate of II-L, IIn and IIb SNe suggesting a possible link (Smartt et al., 2009). There have indeed been observations of high mass progenitors for Type IIn SNe (e.g. Smith et al., 2011), however Smartt (2015) argues the rate of IIn SN is still not high enough to account for the missing progenitors. More recently there is growing evidence that rather than existing as discrete categories, II-L, II-P and II-n SN are more of a continuum. For example Smith et al. (2015) showed that SN PTF11iqb, originally classified as a IIn, was in fact the explosion of an RSG progenitor undergoing mass-loss. The early spectrum of the SN showed WR features, before these features weakened and the light curve became more typical of a IIL or IIP SN. As yet, there is no consensus on the true nature of the progenitor to this SN.

Circumstellar dust has also been considered as a possible solution to the RSG problem. Walmswell & Eldridge (2012) suggested that by failing to take into account the additional extinction resulting from RSG winds, the luminosity of the most massive red supergiants at the end of their lives is underestimated. Extra extinction around a star will cause it to appear dimmer, and hence a lower luminosity will be inferred. As mass estimates are based on mass-luminosity relations, a lower inferred luminosity would result in initial mass being under estimated. While Smartt et al. did provide extinction estimates of nearby supergiants and of the SN itself throughout their paper, only foreground extinction was taken into account, which have been shown to be underestimates (Maund, 2017). A plausible suggestion is that if RSG were to produce extra dust local to the star, this would be destroyed in the SNe. It is known that RSG form dust in their winds and infrared interferometry has shown that this dust can lie very close to

the star itself (Danchi et al., 1994). However, Kochanek et al. (2014) argued that even when the optical depth of the dust shell is high, a high enough fraction of the photons scattered within the dust layer are scattered back into the line of sight. Thus, for all but very high optical depths, the net reduction in observed luminosity is small.

From a stellar evolutionary theory point of view, tweaking the mass-loss can result in a lower predicted $L_{\rm max}$ for RSGs. The effects of substantially increasing $\dot{M}$ by factors of 10 or more have long been shown to have significant effects on the evolutionary path followed by massive stars (e.g. Georgy, 2012, as discussed earlier). More recent attempts to reconcile the RSG problem have involved increasing $\dot{M}$ during the RSG phase by factors of 3, 5 and 10 (see Figure 1.7, Georgy, 2012). Indeed, the end points of the $15M_{\odot}$ track with $\dot{M}$ increased by a factor of 10 agree well with observations of some yellow supergiant (YSG) progenitors. Georgy (2012) suggest that while enhanced mass-loss during the RSG phase may not be universal, a combination of standard and enhanced $\dot{M}$ can reproduce observations of the maximum mass of RSG progenitors as well as the reduced HD limit. However, throughout this thesis I will show that the observational case for enhanced $\dot{M}$ through the RSG phase is weak.

1.3.2 A possible resolution to the red supergiant problem?

Observational constraints on the mass range of Type IIP progenitors are vital to better inform stellar evolutionary models. However, the process of determining initial masses itself has a number of associated uncertainties. As the majority of progenitor detections are either single-band or upper limits from non-detections, the magnitude is converted to a bolometric luminosity using a bolometric correction (BC). In Smartt et al. (2009) the BCs used were those of Levesque et al. (2005). Smartt et al. used a spectral type range of M0$\pm$3 subtypes, stating this range is appropriate for a typical RSG, to estimate $L_{\rm bol}$. This luminosity is in turn used to find an initial mass for the progenitor, using a mass-luminosity relation from stellar evolutionary models. The process of converting a pre-explosion magnitude to an initial mass involves several steps (extinction correction, bolometric correction, mass-luminosity relation), all of

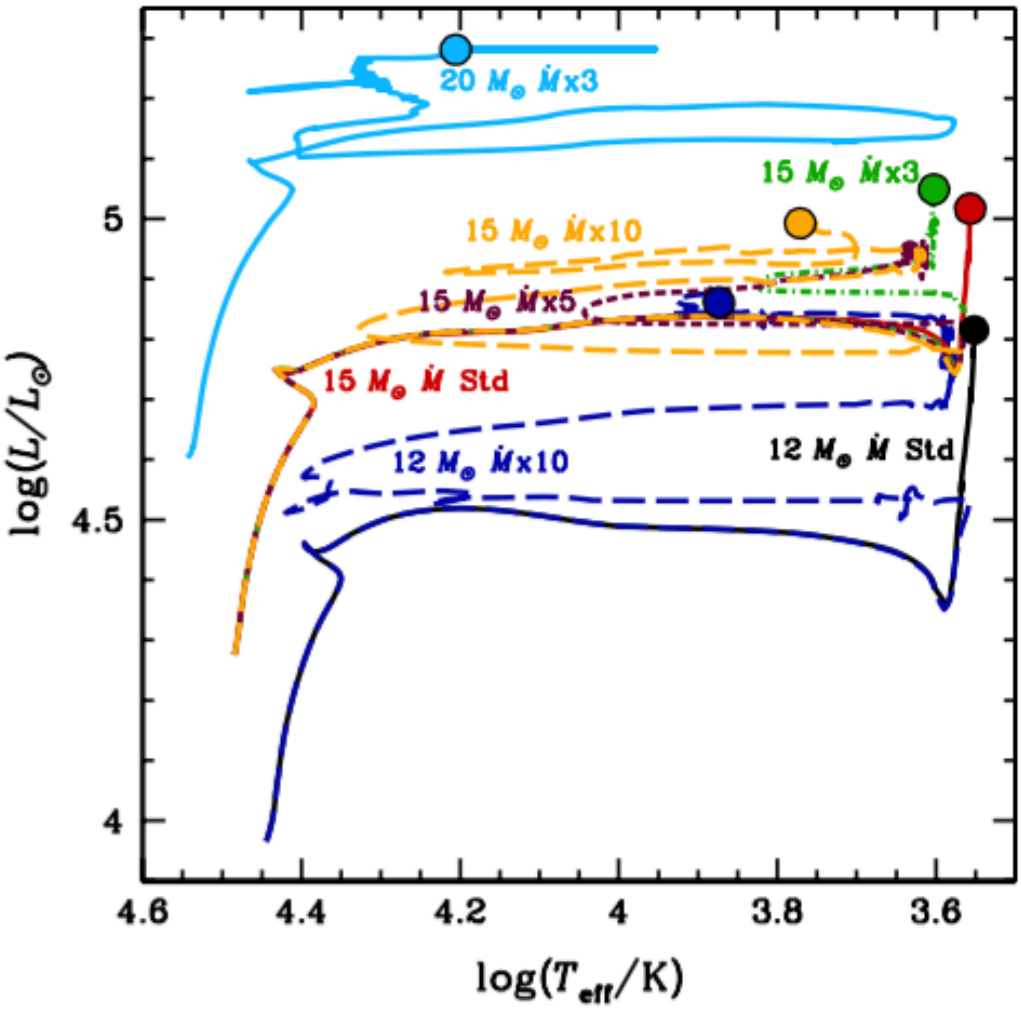

Figure 1.7: HRD for 12, 15 and 20$M_{\odot}$ stars with different levels of mass-loss applied. Taken from Georgy (2012).

which are potentially subject to systematic uncertainties (discussed at length in Davies & Beasor, 2018).

Davies & Beasor (2018) used RSGs in clusters to determine how the bolometric correction changes as the stars evolve towards SN. The authors found that the stars closest to death are later spectral types (i.e. they appear redder than early stage RSGs) and hence require a different bolometric correction to derive $L_{\rm bol}$. When re-appraising the progenitor masses, Davies & Beasor (2018) assumed that the RSGs were of later spectral types and used the new empirically motivated bolometric corrections and extinction estimates from Maund (2017). In all, when taking systematic effects into consideration the likely upper mass limit for RSG progenitors was found to be $\sim 19 M_{\odot}{}^{+2.5}_{-1.3}$ with a 95% confidence limit at $<27 M_{\odot}$. Further to this, when taking into account finite sample effects, the upper mass limit is $25 M_{\odot}$ ($<33 M_{\odot}$) thus eliminating the tension between observations and stellar evolutionary theory. Increasing $\dot{M}$ to solve the red supergiant problem is therefore not necessary.

1.4 Observations III: The blue-to-red supergiant ratio

The ratio of blue to red supergiants (B/R) may also shed light on the evolutionary path followed by massive stars. From B/R we can determine the ratio of time spent in the blue and red regions of the HR diagram after a star has left the main sequence. Strong mass-loss during the RSG phase has the potential to shorten the amount of time a star spends in the red region of the HR diagram, see further discussion below.

Variations in the B/R ratio have long been observed (e.g. Walker, 1964; Hartwick, 1970; Humphreys & Davidson, 1979; Cowley et al., 1979), specifically observations in the Galaxy show that there are a larger proportion of RSGs at lower metallicities (Humphreys & McElroy, 1984), and indeed there are more RSGs found in Galactic clusters than in SMC clusters (Meylan & Maeder, 1982). Many subsequent studies have also shown the trend of decreasing B/R with metallicity (e.g. Humphreys & McElroy, 1984; Carney et al., 1985; van den Bergh & Hagen, 1968), but evolutionary models

have struggled to reproduce this result theoretically (see Langer & Maeder, 1995, for a review).

The consensus seems to be that the difficulty in reproducing the B/R is due to the sensitivity of internal physics implemented in the models, e.g. convection and levels of core overshooting. Models with a given set of parameters can either reproduce B/R at low metallicity, or at high metallicity, but there is no single set of models that can reproduce B/R across all metallicities (Langer & Maeder, 1995; Maeder & Meynet, 2003). Mass-loss also has the potential to play a role. For a star in the He-burning phase of evolution, if the He core contains a large enough fraction of the total mass of the star it will return to the blue of the HR diagram (Chiosi et al., 1978; Maeder, 1981). Therefore, if strong mass-loss occurs during the RSG phase it will become a BSG or WR star, thus changing the amount of time spent in the RSG phase and the B/R ratio. This implies that once a star has reached the RSG phase, it would require *lower* levels of mass-loss in order to maintain its H envelope, and remain on the cool side of the HR diagram.

1.5 Red Supergiant Mass-Loss

Having mentioned already how $\dot{M}$ during the RSG phase may affect various observed phenomenon on the HR diagram, I now discuss the nature of this mass-loss. The first discovery of the winds of RSGs came from Deutsch (1956), where the massive M-type supergiant α Herculis was found to share a common circumstellar envelope with its visual companion. Deutsch (1956) also states that absorption lines had also been observed for several other M-supergiants, indicative of a circumstellar envelope. Following this work, Deutsch (1960) surveyed other red supergiants, finding circumstellar lines were common in M0 (and later) type stars (see also Wilson, 1960). Thus Deutsch concluded that α Her is not alone, and mass-loss may be an important process in the evolution of all other late-type supergiants. In the later work of Gehrz & Woolf (1971) the mid-IR excess was first observed, implying RSGs have warm dust in their CSM.

1.5.1 The winds of RSGs

At present, the wind driving mechanism in RSGs remains uncertain, and so the mass-loss rate of an RSG cannot be determined from first principles. Initially it was thought that the winds were driven by radiation on dust grains (e.g. Deutsch, 1956; Stothers, 1969; Gehrz & Woolf, 1971), however some studies suggest this cannot explain how the wind is driven in the dust free cavity nearest to the star, which can extend to 20 stellar radii (e.g. Ohnaka et al., 2008).

More recently it has been suggested that large scale photospheric convection could trigger mass-loss, by lowering the effective surface gravity. In conjunction with radiative pressure on molecular lines, convection could contribute to initiating mass-loss (Josselin & Plez, 2007). Indeed, large scale convective cells have since been observed for RSG Betelgeuse (e.g. López Ariste et al., 2018; Kervella et al., 2018).

Stellar pulsations have also been suggested as an important factor for RSG winds (e.g. Van Loon et al., 2008; Yoon & Cantiello, 2010) but the detailed mechanisms are still poorly understood.

1.5.2 Mass-loss rate measurements

Dust shell modelling

One commonly used method to estimate mass-loss is to model the mid-IR dust emission by solving the radiative transfer equation through the dusty wind.

Many early studies of RSG winds use this technique, Gehrz & Woolf (1971) used broad band mid-IR photometry to estimate $\dot{M}$, fitting these data points to dust shell models. In these models, the authors fixed the inner dust temperature to $T_{\rm in}$=900K (see discussion in Section 2.2.1), and assume the wind is driven by radiation pressure to estimate an outflow velocity (the driving mechanism for RSG winds is unknown, see Bennett, 2010).

Today, there are a number of codes available for dust shell modelling, such as MOCASSIN (Ercolano et al., 2003), 2-DUST (Ueta & Meixner, 2003) and DUSTY (Ivezic et al., 1999). Throughout this study, I will be using DUSTY. While MOCASSIN and 2-DUST both have the capacity to model asymmetrical dust shells, taking into account effects such as clumping, this is not necessary for this study (see Section 2.2.1 for further discussion).

DUSTY is an open source dust shell modelling code that solves the radiative transfer equation for a star obscured by a 1-D spherical dust shell of a certain optical depth ($\tau_{\rm V}$, optical depth at 0.55μm), inner dust temperature ($T_{\rm in}$) at the innermost radius ($R_{\rm in}$), density profile $\rho(r)$ and temperature structure T(r), for a given dust chemical composition and grain size (a).

As photons travel through the circumstellar medium (CSM) surrounding a star, there are a number of factors that will affect how the star appears to us. If the dust shell is optically thin, photons are able to pass through the atmosphere easily with little interaction. If the dust shell is optically thick, photons will interact more and become scattered (or absorbed and re-emitted) before they escape. For dust enshrouded stars, the emerging radiation can be significantly altered when compared to the source radiation from the star. The radiative transfer equation describes how a star will appear to us after the emitted photons have passed through the CSM. The equation in simplified form is

$$I_0, \lambda(0) = I_1 e^{-\tau_\lambda} + S_\lambda(1 - e^{-\tau_\lambda}) \tag{1.1}$$

where $I_\lambda(0)$ is the observed radiation, I_1 is the emitted radiation from the star, τ_λ is the optical depth of the dust shell at wavelength λ and S_λ is the source function (the ratio of emission to absorption processes). For a purely absorbing medium at local thermodynamic equilibrium (i.e. the length-scale for temperature changes is much longer than the mean-free-path for particle collisions) the source function is simply the Planck function, which itself is dependent on the local temperature. If the scattering is high, then the source function simply equates to the intensity of the star as all radiation

scattered within the dust shell is re-emitted at the same wavelength (e.g. Kochanek et al., 2014).

The DUSTY code assumes the source object is in radiative equilibrium, meaning that the luminosity of the (in this case) star is the same at all radii. As a result, the temperature of the star scales as T $\sim$ 1/r$^{1/2}$, where r is the radial coordinate from the centre of the star. The optical depth of an atmosphere depends on the opacity κ and density ρ as a function of distance s from the star ($\tau = \int \kappa\rho$ ds). Opacity is determined from the chemical composition of the dust, and is contained within look-up tables provided in DUSTY for six common grain types (the dust surrounding RSGs has been confirmed by observations to be oxygen rich, e.g. Sargent et al., 2011). Specifically, the ratio of light that is scattered or absorbed is calculated using Mie thoery, which states that the scattering efficiency of the dust is dependent on the grain size.

This work assumes a steady state wind with a constant velocity, or a density profile of $\rho \sim$r^{-2}. At a certain distance D, the circumstellar dust has no impact on the observable SED as it is too cool and too low density, and therefore equilibrium is reached on a timescale $t_{eq} = D/v_\infty$, where v_∞ is the outflow velocity of the wind. For an RSG, the inner dust radius is approximately 20 stellar radii (Ohnaka et al., 2008). If we assume the stellar radii, $R_\star$, is 10^8km, the outer boundary of the dust layer, R_{out}, lies at approximately 10^{11}km. For a wind where v_∞ is 25km/s, the equilibrium timescale is approximately 10,000 years. Fluctuations in mass-loss, such as episodic mass-loss events, that occur on timescales far smaller than t_{eq} would be undetectable. Any fluctuations larger than this would result in a density profile either steeper or shallower than $\rho \sim$r^{-2}, an effect which can be mimicked by altering the position of the inner dust radius (see in depth discussion in 2.4.2).

DUSTY also has the option of a radiatively driven wind with an acceleration zone, however as radiatively driven winds have been shown to be inadequate for explaining the mass-loss from RSG (see 1.5) we have chosen to model the wind as steady state (i.e. a constant outflow velocity). Indeed, Groenewegen (2012) showed that computing winds in the radiatively driven wind mode can result in $\dot{M}$values that are up to 60 times higher than those calculated when using the former DUSTY mode. This is due to the

acceleration zone within radiatively driven wind models. In such a model, the outflow velocity is small at low radii, and so for a fixed mass-loss rate the density required in the radiatively driven wind paradigm is higher than that for a steady state wind. This in turn results in more emission from the dust per unit mass-loss rate, and for a given mid-IR excess the mass-loss rate will be higher.

Ultimately, to determine a value for $\dot{M}$, we need to determine a dust shell mass. For this, we need to know the gas-to-dust ratio ($r_{\rm gd}$), optical depth (τ) and the inner dust temperature, $T_{\rm in}$, i.e. the temperature at the innermost dust boundary, $R_{\rm in}$, of the dust shell. Many studies fix the value of the inner dust temperature to the literature value of 1200K, however in this work we will leave $T_{\rm in}$ and τ as free parameters, finding the best fit solution and determining the dust shell density ρ_r. To convert dust shell mass into a value for $\dot{M}$ an outflow velocity must be assumed. In Chapter 2 I will discuss this in detail.

Other methods

Another method to derive mass-loss rates for cool supergiants is by modelling the wind's molecular emission lines in the mid-IR. CO rotational lines have long been used to probe the circumstellar environment (CSE) of AGB stars (e.g. Knapp et al., 1982; Knapp & Chang, 1985; Olofsson, 1993), and is useful as almost all of the elemental carbon is found within CO molecules throughout the envelope Decin et al. (2006). Specifically, the low excitational transition J to $J-1$ can be used to derive density, velocity and temperature in the envelope of the star. More recent studies have combined observations of low and high excitational lines (De Beck et al., 2010) to better probe mass-loss of AGBs and RSGs.

There are many reasons CO is a useful probe of CSM. CO is the most abundant molecule in the envelope, and the lines are weak enough that they do not saturate (except in the case of extreme mass-loss rates). However, this method requires a large correction factor to derive a value for $\dot{M}$ from the CO line strength alone, as the overall quantity of CO in the winds is relatively low (De Beck et al., 2010). The fractional

CO abundance ($f_{\rm CO}$) depends on to what degree C and O are fully associated in the envelope. Solar abundances assuming full association suggest $f_{\rm CO}$ between 5×10^{-4} and 10^{-3}, but this is likely to be larger for more massive M-type stars (see Höfner & Olofsson, 2018).

To derive $\dot{M}$ from CO lines radiative transfer codes are used (e.g. Groenewegen, 1994; Schöier & Olofsson, 2001; Decin et al., 2006). De Beck et al. (2010) provide $\dot{M}$ estimates based on many CO lines for 47 sample stars. By accounting for line saturation the authors are able to probe at much higher $\dot{M}$s than previous works, finding RSGs reach mass-loss rates between $2\times10^{-7}M_{\odot}$ yr^{-1} and $3\times10^{-4}M_{\odot}$ yr^{-1}. While this method is a useful tool for deriving $\dot{M}$, large exposure times are required to have a high enough signal-to-noise to fully resolve the CO lines. As a result of this, it would not be possible to use this method for stars in the LMC or SMC.

It is also possible to use atomic lines to study mass-loss. For example, Sanner (1976) determined $\dot{M}$ for red giants and RSGs using photoelectric scans of optical resonance lines. By making assumptions about the physical properties of the CSM (e.g. physical detachment from the photosphere) and using the metal lines to determine the density and wind velocity, a value for $\dot{M}$ can be estimated. The authors speculate that the value of $\dot{M}$ found is likely within a factor of 6 of the true value, but may in fact have larger errors depending on the abundance of the metals relative to hydrogen as they assume cosmic abundances of the elements.

RSGs in binary systems with B stars are another useful method for determining mass-loss. In such a system, the B star contributes to almost all of the flux in the ultraviolet (UV). When the B star passes behind its companion, the absorption spectrum of the RSG wind is visible in the B star continuum. For example, the mass-loss of M supergiant α Sco A was determined by using high dispersion spectra of both α Sco A and its MS companion α Sco B (Kudritzki & Reimers, 1978). Visual binaries allow for sharp circumstellar lines to be separated from the photospheric spectra and can be treated as pure absorption lines, unlike for single stars where circumstellar lines can be difficult to separate from the strong photospheric lines (Reimers, 1977). While these studies provide a reliable measure of mass-loss there are not many visual binary sys-

tems for which this exercise can be repeated, and hence the prescription is based only on a handful of objects.

1.5.3 Implementation of mass-loss in evolution models

As the mass-loss mechanism remains elusive, stellar evolution models rely solely on mass-loss rate prescriptions which have been derived empirically.

An early parameterisation of $\dot{M}$ came from Reimers (1975), updated in Kudritzki & Reimers (1978). Using mass-loss rates from circumstellar absoprtion features, chromospheric emission lines and data from Gehrz & Woolf (1971), Reimers (1975) suggested mass-loss could be characterised as $\dot{M} = \eta LR/g$ (in Solar units, with η being a free parameter). This relation was updated using constraints from Kudritzki & Reimers (1978), where visual binary systems were used to derived absolute mass-loss rates. From this, the Reimers relation could be calibrated to $\dot{M} = 5.5 \times 10^{-13} LR/g$.

Currently the most widely used $\dot{M}$-prescription is that of (De Jager et al., 1988, , hereafter dJ88), in which the authors undertook a literature study and compiled mass-loss rate measurements for 271 field stars across spectral types O through M, of which 15 are RSGs. The RSG sample itself is highly heterogeneous in terms of initial mass and metallicity of the star, and the methodology used to determine $\dot{M}$ is similarly heterogeneous (see the previous section for discussion on the methods included). Many of the methods used to calculate $\dot{M}$ result in large errors, as such the scatter on the $\dot{M}$-$L_{\rm bol}$ relation is large, approximately a factor of 10 (Mauron & Josselin, 2011). In terms of evolution, a factor of 10 error on $\dot{M}$ could be the difference between a star losing none or losing the entirety of the envelope.

More recent $\dot{M}$-prescriptions have been derived, such as Van Loon et al. (2005) and Goldman et al. (2017). These studies modelled the dust shell of AGBs and RSGs using radiative transfer codes (e.g. DUSTY). However in both of these studied the sample is skewed towards the highest $\dot{M}$ RSGs, by choosing dust enshrouded objects (Van Loon et al., 2005) or objects that emit masers, a well known tracer of strong mass-

loss (Goldman et al., 2017). For this reason, while these prescriptions are based on larger data sets with a more homogeneous method, they are only applicable to objects at the later phases of evolution when $\dot{M}$ is at its peak.

1.6 This thesis

The evolution of massive stars to supernovae is strongly influenced by mass-loss during the RSG phase. Strong $\dot{M}$ has the potential to divert a star's evolutionary path and send the star back to the blue of the HR diagram. Observations of massive stars therefore provide vital tests of stellar evolutionary theory.

There have been many observations found to be at conflict with theory, for example the apparent lack of high mass RSG progenitors to CCSN, and many studies have used varying mass-loss by large factors as a potential way to resolve any tensions. In this study, I aim to constrain mass-loss during the RSG phase of evolution, ultimately providing a new $\dot{M}$-prescription to better inform stellar evolutionary theory.

At present, the most widely used $\dot{M}$-prescription in stellar models contains large internal dispersion. This could be due to the fact that the samples used have relied on an inhomogeneous set of RSGs (field stars) where $\dot{M}$s and luminosities have been derived by a variety of different methods. The work I will present here will differ as I will be focusing on RSGs in clusters. Stellar clusters provide a unique opportunity to know the age, and hence initial masses, of the RSGs we are studying. This will allow me to see how mass-loss varies not only with luminosity, but with the initial mass of the star (discussed in great depth in Chapters 2,3 and 5.

This thesis will be structured as follows; in Chapter 2 I will first use an LMC cluster, NGC 2100, as a pilot study, deriving $\dot{M}$ and luminosities for each of the 19 RSGs in the cluster. In Chapter 3 I will expand this study to include two Galactic clusters, NGC 7419 and χ Per, comparing results to evolutionary models. Chapter 4 will describe efforts to accurately measure the ages of the clusters in question, and derive initial masses for the RSGs in each cluster. Finally, Chapter 5 will combine all of the work

presented in the previous chapters, as well as including $\dot{M}$ and L measurements for two more clusters, NGC 2004 and RSGC1, probing the high and low end of the RSG initial mass range. This chapter includes new data from SOFIA as well as archival data. Ultimately in Chapter 5 I will present a new initial mass dependent mass-loss rate prescription for RSGs, which can be implemented in stellar evolutionary models. In my final chapter I will discuss the conclusions of my work, as well as set out a plan for future work.

Chapter 2

The Evolution of Red Supergiants to Supernova I: NGC 2100

2.1 Introduction

This chapter presents work which has been published by Beasor & Davies (2016). The data analysis and interpretation were conducted by E. R. Beasor. The initial draft of the publication was written by E. R. Beasor, who then incorporated comments from co-authors and from an anonymous referee in the final draft.

As already discussed in Chapter 1, knowledge of the mass-loss rates ($\dot{M}$) of red supergiants (RSGs) is fundamentally important for understanding stellar evolution. Changing $\dot{M}$ has effects on the subsequent evolution of the star, as well as the supernova (SN) type and eventual remnant (e.g. Maeder, 1981; Chiosi & Maeder, 1986).

This is particularly pertinent for issues such as the Red Supergiant Problem, where an observed lack of progenitors at the upper end of the predicted RSG mass range is at odds with stellar evolutionary theory (see Section 1.3.1 for an in-depth discussion).

Are all RSGs exploding as Type IIP SNe? Or does the extreme mass-loss affect the final evolution of these massive stars? Stellar evolution models currently rely on observational or theoretical mass-loss rate prescriptions (e.g. De Jager et al., 1988; Reimers,

1975; Van Loon et al., 2005; Nieuwenhuijzen & De Jager, 1990; Feast & Whitelock, 1992). A potential weakness of these prescriptions is that they have relied on observations of field stars, not coeval stars, leaving parameters of initial mass ($M_{\rm initial}$) and metallicity (Z) unconstrained which could potentially explain the large dispersions in the observed trends. The implications of varying mass-loss during the RSG phase are discussed at length in 1.1.2.

In this chapter I measure the amount of circumstellar material and estimate mass-loss rates, to investigate whether this is correlated with how close the star is to supernova. I model the mid-IR excess of 19 RSGs in stellar cluster NGC2100, each of which I assume had the same initial mass and composition, but where the stars are all at slightly different stages of evolution. This allows us to investigate the $\dot{M}$ behaviour with evolution of the RSG.

I begin in Section 2.2 by describing the dust shell models and choice of input parameters. In Section 2.2.2 I discuss applying this to the stars in cluster NGC 2100 and the results I derive from the models. Finally, in Section 2.3.1 I discuss the results in terms of RSG evolution and progenitors.

2.2 Dust shell models

The models used in this project were created using DUSTY (Ivezic et al., 1999). Stars surrounded by circumstellar dust have their radiation absorbed/re-emitted by the dust particles, changing the output spectrum of the star. DUSTY solves the radiative transfer equation for a star obscured by a spherical dust shell of a certain optical depth (τ_V, optical depth at 0.55 μm), inner dust temperature ($T_{\rm in}$) at the innermost radius ($R_{\rm in}$). Below I describe my choices for the model input parameters and the fitting methodology.

2.2.1 Model parameters

Dust composition

It is necessary to define a dust grain composition when creating models with DUSTY as this determines the extinction efficiency Q_λ, and hence how the dust shell will re-process the input spectral energy distribution (SED). Observations of RSGs confirm the dust shells are O-rich, indicated by the presence of mid-IR spectral features at 12 and 18 μm known to be caused by the presence of silicates. I opted for O-rich silicate dust as described by Draine & Lee (1984). Ossenkopff 'warm' and 'cold' silicates (Ossenkopf et al., 1992) were also considered resulting in only small changes to the output flux. The differences in flux from each O-rich dust type were found to be smaller than the errors on the photometry. I therefore concluded that the final results were insensitive to which O-rich dust type was chosen.

Grain size, a

DUSTY requires a grain size distribution to be specified. Kochanek et al. (2012) used DUSTY to model the spectrum for the RSG progenitor of SN 2012aw, opting for the MRN power law with sharp boundaries, ($dn/da \propto a^{-3.5}$ for 0.005 μm $<$ a $<$ 0.25 μm; Mathis et al., 1977). This power law is more commonly associated with dust grains in the interstellar medium. Van Loon et al. (2005) also used DUSTY to model dust enshrouded RSGs, choosing a constant grain size of 0.1μm. However, it is also stated in this paper that the extinction of some of the most dust enshrouded M-type stars was better modelled when a smaller grain size, 0.06μm or a modified MRN distribution, between 0.01 and 0.1μm, was used. Groenewegen et al. (2009) also investigated the effect of grain size on the output spectrum, finding a grain size of 1μm fit reasonably well to the observations of O-rich RSG stars in the SMC and LMC. Using recent observations of VY Canis Majoris, a nearby dust-enshrouded RSG, Scicluna et al. (2015) suggested the dust surrounding the star has a constant grain size of 0.5μm. This is in line with previous observations such as those by Smith et al. (2001), who found

the grain size to be between 0.3 and 1μm. Taking all this into account I created models for the MRN power law as well as constant grain sizes of 0.1, 0.2, 0.3, 0.4 and 0.5μm, choosing 0.3μm as the fiducial grain size. However, as I am studying stars' emission at wavelengths much greater than grain size ($\lambda > 3\mu$m) the scattering and absorption efficiencies of the dust are largely independent of the grain size. This is discussed further in Section 2.3.3.

Density distribution

Here, I assumed a steady state density distribution falling off as r^{-2} in the entire shell with a constant terminal velocity. The outflow velocities for RSGs in this sample are not known, so I rely on previous measurements to estimate this value. Van Loon et al. (2001) and Richards & Yates (1998) both used maser emission to map the dust shells of other RSGs, finding v_∞ values consistent with ∼20-30 km/s for the stars in their samples. I opted for a uniform rate of 25 ± 5 km/s for the outflow wind. Radiatively driven wind theory suggests that v_∞ scales with luminosity, $v_\infty \propto L^{1/4}$, though this is negligible for the luminosity range I measure compared to the errors on luminosity. It is specified that the shell extends to 10000 times its inner radius, such that the dust density is low enough at the outer limit that it has no effect on the spectrum. A gas to dust ratio is also required to be input, r_{gd}. It has been shown that this quantity scales with metallicity (Marshall et al., 2004), so while the gas to dust ratio for RSGs in the Milky Way is around 200:1, for RSGs in the more metal poor LMC the value is higher, around 500:1. I also assumed a grain bulk density, ρ_d of 3g cm^{-3}. The values adopted for r_{gd} and r_s will have an effect on the absolute values of $\dot{M}$. It is likely that changes in these properties would have little to no effect on the relative $\dot{M}$ values and the correlation with luminosity, but the absolute value of the relation may change.

The calculation of $\dot{M}$ requires the calculation of τ_λ between $R_{\rm in}$ and $R_{\rm out}$

$$\tau_\lambda = \int_{R_{\rm in}}^{R_{\rm out}} \pi a^2 Q_\lambda n(r) dr \tag{2.1}$$

for a certain number density profile, $n(r) = n_0(R_{\rm in}/r)^2$, where n_0 is the number density at the inner radius, $R_{\rm in}$, and Q_λ is the extinction efficiency. I can rearrange to find the mass-density ρ_0 at $R_{\rm in}$,

$$\rho_0 = \frac{4}{3}\frac{\tau_\lambda \rho_d a}{Q_\lambda R_{in}}. \tag{2.2}$$

By substituting this into the mass continuity equation ($\dot{M} = 4\pi r^2 \rho(r) v_\infty$) a mass-loss rate can be calculated,

$$\dot{M} = \frac{16\pi}{3}\frac{R_{in}\tau_\lambda \rho_d a v_\infty}{Q_\lambda} r_{gd}. \tag{2.3}$$

My choice of density distribution differs from that used in other similar work, for example Shenoy et al. (2016), who performed a similar study on the red supergiants μCep and VY CMa. By adopting a constant $T_{\rm in}$ value of 1000K and allowing the density exponent to vary, Shenoy et al. (2016) found that the best fits were obtained by adopting exponents < 2, and hence concluded that $\dot{M}$ decreases over the lifetime of the stars. In Section 2.4.2 I show that this can be reconciled by fixing the density exponent to be 2, and allowing $T_{\rm in}$ to vary. While 1200K is the commonly adopted temperature for silicate dust sublimation, there are many observations in the literature that suggest dust may begin to form at lower $T_{\rm in}$, and hence larger radii. There is interferometric data supporting the case for RSGs having large dust free cavities, for example Ohnaka et al. (2008), who used N-band spectro-interferometric observations to spatially resolve the dust envelope around LMC RSG WOH G64. Sargent et al. (2010) used radiative transfer models of dust shells around two LMC AGB stars, finding best fit models with lower $T_{\rm in}$ values of 430K and 900K. These values are comparable to previous determinations of $T_{\rm in}$ for O-rich stars from mid-IR infrared fitting similar to the work presented here (e.g. Bedijn, 1987; Schutte & Tielens, 1989; Van Loon et al., 2005) suggesting $T_{\rm in}$ often differs from the hot dust sublimation temperature of 1000-1200K.

Sensitivity to T_{eff}

DUSTY requires an input SED to illuminate the dust shell, so that the light can be reprocessed and re-emitted. The SEDs I use are synthesised from MARCS model atmospheres (Gustafsson et al., 2008) using TURBOSPECTRUM (Plez, 2012). I opted for typical RSG parameters (log(g)=0.0, microturbulent velocity 4km/s) and an LMC-like metallicity of [Z]=–0.3, though the precise value of these parameters are relatively inconsequential to the morphology of the SED. The most important parameter is the stellar effective temperature, $T_{\rm eff}$. Patrick et al. (2016) used KMOS spectra of 14 RSGs in NGC2100 (of which 13 are analysed in this thesis), finding the average $T_{\rm eff}$ to be 3890 $\pm$ 85 K. This is consistent with the temperature range observed by Davies et al. (2013), who found the average $T_{\rm eff}$ of a sample of RSGs in the LMC to be 4170 $\pm$ 170K, by using VLT+XSHOOTER data and fitting this to line-free continuum regions of SEDs. In this study I have opted for a fiducial SED of $T_{\rm eff}$= 3900K in line with these findings. I also checked how sensitive the results were to this choice of SED temperature by re-running the analysis with stellar SEDs 300K above or below the fiducial SED, fully encompassing the range observed by Patrick et al. (2016). I found that the different SEDs reproduced the mid-IR excess, and therefore the inferred $\dot{M}$, almost identically with very small errors ($< 10\%$). Different $T_{\rm eff}$ values do however affect the bolometric correction and therefore $L_{\rm bol}$, leading to errors of $\sim$0.14dex on the luminosity measurements.

Departure from spherical symmetry

Observations show that RSG nebulae are often clumpy, rather than spherically symmetric (e.g. Scicluna et al., 2015; O'Gorman et al., 2015; Humphreys et al., 2007). I investigated the effect of clumped winds by comparing the 1D models with those from MOCASSIN (Ercolano et al., 2003, 2005, 2008), a code which solves the radiative transfer equation in 3D. I found that clumping has no effect up to a filling factor of 50. As long as the dust is optically thin there is no change in the output spectrum.

$T_{\rm in}$ and τ_V

Finally, DUSTY also allows inner temperature, $T_{\rm in}$, and the optical depth τ_V to be chosen. $T_{\rm in}$ defines the temperature of the inner dust shell (and hence its position). The optical depth determines the dust shell mass. As these parameters are unconstrained, in this study I have allowed them to vary until the fit to the data is optimised. This fitting methodology is described in the next subsection.

2.2.2 Fitting methodology

I first computed a grid of dust shell models spanning a range of inner temperatures and optical depths. For each model I then computed synthetic WISE and Spitzer photometry by convolving the model spectrum with their relevant filter profiles. This synthetic model photometry was compared to each stars' mid-IR photometry from WISE, IRAC and MIPS. The grid spanned τ_v values of 0 - 1.3 with 50 grid points, and inner temperature values from 100K to 1200K in steps of 100K. By using χ^2 minimisation I determined the best fitting model to the sample SED.

$$\chi^2 = \sum \frac{(O_i - E_i)^2}{\sigma_i^2} \tag{2.4}$$

where O is the observed photometry, E is the model photometry, σ^2 is the error and i denotes the filter. In this case, the model photometry provides the "expected" data points. The best fitting model is that which produced the lowest χ^2.

To account for systematic errors I applied a blanket error of 10% to the observations. The errors on the best fitting model parameters were determined by models within the lowest χ^2+10. While this is not the formal error for a 2-parameter fit (χ^2+2.3), as we are dominated by systematic rather than random errors, the formal errors were unrealistically small. The χ^2+10 limit was chosen so that the stars with the lowest measured $\dot{M}$, which were clearly consistent with non-detections, would have $\dot{M}$ values consistent with 0 (or upper limits only).

2.3 Application to NGC2100

In this study I apply this dust modeling to a sample of RSGs in a young star cluster. Such clusters can be assumed to be coeval, since any spread in the age of the stars will be small compared to the age of the cluster. Hence, I can assume that all stars currently in the RSG phase had the same initial mass to within a few tenths of a solar mass. Since the stars' masses are so similar, they will all follow almost the same path across the H-R diagram. Differences in luminosity are caused by those stars with slightly higher masses evolving along the mass-track at a slightly faster rate. It is for this reason that luminosity can be taken as a proxy for evolution.

The photometry used in this thesis is taken from 2MASS, Spitzer and WISE (Skrutskie et al., 2006; Werner et al., 2004; Wright et al., 2010) and is listed in Table 2.2. A finding chart for NGC2100 is shown in Fig. 2.1 in which the RSGs are numbered based on [5.6]-band magnitude. Star #13 has been omitted from my analysis due to large disagreements between the MIPS and WISE photometry, as well as WISE and IRAC.

Table 2.1: Star designations and positions. Stars are numbered based on their [5.6]-band magnitude.

Name	ID	RA (degrees) J2000	DEC (degrees) J2000	W61[a]	R74[b]
1	J054147.86-691205.9	85.44944763	-69.20166779	6-5	D15
2	J054211.56-691248.7	85.54819489	-69.21353149	6-65	B40
3	J054144.00-691202.7	85.43335724	-69.20075989	8-67	...
4	J054206.77-691231.1	85.52821350	-69.20866394	...	A127
5	J054209.98-691328.8	85.54161072	-69.22468567	6-51	C32
6	J054144.47-691117.1	85.43533325	-69.18808746	8-70	...
7	J054200.74-691137.0	85.50312042	-69.19362640	6-30	C8
8	J054203.90-691307.4	85.51628113	-69.21873474	6-34	B4
9	J054157.44-691218.1	85.48937225	-69.20503235	6-24	C2
10	J054209.66-691311.2	85.54025269	-69.21979523	6-54	B47
11	J054152.51-691230.8	85.46879578	-69.20856476	6-12	D16
12	J054141.50-691151.7	85.42295837	-69.19770813	8-63	...
13	J054207.48-691250.3	85.53116608	-69.21398163	6-48	...
14	J054204.78-691058.8	85.51993561	-69.18302917	6-44	...
15	J054206.13-691246.8	85.52555847	-69.21302032	6-46	...
16	J054206.36-691220.2	85.52650452	-69.20561218	6-45	B17
17	J054138.59-691409.5	85.41079712	-69.23599243	8-58	...
18	J054212.20-691213.3	85.55084229	-69.20370483	6-69	B22
19	J054207.45-691143.8	85.53106689	-69.19552612	6-51	C12

[a] star designation from Westerlund (1961)

[b] star designation from Robertson (1974)

Table 2.2: Observational data. All fluxes are in units of mJy.

Name	IRAC1 (3.4 μm)	IRAC2 (4.4 μm)	IRAC3 (5.6 μm)	IRAC4 (7.6μm)	MIPS1 (23.2 μm)	2MASS-J	2MASS-H	2MASS-Ks	WISE1 (3.4 μm)	WISE2 (4.6 μm)	WISE3 (11.6 μm)	WISE4 (22 μm)
1	176.0±0.2	163.00± 0.03	150.0±0.05	141.00±0.04	140.00±0.063	244± 4	364±12	344± 9	240±6	153±2.8	166± 2.6	149± 3.97
2	-	95.10± 0.02	115.0±0.05	120.00±0.03	113.00±0.063	237± 5	359±13	324± 5	173± 3	116± 2.0	146± 2.0	132± 3.04
3	131.0±0.1	72.70± 0.02	64.7±0.04	43.80±0.02	-	232 ± 4	332±10	286± 6	171 ± 3	82± 1.5	33± 0.7	25± 1.63
4	86.6±0.1	65.20± 0.02	60.7±0.04	56.50±0.02	33.20± 0.063	161± 3	220± 4	196± 4	120± 3	65± 1.5	51± 0.8	36± 1.59
5	101.0±0.1	64.10± 0.02	56.9±0.03	49.00±0.02	26.10±0.064	154± 3	220± 4	194± 4	145± 2	66± 1.2	39± 0.7	30± 1.30
6	110.0±0.1	65.10± 0.02	56.6±0.03	46.00±0.02	27.50±0.065	186± 3	270± 6	240± 4	137± 2	70± 1.3	37± 1.0	35± 3.08
7	92.6±0.1	62.30± 0.02	53.7±0.03	38.10±0.02	-	173± 3	249± 5	220± 4	125± 2	60± 1.1	27± 0.6	12± 1.23
8	93.5±0.1	58.10± 0.02	50.9±0.03	42.00±0.02	19.20±0.063	183± 3	254± 5	209± 4	113± 2	56± 0.9	30± 0.5	14± 1.63
9	93.6±0.1	58.30± 0.02	48.4±0.03	36.30±0.02	-	187± 3	244± 5	209± 4	113± 2	56± 1.0	22± 0.6	2± 0.77
10	80.7±0.1	50.70± 0.02	41.3±0.03	26.00±0.02	-	161± 3	223± 4	190± 4	105± 2	51± 1.0	15± 0.3	11± 1.14
11	68.1±0.1	43.30± 0.01	34.7±0.03	23.70±0.02	-	108± 2	156± 3	143± 2	84± 1	41± 0.8	10± 0.5	4± 0.87
12	63.7±0.1	41.80± 0.01	32.8±0.03	23.00±0.02	-	125± 2	181± 3	156± 3	83± 1	39± 0.7	13± 0.5	3± 1.25
13	75.2±0.1	-	32.4±0.03	21.50±0.02	-	131± 3	178± 4	160±3	140± 2	73± 1.3	20± 0.4	21± 1.07
14	65.7±0.1	37.50± 0.01	29.2±0.03	16.60±0.02	-	117± 2	171± 3	142± 2	75± 1	35± 0.6	6± 0.4	-
15	62.9±0.1	36.30± 0.01	28.7±0.02	17.80±0.02	-	120± 3	166± 5	137± 3	106± 9	44± 3.7	4± 1.2	-
16	62.0±0.1	37.00± 0.01	28.4±0.02	17.80± 0.02	-	112± 2	162± 3	142± 2	94± 1	49± 0.9	19± 0.4	14± 1.03
17	59.7±0.1	35.70± 0.01	27.1±0.02	16.80±0.02	-	113± 2	155± 3	135± 2	73± 1	34± 0.6	9± 0.3	3± 1.08
18	51.4±0.1	31.50± 0.01	24.0±0.02	14.40±0.01	-	105± 2	142± 3	121± 2	64± 1	30± 0.6	5± 0.2	-
19	53.8±0.1	30.40± 0.01	22.6±0.02	-	-	101± 2	144± 2	119± 2	61± 1	28± 0.5	3± 0.2	-

The RSG in NGC2100 can be seen as a clump of stars in CMD space with a K_S-band magnitude less than 9.49 within a 2 arcminute radius of the cluster centre. This identified 19 candidate RSGs. By plotting J-K vs. K it was possible to locate RSGs in the data as a clump of stars clearly separated from the field stars. This is shown in Fig. 2.2. The red circles indicate RSGs.

From the photometry alone it was possible to see evidence of $\dot{M}$ evolving with evolution of the RSG. This qualitative evidence is shown in the [8-12] vs. [5.6] CMD, Fig. 2.3. The [5.6]-band magnitude can be used as a measure of luminosity as the bolometric correction at this wavelength is largely insensitive to the RSG's temperatures, whilst also being too short a wavelength to be significantly affected by emission from circumstellar dust. The [8-12] colour can be used as a measure of dust shell mass as it measures the excess caused by the broad silicate feature at 10μm. It can be seen from Fig. 2.3 that more luminous (and therefore, more evolved) RSGs have a larger amount of dust surrounding them (shown by the increasing colour, meaning they appear more reddened), suggesting dust mass increases with age.

Below I discuss the modeling results and compare them to mass-loss rate prescriptions frequently used by stellar evolution groups.

2.3.1 Modeling results

I ran the fitting procedure for the 19 RSGs located in NGC2100, and the results are shown in Table 2. Figures 2.4-2.6 shows example model fits with observed photometry for stars #1, #8 and #12. The plot shows the best fit model spectra (green line), the models within the error range (blue dotted lines) and the various contributions to the flux, including scattered flux, dust emission and attenuated flux. It also shows the photometric data (red crosses) and model photometry (green crosses). The 10μm silicate bump can be clearly seen; this is due to dust emission (pink dashed line). The plot also shows the significant effect scattering within the dust shell (grey dotted/dashed line), contributing a large proportion of the optical output spectrum.

Figure 2.1: Finding chart for RSGs in NGC2100. The stars are numbered based on [5.6]-band magnitude.

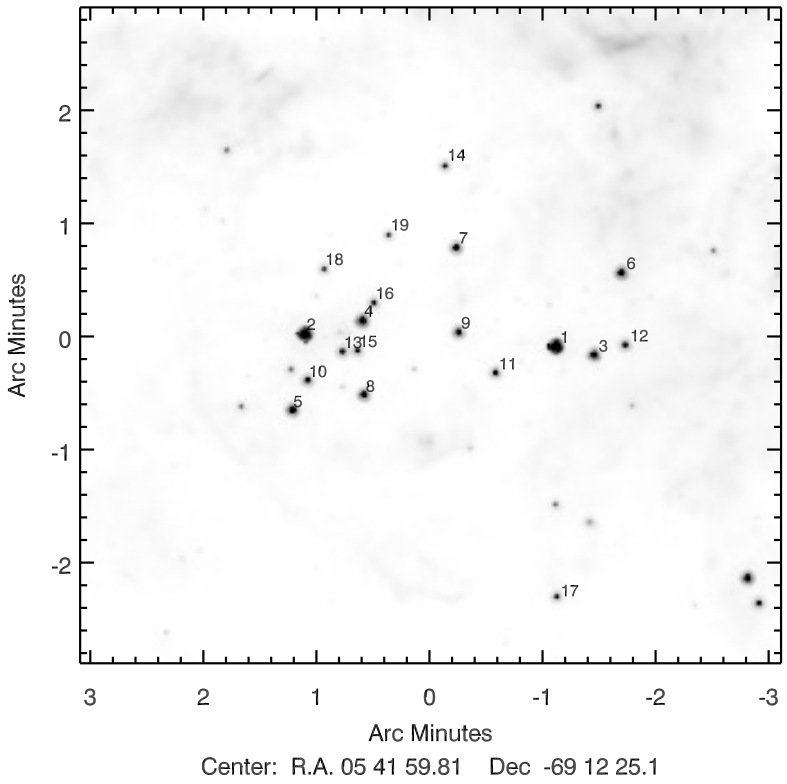

The fitting procedure did not include the JHK photometry bands as these bands are strongly affected by extinction, but when over-plotting this photometry (once de-reddened) it was found to be in good agreement with the model spectrum for all stars except #1 and #2, for which the model over-predicts the near-IR flux. Figures 2.5 and 2.6 show the model fits for stars #8 and #12 respectively, representative of medium and low $\dot{M}$ values.

I attempted to explain the missing near-IR (NIR) flux in stars #1 and #2 by adapting the fitting procedure to include JHK photometry and to include a lower $T_{\rm eff}$ SED. This gave a better fit to the near-IR photometry but at the expense of a poorer fit to the 3-8μm region, where the model now underpredicted the flux. I considered whether this fit could be improved by dust emission. To achieve this, it would require either unphysically high dust temperatures above the sublimation temperature for silicate dust, or it would require an increase in dust mass of a factor of 100. This would lead to significantly poorer fits to the mid-IR photometry and can therefore be ruled out. There

Figure 2.2: Colour-magnitude plot using J-K_s vs. K_s to locate RSGs in NGC 2100. This plot also shows a14Myr PARSEC isochrone (Tang et al., 2014; Chen et al., 2015) at LMC metallicity (non-rotating). Isochrones have been adjusted for the distance to the LMC and a foreground extinction of A_V=0.5. The extinction noted in the legend is *in addition* to the foreground extinction already known to be present in the LMC (Niederhofer et al., 2015).

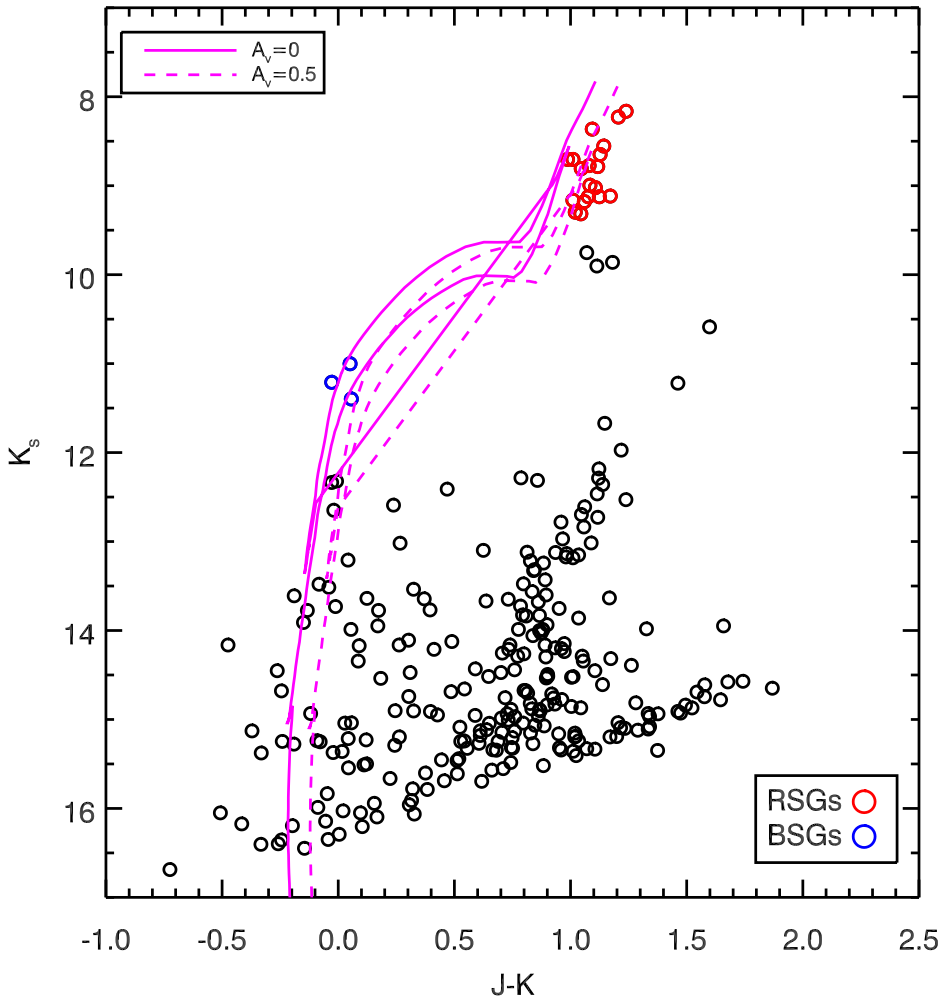

Figure 2.3: Colour magnitude plot of RSGs in the cluster to show increasing dust mass with age. [5.6]-band magnitude is used as an indicator of $L_{\rm bol}$ and the [8-12] colour is used as a measure of dust shell mass. The [8-12] colour is useful as it includes the mid-IR excess and the excess caused by the broad silicate feature.

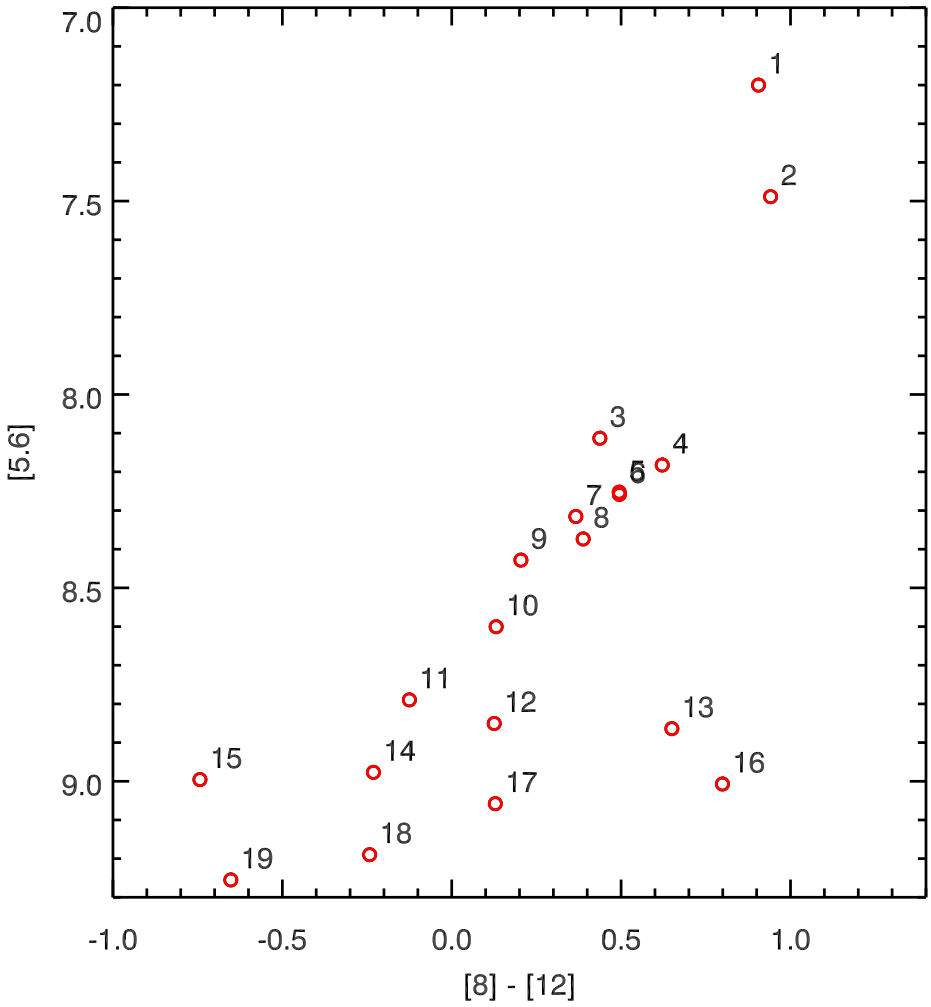

was only a small effect on the best fit $\dot{M}$ found (less than 10%). The only change to the results from making these adjustments was that the $L_{\rm bol}$ was reduced for stars #1 and #2 by approximately 0.3 dex. I discuss these results further in Section 2.3.3.

In Figs. 2.4–2.6 I show contour plots illustrating the degeneracy between the two free parameters, $T_{\rm in}$ and $\tau_{\rm v}$, with $\dot{M}$ contours for the best fit $\dot{M}$ and upper and lower $\dot{M}$ contours overplotted. It can be seen that the lines of equal $\dot{M}$ run approximately parallel to the χ^2 contours. This means that despite the degeneracy between τ_V and $T_{\rm in}$ the value of $\dot{M}$ is well constrained and robust against variations in where I place the inner dust rim.

Fit results for all stars modelled are shown in Table 2. I find differing $T_{\rm in}$ values for the stars in the sample, rather than a constant value at the dust sublimation temperature of 1200K. For each of the stars a best fit value of τ and $T_{\rm in}$ is found. Lower $T_{\rm in}$ values have also been found in other studies (c.f. Groenewegen et al., 2009). When compared to the stars' calculated luminosities, it can be seen that lower luminosity stars have a greater spread in $T_{\rm in}$ values, while higher $\dot{M}$ stars have $T_{\rm in}$ values that are more constrained. I find that all stars in the sample are consistent with $T_{\rm in} \sim$ 600K. $L_{\rm bol}$ is found by integrating under the model spectra with errors on $L_{\rm bol}$ dominated by the uncertainty in $T_{\rm eff}$. The value of A_V is found from the ratio of input and output fluxes at 0.55μm and is intrinsic to the dust shell. For stars numbered 15, 18 and 19 the value of $\dot{M}$ is so low it can be considered as a non-detection, leaving $T_{\rm in}$ unconstrained.

A positive correlation between $\dot{M}$ and luminosity is illustrated in Fig. 2.7, implying that $\dot{M}$ increases by a factor of 40 during the RSG phase, which according to model predictions should last approximately 10^6 years for stars with initial masses of 15M$_\odot$ (Georgy et al., 2013), see Section 3.2. This correlation between $\dot{M}$ and luminosity has a Pearson correlation value of 0.8. This plot also shows some mass-loss rate prescriptions for comparison (assuming a $T_{\rm eff}$ of 4000K); De Jager et al. (1988, hereafter dJ88), Reimers (1975); Kudritzki & Reimers (1978), Van Loon et al. (2005), (Nieuwenhuijzen & De Jager, 1990, hereafter NJ90) and Feast & Whitelock (1992). See Section 3.1.1 for further discussion of the $\dot{M}$ prescriptions. I find the results are best fitted by dJ88, van Loon and Reimer's prescriptions, with dJ88 providing a better fit for the

Figure 2.4: *Left panel:* Model plot for the star with the highest $\dot{M}$ value in NGC 2100 including all contributions to spectrum. The "error models" are the models that fit within the minimum χ^2+10 limit. The silicate bump at 10μm is clearly visible on the spectra suggesting a large amount of circumstellar material. *Right panel:* Contour plot showing the degeneracy between χ^2 values and best fitting $\dot{M}$ values in units of 10^{-6} $M_\odot$ yr^{-1}. The green lines show the best fit $\dot{M}$ and upper and lower $\dot{M}$ isocontours. It can be seen that while there is some degeneracy between inner dust temperature and optical depth the value of $\dot{M}$ is independent of this.

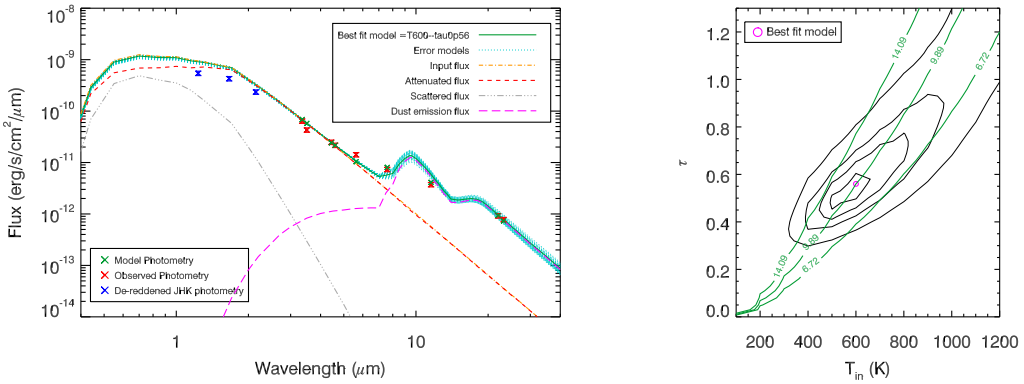

Figure 2.5: Same as Fig. 2.4 for star #8, which has an intermediate $\dot{M}$ value. It can be seen in the model plot (left) that it is possible to fit both the near-IR and mid-IR photometry. $\dot{M}$ values are in units of 10^{-6} $M_\odot$ yr^{-1}.

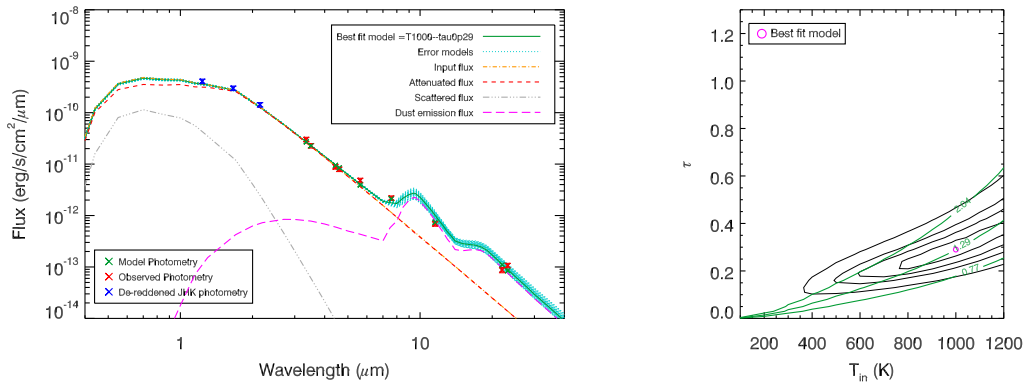

Figure 2.6: Same as Fig. 2.4 for star #12, which has a low $\dot{M}$ value. It can be seen in this plot that it is possible to fit both the near-IR photometry and mid-IR photometry. $\dot{M}$ values are in units of 10^{-6} $M_{\odot}$ yr^{-1}.

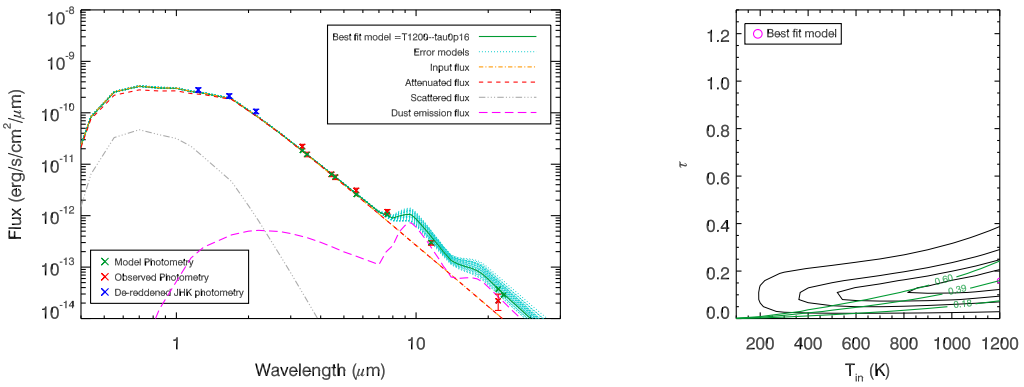

more evolved stars (where the mass-loss mechanism is stronger).

The stars in this work form a tight correlation, whereas previous studies of $\dot{M}$ with $L_{\rm bol}$ (e.g. Van Loon et al. (2005)) have shown a large spread in results. This could be due to previous studies looking at field stars, whereas this study has looked at RSGs in a coeval cluster. As for the three stars with negligible $\dot{M}$ values, it is possible that no appreciable amount of dust has formed around these RSGs yet meaning the dust driven wind has not taken effect. I considered the possibility that these stars were foreground stars but after checking their v_{rad} values (Patrick et al., 2016) I find they are all consistent with being within the cluster.

mass-loss rate prescriptions

Each $\dot{M}$ prescription was calculated using different methods. The $T_{\rm eff}$ was set to 3900K for all prescriptions shown in Fig. 2.7.

The empirical formula for dJ88 was derived by comparing $\dot{M}$ values found from 6 different methods from literature for 271 stars of spectral types O through M. Determination of $\dot{M}$ for M type stars included the modeling of optical metallic absorption lines of nearby RSGs (under the assumption the lines form in the wind; Sanner, 1976) and using mid-IR photometry and hydrodynamics equations to find v_{∞} (Gehrz & Woolf,

1971). This relation is a two parameter fit of $L_{\rm bol}$ and $T_{\rm eff}$. De Jager et al. (1988) found the same $\dot{M}$ value with each method to within the error limits no matter the star's position on the HR-diagram. The NJ90 prescription (Nieuwenhuijzen & De Jager, 1990) is a second formulation of the dJ88 formula, including stellar mass. Due to the narrow mass range for RSGs (8-25$M_{\odot}$) and the very weak dependence on M it has very little effect on the $\dot{M}$ found from this formulation.

Reimers' law (Reimers, 1975; Kudritzki & Reimers, 1978) is a semi-empirical formula derived by measurements of circumstellar absorption lines for companions in binary systems. This has been repeated for 3 such systems only but provides an accurate measurement of $\dot{M}$. The formula depends on surface gravity, g, but can be expressed in terms of R,L and M (in solar units) as shown by Mauron & Josselin (2011).

Van Loon's prescription is an empirical formula based on optical observations of dust-enshrouded RSGs and Asymptotic Giant Branch (AGB) stars within the LMC, where $\dot{M}$ was derived by modeling the mid-IR SED using DUSTY. Van Loon et al. (2005) assumed a constant grain size of 0.1μm, but state that this value was varied for some of the stars to improve fits. $T_{\rm in}$ values were first assumed to be between 1000 and 1200K, but again they state that for some stars in the sample this was reduced to improve the fit of the data and the DUSTY model.

The most widely used $\dot{M}$ prescription, dJ88, provides the best fit to the observations for the more evolved stars. The van Loon prescription overestimates mass-loss for every star in the sample. This is expected due to this study's focus on dust-enshrouded stars, and hence is biased towards higher $\dot{M}$ objects. All of the prescriptions over-predict the $\dot{M}$ for the lowest luminosity stars, though, this may be due to the fact that dust in these stars has yet to form (and hence $r_{gd} > 500$ for these).

2.3.2 Cluster age and initial masses

In order to analyse these questions, it is necessary to know the initial masses of the stars in the cluster. By comparing various stellar evolutionary models, such as that of

Figure 2.7: Plot showing $\dot{M}$ versus $L_{\rm bol}$. A positive correlation can be seen suggesting $\dot{M}$ increases with luminosity, and hence evolutionary stage. This is compared to some mass-loss rate prescriptions. The downward arrows show for which stars I only have upper limits on $\dot{M}$.

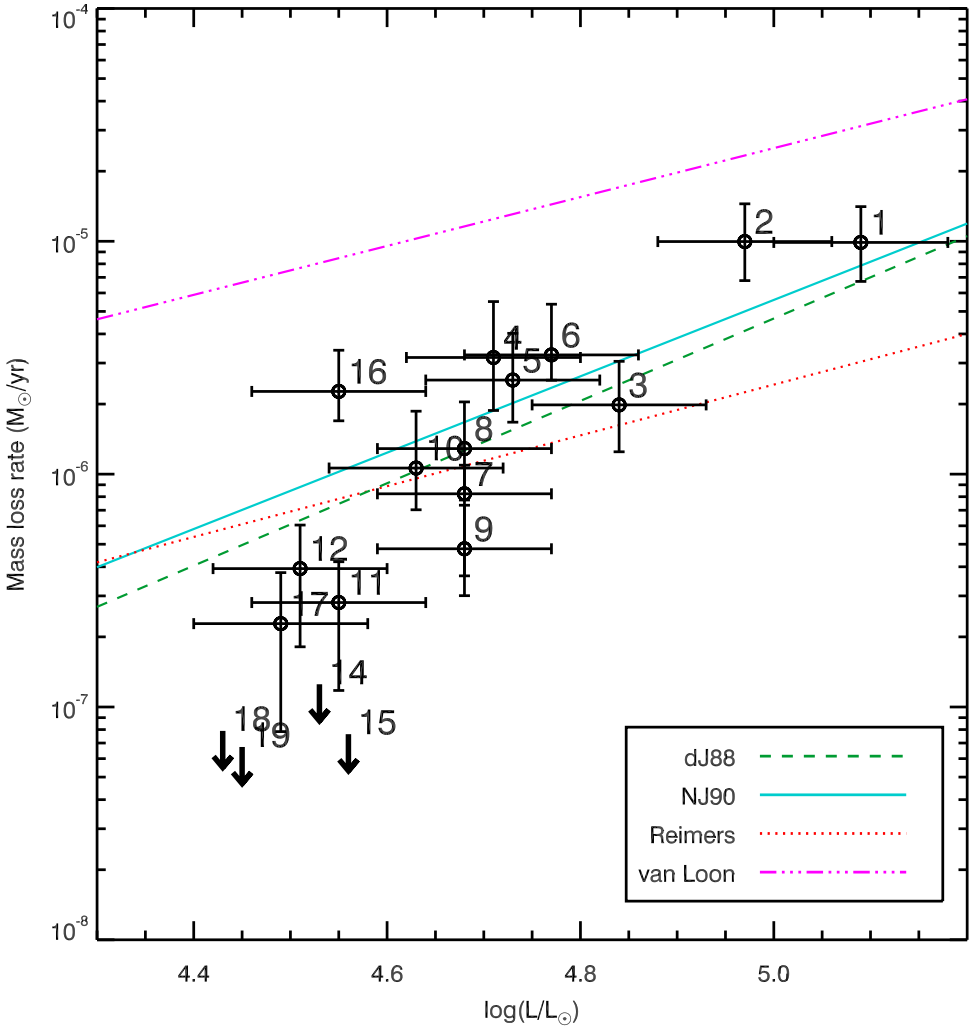

Table 2.3: Results for stars in NGC 2100. Stars are numbered with #1 having the highest [5.6]-band magnitude and #19 having the lowest. Luminosities quoted are in units of $\log(L_{\rm bol}/{\rm L}_\odot)$. A_V is the extinction intrinsic to the dust shell.

Star	$T_{\rm in}$ (K)	τ_V	$\dot{M}$ ($10^{-6}{\rm M}_\odot$ yr^{-1})	$L_{\rm bol}$	A_V
1	600^{+200}_{-100}	$0.56^{+0.21}_{-0.14}$	$9.89^{+4.20}_{-3.17}$	5.09 ± 0.09	$0.09^{+0.04}_{-0.02}$
2	600^{+200}_{-100}	$0.64^{+0.26}_{-0.16}$	$9.97^{+4.52}_{-3.19}$	4.97 ± 0.09	$0.10^{+0.05}_{-0.03}$
3	600^{+400}_{-200}	$0.16^{+0.08}_{-0.05}$	$1.98^{+1.07}_{-0.74}$	4.84 ± 0.09	$0.02^{+0.01}_{-0.01}$
4	800^{+400}_{-200}	$0.45^{+0.32}_{-0.16}$	$3.17^{+2.34}_{-1.29}$	4.71 ± 0.09	$0.07^{+0.06}_{-0.03}$
5	700^{+300}_{-200}	$0.29^{+0.16}_{-0.08}$	$2.54^{+1.49}_{-0.86}$	4.73 ± 0.09	$0.04^{+0.03}_{-0.01}$
6	500^{+300}_{-100}	$0.21^{+0.13}_{-0.02}$	$3.25^{+2.12}_{-0.72}$	4.77 ± 0.09	$0.03^{+0.02}_{-0.00}$
7	1200^{+0}_{-500}	$0.27^{+0.07}_{-0.14}$	$0.82^{+0.27}_{-0.46}$	4.68 ± 0.09	$0.04^{+0.01}_{-0.02}$
8	1000^{+200}_{-400}	$0.29^{+0.16}_{-0.10}$	$1.29^{+0.76}_{-0.51}$	4.68 ± 0.09	$0.04^{+0.03}_{-0.01}$
9	1200^{+0}_{-400}	$0.16^{+0.08}_{-0.05}$	$0.48^{+0.26}_{-0.18}$	4.68 ± 0.09	$0.02^{+0.01}_{-0.01}$
10	600^{+500}_{-200}	$0.11^{+0.08}_{-0.03}$	$1.06^{+0.80}_{-0.36}$	4.63 ± 0.09	$0.01^{+0.01}_{-0.00}$
11	1200^{+0}_{-700}	$0.11^{+0.05}_{-0.06}$	$0.28^{+0.14}_{-0.16}$	4.55 ± 0.09	$0.01^{+0.01}_{-0.01}$
12	1200^{+0}_{-600}	$0.16^{+0.08}_{-0.08}$	$0.39^{+0.21}_{-0.21}$	4.51 ± 0.09	$0.02^{+0.01}_{-0.01}$
14	–	< 0.05	< 0.12	4.53 ± 0.10	–
15	–	< 0.03	< 0.08	4.56 ± 0.09	–
16	400^{+300}_{-100}	$0.13^{+0.06}_{-0.02}$	$2.27^{+1.14}_{-0.57}$	4.55 ± 0.09	$0.020^{+0.010}_{-0.000}$
17	1100^{+100}_{-700}	$0.08^{+0.05}_{-0.05}$	$0.23^{+0.15}_{-0.15}$	4.49 ± 0.09	$0.010^{+0.010}_{-0.010}$
18	–	< 0.03	< 0.08	4.43 ± 0.09	–
19	–	< 0.03	< 0.07	4.45 ± 0.11	–

Brott et al. (2011), STARS (Eldridge & Stanway, 2009) and Geneva (Georgy et al., 2013), and the lowest measured $L_{\rm bol}$ of $\sim$4.5L$_\odot$ as a constraint, see Fig. 2.8, I derived an initial mass for the stars in the sample. It should be noted that Brott et al. (2011)'s mass tracks are not evolved to the end of helium burning, but since I am only interested in the initial mass of the cluster stars this does not affect the conclusions. The current Geneva models at LMC metallicity are currently only available for masses up to 15M$_\odot$, but seem to imply a mass greater than 14M$_\odot$. I conclude that an $M_{\rm initial}$ of $\sim$14M$_\odot$ - 17M$_\odot$ seems most likely.

Cluster age was derived using PARSEC non-rotating isochrones (Tang et al., 2014; Chen et al., 2015) at Z$\sim$0.006. These isochrones were used as they have the added advantage of coming with photometry. I used $M_{\rm initial}$ as a constraint and found an age of 14 Myrs. Patrick et al. (2016) estimated the age of NGC 2100 to be 20 $\pm$ 5 Myr using SYCLIST stellar isochrones (Georgy et al., 2013) at SMC metallicity and at solar metallicity. This difference in cluster age is due to the use of non-rotating isochrones

Figure 2.8: Plot showing $M_{\rm initial}$ vs luminosity for various mass tracks. The plot shows the upper and lower luminosity values at each $M_{\rm initial}$ for STARS (Eldridge & Stanway, 2009) (pink solid lines) at $Z \sim 0.008$, (Brott et al., 2011) non-rotating models at LMC metallicity (green dashed line), and Geneva rotating (red dotted line) and non-rotating (blue dotted line) (Georgy et al., 2013) at LMC metallicity. The Geneva models do not currently cover masses greater than $15M_{\odot}$ at this metallicity. The grey shaded region shows the upper and lower luminosities derived for the stars in the sample. Using the lowest measured $L_{\rm bol}$ of $\sim 4.5L_{\odot}$ as a constraint I find $M_{\rm initial}$ of $\sim 14M_{\odot} - 17M_{\odot}$ from the evolutionary models.

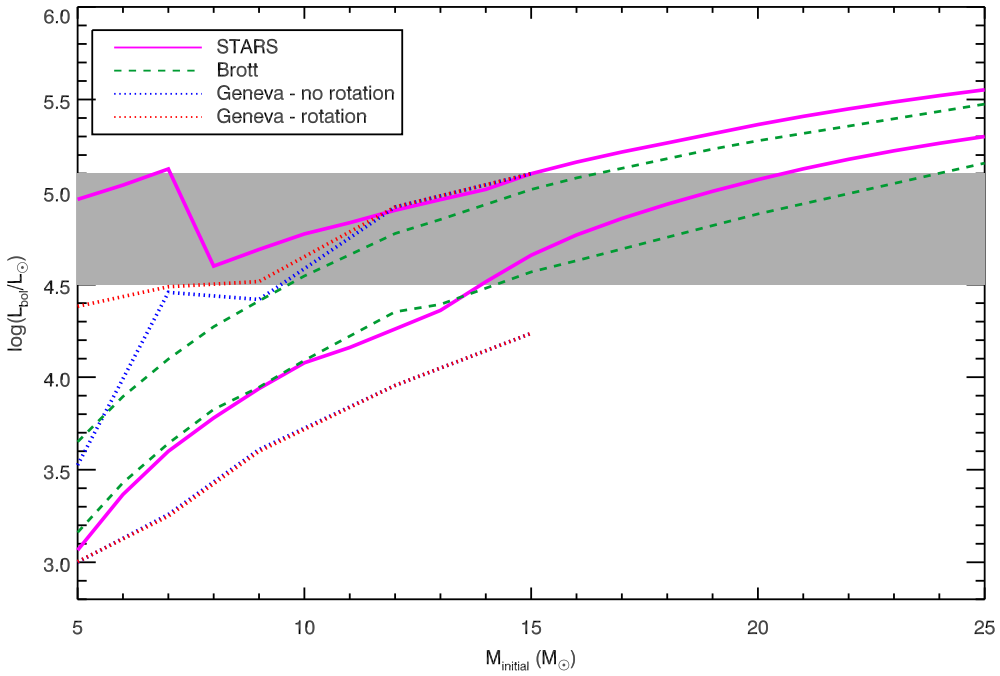

in this study, as it is known that stellar rotation causes stars to live longer, and hence infer an older cluster age. When using rotating isochrones I found the same age.

2.3.3 Extinction

I determined the extinction due to the dust wind from the ratio of the input and output flux at 0.55 μm. This extinction is intrinsic to the circumstellar dust shell and is independent of any foreground extinction. Due to scattering within the dust wind the effect of extinction is small, see Table 2. As discussed by Kochanek et al. (2012), enough light is scattered by the dust shell back into the line of sight of the observer so little flux is lost. In apparent contradiction, Davies et al. (2013) derived extinctions for a sample of RSGs in the SMC and LMC of a few tenths of a magnitude. As the mass

of the progenitor RSGs to the IIP SN are found from mass-luminosity relations, an extinction this high could have an effect on the mass calculation, causing them to be underestimated.

I next fit isochrones to the CMD of the sample and by dereddening this it was possible to further estimate extinction for the RSGs. I used a 14 Myr PARSEC stellar evolutionary track isochrone (Tang et al., 2014; Chen et al., 2015). After adjusting the isochrone to a distance of 50kpc and the extinction law towards the LMC (Koornneef, 1982) I found that there is additional extinction towards the RSGs that is not present for blue supergiants (BSGs) in the cluster, see Fig. 2.2. The isochrone shows that the RSGs require additional extinction in order to fit with the model, with stars #1 and #2 possessing even further extinction (see Section 2.3.3). This is further to the foreground extinction already known to be present for NGC 2100 (around 0.5 mag, Niederhofer et al., 2015). From this I can infer an intrinsic RSG extinction of approximately $A_V \sim 0.5$ that is not present for other stars in the cluster.

I considered the possibility that this extra extinction could be due to cool dust at large radii from the stars that is not detectable in the mid-IR. To do this I created DUSTY models at 30K with an optical depth of 2, large enough to produce the extra extinction of A_V of $\sim$0.5 mags. If this dust were present it would emit at around 100μm with a flux density of > 1 Jy. A flux this high would be within the detection limits for surveys such as Herschel's HERITAGE survey (Meixner et al., 2013), which mapped the SMC and LMC at wavelengths of 100μm and above. After checking this data I found no evidence of the stars within NGC2100 emitting at this wavelength, suggesting that the additional extinction local to RSGs is not caused by a spherically symmetric cold dust shell.

I also considered the effect of differential extinction on the cluster. Niederhofer et al. (2015) found that a low level of differential extinction is present in NGC 2100, but after analysing Herschel 100μm to 250μm images (Meixner et al., 2013) it seems the core of the cluster, where the RSGs are, remains clear of dust. Star #2 is spatially coincident with the BSGs, whereas star #1 is away from the cluster core. From Herschel images I see no reason to expect that the foreground extinction should be unusually high for

these objects. I therefore see no argument for the RSGs having different foregound extinction than the BSGs. Clumpy cold dust at larger radii could potentially explain the extra extinction in RSGs; I investigate this possibility further in Section 2.4.1.

2.3.4 Sensitivity to grain size distribution

To check how robust the results were to a change in the grain size distribution, I created grids of models for various constant grain sizes of 0.1 μm, 0.2 μm, 0.4 μm and 0.5 μm (in addition to the 0.3 μm grain size). The maximum grain size of 0.5 μm was chosen as this was recently found to be the average grain size for dust grains around the well known RSG VY Canis Majoris (Scicluna et al., 2015). I then derived $\dot{M}$ values.

The results can be seen in Fig. 2.9, where the $\dot{M}$ value for each star is plotted for each constant grain size. It is clear that increasing grain size does not have an effect on the derived $\dot{M}$ values. Similarly, the grain size also does not seem to have a significant effect on the value of A_V. This can be seen in Fig. 2.10. The stars chosen are representative of high $\dot{M}$ (#2), intermediate $\dot{M}$ (#7) and low $\dot{M}$ (#9). While the A_V does fluctuate slightly, the values remain within error boundaries of each other. A_v is affected by grain size as described by Mie theory, which states that the scattering efficiency of the dust is dependent on grain size, a. Extinction is dominated by particles of size $\sim\lambda/3$. When $\lambda \gg$ grain size, scattering and absorption efficiency tend to 0. When dust grains are larger than a certain size, fewer particles are needed to reproduce the mid-IR bump causing a reduction in A_V. $\dot{M}$ remains unaffected as the overall mass of the dust shell remains the same whether there are more smaller grains or fewer large grains.

Figure 2.9: Plot showing $\dot{M}$ derived at each constant grain size. Each colour represents a different star from NGC2100. The stars chosen are representative of high $\dot{M}$ (#2), intermediate $\dot{M}$ (#7) and low $\dot{M}$ (#9).

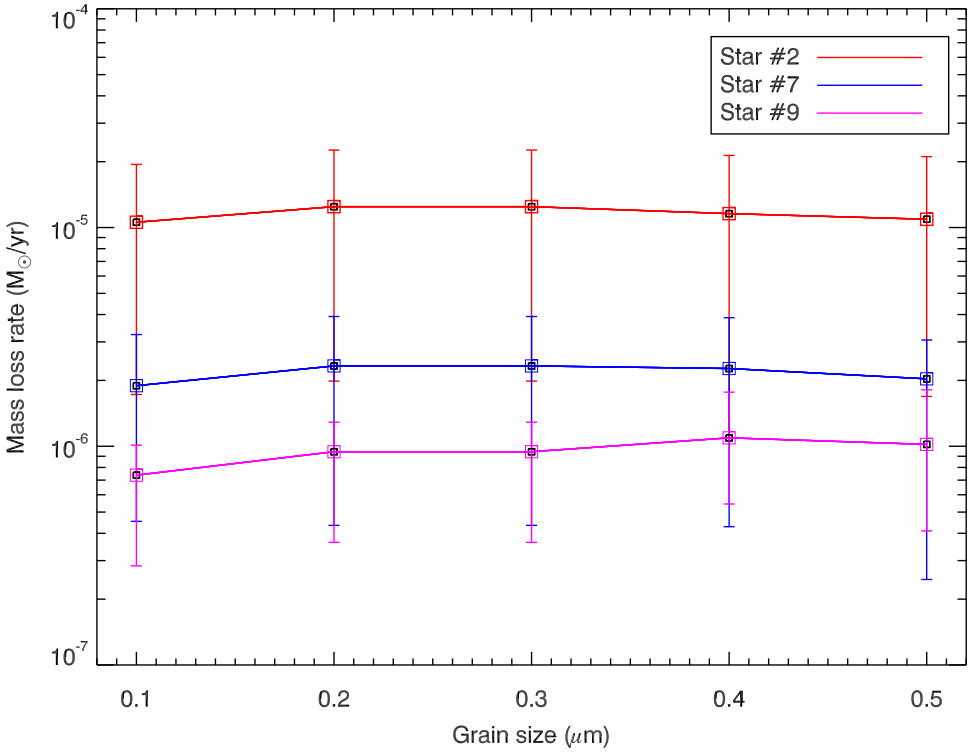

2.4 Discussion

2.4.1 Evidence for enhanced extinction to stars #1 and #2

As discussed in Section 2.3.1, stars #1 and #2 were found to be the most luminous in the sample, as well as having the strongest measured $\dot{M}$ values. From the fitting procedure I found that the near-IR flux for these stars was overestimated by the best fit model spectrum. Possible causes for the discrepant near-IR photometry of these stars will now be discussed.

Next, I included the near-IR photometry into the fitting procedure to see the effect this would have on the output $L_{\rm bol}$. The $L_{\rm bol}$ values were derived by integrating under the best fit model spectrum for each star. As I did not initially include JHK photometry in the fitting procedure, it was possible that the derived $L_{\rm bol}$ would be overestimated also.

Figure 2.10: Plot showing grain size versus A_v. Each colour represents a different star from NGC 2100. The stars chosen are representative of high $\dot{M}$ (#2), intermediate $\dot{M}$ (#7) and low $\dot{M}$ (#9).

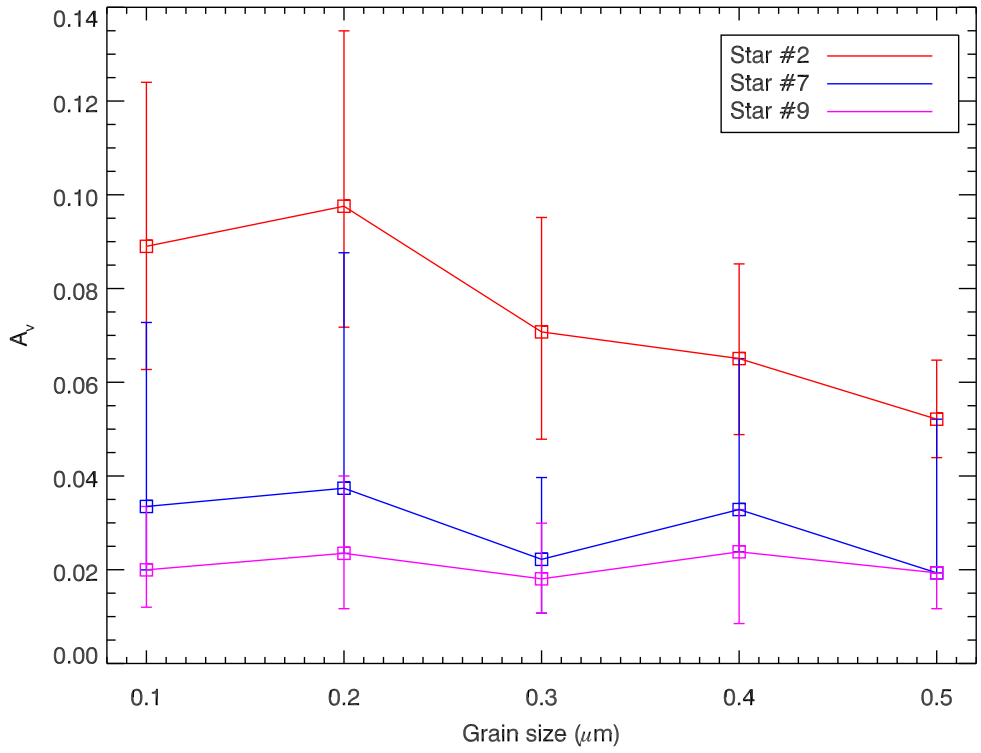

When including the JHK photometry, the fits were improved at near-IR wavelengths but the mid-IR photometry fits became poorer. This had little effect on the best fit $\dot{M}$ values and the trend of increasing $\dot{M}$ with luminosity was still observed, and well modelled by the dJ88 prescription (De Jager et al., 1988), with stars #1 and #2 having lower $L_{\rm bol}$ by $\sim$0.3 dex. As I was unable to reliably fit both the near-IR and mid-IR photometry it can be concluded that stars #1 and #2 were redder than the other, less evolved stars in the sample.

Choice of input SED could also have affected the measured $L_{\rm bol}$ as lower $T_{\rm eff}$ causes the peak of the spectrum to shift to longer wavelengths. The $T_{\rm eff}$ of star #1 has been found to be 4048$\pm$68K (Patrick et al., 2016) so I do not believe the overestimated near-IR flux to be an effect of input SED. Nevertheless, I repeated the fitting procedure using a lower $T_{\rm eff}$ of 3600K finding that this now underestimated the JHK photometry. I also calculated luminosities for each star based on the K-band calibration described

by Davies et al. (2013) and find the integrated luminosities of all stars are consistent with a 1:1 relation within errors except for stars #1 and #2, which were underpredicted by this calibration. This further supports the suggestion that these stars have more self-extinction than the other RSGs in the sample.

After repeating the fitting procedure with lower $T_{\rm eff}$ and to include near-IR photometry I believe the most likely explanation is that stars #1 and #2 have extra extinction that cannot be explained by the inner dust wind. These stars are the most evolved in the sample, so it is possible this enhanced extinction only becomes apparent towards the end of an RSGs' life.

It is known that RSGs have extended clumpy nebulae, for example μ Cep (de Wit et al., 2008). If μ Cep were at the distance of the LMC, the cold dust emitting at 100μm would be too faint to be observable, at a level of around 0.2 Jy (even before I account for a factor of 2 lower dust to gas ratio for the LMC). It is therefore possible that the enhanced extinction I observe for stars #1 and #2 is caused by the stars being surrounded by cold, clumpy dust that emits at similarly low levels.

I considered the possibility that the poor fits to the JHK and mid-IR photometry for stars #1 and #2 is due to extreme variability. If the mid-IR data used in the analysis was taken at a time when the near-IR brightness of these stars was lower than when the 2MASS data were taken, this would cause the best fit SED to overestimate the flux at the JHK wavelengths. Star #1 ($\equiv$HV 6002) is variable in the J and H bands by 0.13 mag and 0.11 mag, respectively (from minimum observed brightness to maximum observed brightness) and the 2MASS photometry I use in the analysis is the peak of this variability. In the V-band this variability is higher ($\sim$0.6 mag). I find that even at maximum brightness, the V-band photometry (corrected for foreground reddening) does not fit with the best fit SED. When I further de-redden the V-band photometry for the intrinsic reddening implied by the difference between the fit and the JHK photometry, I find the V-band photometry fits well with the best fitting SED with no tuning. I therefore conclude variability cannot explain the missing flux at JHK from the mid-IR photometry fits for stars #1 and #2. However, if this extra reddening is attributed to extinction, this could provide a self-consistent explanation.

2.4.2 Effects of using a shallower density distribution

Shenoy et al. (2016) presented a recent study of cool dust around hypergiant stars VY Canis Majoris and μ Cep. Using photometry and DUSTY modeling to derive $\dot{M}$ values, they adopted a fixed inner radius temperature of $T_{\rm in}$=1000K and a power law dust mass density distribution (ρ(r) $\propto$ r^{-q}) with a single index q throughout the shell. They then went on to test a range of optical depths and a range of power law indices $q \leq 2$. They found that a power law with q=2 did not produce enough cool dust to match the long wavelength end of the observed SED, instead concluding that a power law of ρ(r) $\propto$ r$^{-1.8}$ was more appropriate. This implies $\dot{M}$ decreases with time since there was more dust present at large radii than would be for a fixed $\dot{M}$.

By setting a fixed $T_{\rm in}$ at the sublimation temperature for silicate dust Shenoy et al. (2016) are left with not enough cool dust at large radii. However, it is possible that the data could be fit equally well by fixing q=2 and allowing $T_{\rm in}$ to vary. I tested this for μ Cep by creating a model using the best fit parameters found by Shenoy et al. (2016) using the same density distribution ($T_{\rm in}$=1000K, $\tau_{37.2\mu m}$=0.0029 and q=1.8) and then attempted to fit this spectrum using a q=2 density law and allowing $T_{\rm in}$ to vary. I found that a model with an inner dust temperature of 600K and q=2 density law fit Shenoy et al.'s model to better than $\pm$10% at all wavelengths $\leq$70μm, comparable to the typical photometric errors. If I include the 150μm data-point, noting that Shenoy et al.'s best-fit model overpredicted the flux of μ Cep at this wavelength. I can again fit the q=1.8 model with a steady state wind by adjusting the $T_{\rm in}$ value to 500K, giving a fit to better than 15% at all wavelengths.

Shenoy et al. (2016) also fit intensity profiles to the PSF of μ Cep. Models were computed using different density power law indices (q=1.8 and q=2) and a constant inner dust temperature of 1000K. Shenoy et al. concluded the PSF of μ Cep was best matched by an intensity profile of q=1.8 and $T_{\rm in}$ = 1000K out to 25 arcseconds. To check the robustness of this conclusion, I created DUSTY models using the model atmosphere in the grid most similar to that of Shenoy et al. (MARCS, $T_{\rm eff}$ = 3600K), with the same parameters as in Shenoy et al. (q=1.8, $T_{\rm in}$ = 1000K). I then also created

a second DUSTY model using the parameters I found to give an equally good fit to the SED (q=2, $T_{\rm in}$ = 600K, discussed previously). The intensity profiles for both of these models was convolved with the PSF from Shenoy et al. I found the two models to be indistinguishable for both the SED and the intensity profile out to 25 arcseconds. From this I conclude that μ Cep data can be equally well modelled by a steady-state wind and a cooler inner dust temperature.

A density power law index q<2 implies a mass-loss rate that decreases over time. Specifically, if $R_{\rm out}$ = 1000$R_{\rm in}$ then $\dot{M}$ will be found to decrease by a factor of 1000^{2-q} in the time it takes for the dust to travel from $R_{\rm in}$ to $R_{\rm out}$. For q=1.8, $\dot{M}$ would decrease by a factor of 4 through the time it takes for the dust to travel to the outer radius. In the case of μ Cep, Shenoy et al. (2016) concluded that the $\dot{M}$ must have decreased by a factor of 5 (from 5×10^{-6} to 1×10^{-6} $M_{\odot}$ yr^{-1}) over a 13,000 year history. If μ Cep's $\dot{M}$ increases as the star evolves to higher luminosities, as I have found for the RSGs in NGC 2100[1] then this is inconsistent with the conclusions of Shenoy et al. This inconsistency can be reconciled if I assume the winds are steady-state (q=2) and allow $T_{\rm in}$ to be slightly cooler. From the best fit q=2 model I find an $\dot{M}$ value of 3.5×10^{-6}, corresponding approximately to a density-weighted average of Shenoy et al.'s upper and lower mass-loss rates.

As a further test of these conclusions that $\dot{M}$ increases with evolution, I ran the fitting procedure and this time set the $T_{\rm in}$ to a constant value of 1200K. I still find an increase in $\dot{M}$ with evolution. Although the fits at this constant $T_{\rm in}$ are worse at longer wavelengths, the warm dust (i.e. the most recent ejecta) is still accurately matched at shorter wavelengths (<8μm). This relative insensitivity of $\dot{M}$ to the inner dust radius is illustrated in Fig. 2.4, where the contours of constant $\dot{M}$ run parallel to the χ^2 trenches. This shows again the degeneracy of optical depth and $T_{\rm in}$ where many combinations of the two result in the same value of $\dot{M}$. Even when fixing $T_{\rm in}$, I still find a positive correlation between $\dot{M}$ and luminosity.

[1]Although μ Cep has a higher initial mass and metallicity compared to NGC 2100, all evolutionary models predict an increase in luminosity with evolution, with the length of the RSG phase depending on the mass-loss.

2.4.3 Consequences for stellar evolution

I find a clear increase in $\dot{M}$ with RSG evolution, by a factor of $\sim$40 through the lifetime of the star. These results are well described by mass-loss rate prescriptions currently used by some stellar evolution models, particularly dJ88 which matches the $\dot{M}$ of the most evolved RSGs in this study (see Fig. 2.7). I find very little spread of $L_{\rm bol}$ with $\dot{M}$ unlike that observed for field RSGs (e.g. Van Loon et al., 2005). The spread observed in previous results could be due to a varying $M_{\rm initial}$ in the sample stars. By focussing the study on a coeval star cluster I have kept metallicity and initial mass fixed, showing the mass-loss rate prescriptions fit well for LMC metallicity and $M_{\rm initial}$ of 14M$_{\odot}$.

mass-loss due to stellar winds is a hugely important factor in determining the evolution of the most massive stars. There is uncertainty about the total amount of mass lost during the RSG phase, and therefore about the exact nature of the immediate SNe progenitors. Meynet et al. (2015) studied the impact of $\dot{M}$ on RSG lifetimes, evolution and pre-SNe properties by computing stellar models for initial masses between 9 and 25M$_{\odot}$ and increasing the $\dot{M}$ by 10 times and 25 times. The models were computed at solar metallicity (Z$\sim$0.014) for both rotating and non-rotating stars. It was found that stronger $\dot{M}$ had a significant effect on the population of blue, yellow and RSGs. It has been discussed previously that yellow supergiants (YSGs) could be post-RSG objects (e.g. Georgy, 2012; Yoon & Cantiello, 2010), suggesting a possible solution to the "missing" type IIP SNe progenitors. Georgy & Ekström (2015) also discuss the case for an increased $\dot{M}$ during the RSG phase. By increasing the standard $\dot{M}$ by a factor of 3 in the models, Georgy & Ekström (2015) find a blueward motion in the HRD for stars more massive than 25M$_{\odot}$ (non-rotating models) or 20M$_{\odot}$ (rotating models, see Georgy, 2012).

As can be seen in Fig. 2.7 I find the accepted $\dot{M}$ prescriptions commonly used in stellar evolution codes fit well when the variables Z and $M_{\rm initial}$ are fixed. For this $M_{\rm initial}$ ($\sim$15M$_{\odot}$) and at LMC metallicity altering the $\dot{M}$ prescriptions seems unjustified. Increasing the $\dot{M}$ by a factor of 10 (as in Meynet et al., 2015) would result in a strong conflict with the findings presented here.

Application to SNe progenitors and the red supergiant problem

In the previous sections, I have found that the most evolved stars in the cluster appear more reddened than others within the cluster. I now ask the question, if star #1 were to go SN tomorrow, what would we infer about its initial mass from limited photometric information? This is relevant in the context of the "red supergiant problem", first identified by Smartt et al. (2009) and updated in Smartt (2015). Here it is suggested that RSG progenitors to Type IIP SNe are less massive than predicted by stellar evolution theory. Theory and observational studies strongly suggest that the progenitors to Type II-P events are red supergiants (RSGs) and could be anywhere in the range of 8.5 to 25$M_{\odot}$ (e.g. Meynet & Maeder, 2003; Levesque et al., 2005). However, no progenitors appeared in the higher end of this predicted mass range, with an upper limit of 18$M_{\odot}$. Many of the luminosities (and hence masses) in this study were based on upper limit single band magnitudes only. In each Smartt et al. (2009) assumed a spectral type of M0 ($\pm$ 3 subtypes) and hence a BC_v of –1.3 $\pm$ 0.3. The level of extinction considered was estimated from nearby stars or from Milky Way dust maps (Schlegel et al., 1998). The presence of enhanced reddening that may occur at the end of the RSGs' life, such as that observed for the two most evolved stars in this study (#1 and #2), was not considered.

I now apply similar assumptions to those of Smartt et al. (2009) to #1, to see what would be inferred about the star's initial mass were it to explode tomorrow. I find an excess reddening between J-K of 0.2 and an excess between H-K of 0.15, assuming $T_{\rm eff}$ = 3900K. If I attribute this reddening to extinction, this implies an average K_s-band extinction of A_K = 0.23 $\pm$ 0.11, leading to an optical V-band extinction of A_V = 2.1 $\pm$ 1.1 (based on LMC extinction law Koornneef, 1982). If I take this star's measured V-band magnitude (m_V = 13.79; Bonanos et al., 2009) and adjust to $m_{\rm bol}$ using the bolometric correction BCv = –1.3 (in line with Smartt et al., 2009), the measured $L_{\rm bol}$ without considering any extra extinction is $10^{4.33}L_{\odot}$. When I factor in the extra reddening, this increases to $10^{5.14\pm0.44}L_{\odot}$, in good agreement with the luminosity derived from integration under the best fit DUSTY spectra. This increase will have a significant effect on the mass inferred. When extinction is *not* considered a mass of 8$M_{\odot}$ is

found. From mass tracks, I have determined the initial mass of the cluster stars to be in the range of 14M$_\odot$-17M$_\odot$. Hence, the mass determined for the most evolved star in the cluster from single band photometry is clearly underestimated when applying the same assumptions as used by Smartt et al. (2009). When extinction *is* taken into account the mass increases to $\sim$17 $\pm$ 5 M$_\odot$ (in close agreement with the mass inferred from cluster age, see Section 2.3.2).

An alternative explanation for the redder colours of #1 and #2 is that they may have very late spectral type. Indeed, spectral type has been speculated to increase as RSGs evolve (Negueruela et al., 2013; Davies et al., 2013). A colour of (J-K) = 0.17 would imply a supergiant of type M5 (Koornneef, 1983; Elias et al., 1985). If I consider stars #1 and #2 to be of this spectral type, this would require a BC$_v$ of approximately –2.3, giving a luminosity of $\sim 10^{4.73} L_\odot$. This would lead to an inferred mass of 11 M$_\odot$, an increase on the $8 M_\odot$ inferred when the star was assumed to be of type M0, but still lower than the 14M$_\odot$ - 17M$_\odot$ found from mass tracks.

Based on the enhanced reddening I have observed for stars #1 and #2, it is interesting to see what effect an increased level of extinction would have on other progenitors studied by Smartt et al. (2009). I considered three case studies, the progenitors to SN 1999gi, 2001du and 2012ec (of which SN 1999gi and 2001du are based on upper limits, with SN 2012ec having a detection in one band). I have chosen these SNe as they have host galaxies with sub-solar metallicity comparable to the LMC.

- SN 1999gi

  The progenitor site to SN 1999gi was first studied by Smartt et al. (2001), the 3σ detection limit was determined to be m_{F606W} = 24.9 leading to a luminosity estimate of log($L_{\rm bol}$/$L_\odot$)$\sim$4.49 $\pm$ 0.15 and upper mass limit of 14M$_\odot$. The upper limit to this luminosity was revisited by Smartt (2015) and revised upwards to be $10^{4.9}$ once an ad-hoc extinction of A_V = 0.5 was applied. Based on STARS and Geneva models, Smartt (2015) finds the upper limit to the progenitor star's initial mass to be 13M$_\odot$. If I assume the progenitor to SN 1999gi had similar levels of extinction to star #1 (A_V = 2.4, including the ad-hoc extinction applied

by Smartt), this leads to an extra R-band extinction A_R = 1.4 (Koornneef, 1982) and therefore an increase in luminosity of 0.58 dex. This revises the upper limit on initial mass to 23 $M_\odot$, substantially higher than the upper mass originally stated.

- SN 2001du

  This RSG progenitor was observed in the F336W, F555W and F814W bands, which were all non detections. The 3σ upper limit was based on F814W as this waveband is least affected by extinction. From this Smartt et al. (2009) find a luminosity of $\log(L_{\rm bol}/L_\odot)\sim4.57 \pm 0.14$. When including an extra ad hoc A_V = 0.5, Smartt (2015) find the mass of this progenitor to be 10$M_\odot$ and a luminosity of $10^{4.7}L_\odot$. If I again assume additional optical extinction A_V = 1.4 (on top of the ad hoc extinction included by Smartt, 2015) I find an I-band extinction A_I = 0.95 leading to an increase in measured $L_{\rm bol}$ of 0.38 mag. This would revise the upper mass limit for this progenitor to $\sim$ 17 $M_\odot$.

- SN 2012ec

  Finally, I analyse the RSG progenitor to SN 2012ec, originally discussed by Maund et al. (2013). These authors used a foreground reddening of E(B-V)=0.11 and constrained $T_{\rm eff}$ to $<$ 4000K using an upper limit in the F606W band. Using a $F814W$ pre-explosion image the progenitor candidate is found to have a brightness of m_{F814W} = 23.39 $\pm$ 0.18. Maund et al. (2013) estimate the luminosity to be $\log(L_{\rm bol}/L_\odot)$ = 5.15 $\pm$ 0.19 leading to a mass range of 14 - 22 $M_\odot$. If I again apply a similar level of extinction I measure for star #1 to the progenitor of SN 2012ec I infer a luminosity of $\log(L_{\rm bol}/L_\odot)$ = 5.41, leading to a mass of between 22 - 26 $M_\odot$ based on Fig. 2 of Smartt et al. (2009).

From the three cases studied above, I have shown that including similar levels of reddening that I find in the most evolved stars in NGC 2100, the initial mass estimates for Type IIP SN progenitors increase substantially. When applied to all objects in the Smartt et al. (2009) sample this may resolve the inconsistency between theory and observations and hence solve the red supergiant problem.

One argument against extinction being the cause of the red supergiant problem comes from X-ray observations of SNe. Dwarkadas (2014) used the X-ray emission from IIP SNe to estimate the pre-SNe $\dot{M}$ for RSGs, arguing for an upper limit of 10^{-5}M$_{\odot}$yr^{-1}. By using the mass-loss rate - luminosity relation of Mauron & Josselin (2011) and the mass-luminosity relation from STARS models (Eggleton, 1971), this upper limit to the mass-loss rate was transformed into an upper mass limit of 19M$_{\odot}$, in good agreement with Smartt et al. (2009). While this number is in good agreement with Smartt et al. (2009) I estimate that the errors on this measurement must be substantial. Dwarkadas (2014) converts an X-ray luminosity into a value of $\dot{M}$ (a conversion which must have some systematic uncertainties, but as I do not know these I assume them to be consistent with zero) and from this $\dot{M}$ finds a luminosity of the progenitor using the calibration in Mauron & Josselin (2011). This calibration between $\dot{M}$ and luminosity has large dispersion of a factor of ten (see Fig. 5 of Mauron & Josselin, 2011), but if I am again optimistic take these to be half that, a factor of five. From this, a progenitor mass was calculated under the assumption from mass-luminosity relation for which RSG luminosity scales as L $\sim$ M$^{2.3}$, increasing the errors further. Even with these optimistic estimates, I find the error to be a factor of two, or around 19$\pm$10M$_{\odot}$. Therefore, I conclude that X-ray observations of IIP SNe provide only a weak constraint on the maximum initial mass of the progenitor star, and cannot rule out that circumstellar extinction is causing progenitor star masses to be underestimated.

2.5 Conclusion

Understanding the nature of the mass-loss mechanism present in RSGs remains an important field of study in stellar astrophysics. Here a method of deriving various stellar parameters, $T_{\rm in}$, τ_V, $\dot{M}$ was presented as well as evidence for an increasing value of $\dot{M}$ with RSG evolution. By targetting stars in a coeval cluster it was possible to study $\dot{M}$ while keeping metallicity, age and $M_{\rm initial}$ constrained. As all stars currently in the RSG phase will have the same initial mass to within a few tenths of a solar mass, it is possible to use luminosity as a proxy for evolution, due to those stars with

slightly higher masses evolving through the HR diagram at slightly faster rates. From this study I can conclude the following:

- The most luminous stars were found to have the highest value of $\dot{M}$ evidenced observationally by colour-magnitude diagrams and also by a positive correlation between bolometric luminosity and $\dot{M}$.
- The results are well modelled by various mass-loss rate prescriptions currently used by some stellar evolution groups, such as dJ88 and Reimer's, with dJ88 providing a better fit for the RSGs with stronger $\dot{M}$. I therefore see no evidence for a significantly increased $\dot{M}$ rate during the RSG phase as has been suggested by various stellar evolutionary groups
- I also presented extinction values for each star, first determined from DUSTY models and next determined by isochrone fitting. While the warm dust created low extinction values in the optical range ($A_V \sim$0.01 mag), isochrone fitting showed that RSGs may have an intrinsic optical extinction of approximately A_V = 0.5mag. This extinction cannot come from the warm inner dust, but may come from clumpy cool dust at larger radii. This supports the suggestion that RSGs create their own extinction, more so than other stars in the same cluster.
- I also find that the two most luminous (therefore most evolved) stars in the sample show enhanced levels of reddening compared to the other RSGs. If I attribute this reddening to further extinction, this implies an average K_S-band extinction of A_K = 0.23 $\pm$ 0.11. I do not find evidence for cold dust emitting at wavelengths of 100μm as first suspected, so as yet do not know the source of this extra reddening towards the RSGs.
- When taking the enhanced reddening into account it seems the inferred progenitor masses to Type II-P SNe often increase significantly, providing a potential solution to the red supergiant problem. If this level of extinction is applied to all known RSG progenitors (assuming all RSGs show enhanced reddening at the end of their lives) the inconsistency between theory and observations may be resolved.

Chapter 3

The Evolution of Red Supergiants to Supernova II: Galactic clusters

3.1 Introduction

The work presented in this Chapter has been published as Beasor & Davies (2018). The data analysis and interpretation were conducted by E. R. Beasor. The initial draft of the publication was written by E. R. Beasor, who then incorporated comments from co-authors and from an anonymous referee in the final draft.

In the previous chapter I showed that the dispersion in the $\dot{M}$-$L_{\rm bol}$ relation is reduced when looking at RSGs in a cluster, where all of the RSGs can be assumed to have the same metallicity, the same age and similar initial mass. $\dot{M}$ and luminosities were derived for RSGs in NGC 2100, a cluster in the Large Magellanic Cloud (LMC), finding a tight correlation between $\dot{M}$ and luminosity with little scatter. This suggests that the origin for the dispersion in previous $\dot{M}$ studies comes from differences in initial masses of the stars, their metallicities, or a combination of the two. In Chapter 2 it was also shown that $\dot{M}$ increases as a star evolves, and that there is little justification for increasing $\dot{M}$ by more than a factor of 2 during the RSG phase (as suggested by Georgy (2012)).

I now present a similar study, this time focussing on two Galactic clusters, NGC 7419 and χ Per. Both clusters contain RSGs at different evolutionary stages all of a similar initial mass and solar metallicity. Using near and mid-IR photometry I have derived $\dot{M}$values and luminosities for 13 RSGs, allowing a study of how $\dot{M}$ changes with evolution at a fixed metallicity. In Section 3.2 I discuss the modelling procedure and justifications for the parameters chosen. In Section 3.3.2 I discuss the application of the fitting methodology to Galactic clusters NGC 7419 and χ Per and the results I derive. In Section 3.5 I compare the results with commonly used $\dot{M}$ prescriptions, and calculate the total mass lost for an RSG of a given initial mass during the RSG phase. In Section 3.6 I present the conclusions.

3.2 Application to Galactic clusters

3.2.1 Sample selection

In this paper I have chosen to study the Galactic clusters NGC 7419 and χ Per (also known as NGC 884), both of which contain a number of RSGs at Solar metallicity. These clusters have been found to be of similar ages ($\sim$ 14 Myr, Marco & Negueruela, 2013; Currie et al., 2010), which means all of the RSGs within each cluster have comparable initial masses (in this case 16 $M_{\odot}$, see Section 3.2.2). As the RSG phase is short ($\sim 10^6$yrs, Georgy et al., 2013) I can assume the stars are all coeval, i.e. any spread in age between the stars is small compared to the lifetime of the cluster. A coeval set of RSGs also allows us to use luminosity as a proxy for evolution, since those stars with higher luminosities have evolved slightly further up the RSG branch.

The photometry used in this work is shown in Table 3.1 and is taken from 2MASS, WISE and MSX (Skrutskie et al., 2006; Wright et al., 2010; Price et al., 2001). The stars selected were known cluster members. For χ Per I picked RSGs within 6′ of cluster centre, which is the distance to the edge of the h & χ Per complex, to maximise the probability that the stars were cluster members and hence were formed at the same time. However, Currie et al. (2010) showed that everything within the h & χ Per

complex, including the surrounding region, is the same age to within the errors.

3.2.2 Initial masses

To estimate initial masses for the RSGs, we need to know the age of the cluster. I have taken the best fit isochrone for both clusters ($\sim$ 14Myr from Padova isochrones, Marco & Negueruela, 2013; Currie et al., 2010) as well as Geneva rotating and non-rotating isochrones. I compare the best fit turn off mass to that of other evolutionary models to determine a model-dependent age for each cluster, and therefore the model-dependent mass for the RSGs. From this, I am also able to ensure that we are comparing a self-consistent age and mass for each evolutionary model.

From the original Padova isochrone, a turn-off mass of $14M_{\odot}$ is found and an RSG mass of $\sim$ $14.5M_{\odot}$ for both clusters. The non-rotating Geneva models suggest the cluster's turn-off mass is best fit by a 10Myr isochrone, giving an RSG mass of 17-$18M_{\odot}$. The rotating models suggest an age of 14Myrs, with an RSG mass of 15-$16M_{\odot}$. For the rest of this chapter I will assume the initial mass for the stars across both MW clusters is $16M_{\odot}$, in between the rotating and non-rotating estimates[1].

[1]The evolutionary models suggest that for a single age cluster (e.g. Geneva rotating, 14 Myrs) the difference in initial mass between stars at the start and the end of the RSG phase is $\sim$$0.8M_{\odot}$. A significant dispersion in initial masses between the RSGs in this sample is therefore unlikely.

Table 3.1: Observational data for RSGs in χ Per & NGC 7419. All fluxes are in units of Jy. All photometry for WISE 1 and 2 are upper limits.

Name	2MASS-J	2MASS-H	2MASS-Ks	WISE1 (3.4 μm)	WISE2 (4.6 μm)	WISE3 (11.6 μm)	WISE4 (22 μm)	MSX-A	MSX-C	MSX-D	MSX-E
FZ Per	48.18± 3.22	70.32± 4.84	67.79± 6.56	–	<64.90	9.33± 0.06	4.43± 0.06	12.20	10.90	6.52	4.13
RS Per	95.69± 6.83	146.93± 13.38	158.20± 21.27	< 952.05	<317.56	51.70± 39.43	43.88± 0.07	57.60	59.50	42.80	41.10
AD Per	70.94 ± 4.95	104.30 ± 8.66	111.38 ± 14.90	< 349.83	< 115.72	18.09 ± 2.05	11.16 ± 0.36	20.80	20.40	13.10	11.30
V439 Per	35.52 ± 2.46	52.71 ± 3.80	55.98 ± 6.24	< 119.42	< 45.69	4.29 ± 0.05	1.85 ± 0.02	7.33	5.18	3.20	2.39
V403 Per	25.85 ± 0.00	42.22 ± 0.00	42.66 ± 14.29	< 0.23	< 0.02	2.89 ± 0.02	0.93 ± 0.01	5.31	2.71	1.83	-1.86
V441 Per	65.12 ± 4.84	105.66 ± 9.43	101.76 ± 11.87	< 511.75	< 165.28	16.54 ± 1.17	11.55 ± 0.47	19.30	16.80	13.30	11.10
SU Per	118.27 ± 10.64	173.42 ± 16.55	174.58 ± 26.64	< 1099.16	< 315.23	39.14 ± 25.30	27.13 ± 0.11	43.80	40.00	24.10	30.10
BU Per	53.91 ± 4.28	86.84 ± 6.61	88.39 ± 9.27	< 467.15	< 170.70	32.05 ± 1057.73	28.15 ± 0.11	33.10	36.70	26.30	30.20
MY Cep	23.40 ± 1.43	65.81 ± 5.34	93.07 ± 12.10	< 712.95	< 239.12	76.04 ± 28.26	81.94 ± 0.03	87.80	134.00	97.00	97.70
BMD 139	6.00 ± 0.02	16.02 ± 0.13	17.75 ± 0.16	< 0.56	< 0.49	0.10 ± 0.00	0.12 ± 0.00	3.39	2.41	1.58	-2.45
BMD 921	5.54 ± 0.02	12.32 ± 0.08	13.50 ± 0.05	< 9.45	< 5.64	0.91 ± 0.00	0.39 ± 0.00	1.71	0.71	0.74	-2.23
BMD 696	8.17 ± 0.03	13.98 ± 0.64	20.61 ± 0.20	< 31.01	< 9.35	2.12 ± 0.01	1.03 ± 0.01	3.40	2.00	1.68	-2.23
BMD 435	8.88 ± 0.03	14.99 ± 0.75	16.80 ± 1.19	< 0.60	< 1.12	0.26 ± 0.00	0.27 ± 0.00	3.43	2.11	1.33	3.62

3.3 Dust shell models

The dust shell models used in this project were made using DUSTY (Ivezic et al., 1999) which solves the radiative transfer equation for a central star surrounded by a spherical dust shell of a certain optical depth (τ_V, optical depth at 0.55μm), inner dust temperature ($T_{\rm in}$) at the inner most radius ($R_{\rm in}$) and radial density profile (ρ_r). Below I briefly describe the choices for the model input parameters and the fitting methodology; for an in-depth discussion see Chapter 2.

3.3.1 Model Setup

The dust layer surrounding RSGs absorbs and reprocesses the light emitted from the star, with different compositions of dust affecting the spectral energy distribution (SED) in different ways. I have opted for oxygen-rich dust as specified by Draine & Lee (1984) and a grain size of 0.3μm (e.g. Smith et al., 2001; Scicluna et al., 2015).

To calculate mass-loss rates I have assumed a steady-state density distribution falling off as r^{-2}. Departure from this law has been suggested for some RSGs (e.g. Shenoy et al., 2016), a matter which I discuss in detail in Chapter 2. As I do not have outflow velocity measurements for the RSGs in the sample, I have assumed a uniform speed of 25$\pm$5 km s^{-1}, consistent with previous measurements (e.g. Van Loon et al., 2001; Richards & Yates, 1998).

I have also assumed a gas-to-dust ratio ($r_{\rm gd}$) of 200 and a grain bulk density ($\rho_{\rm d}$) of 3 g cm^{-3}. From this, I can then calculate $\dot{M}$ values from the following equation

$$\dot{M} = \frac{16\pi}{3} \frac{R_{in} \tau_V \rho_d a v_\infty}{Q_V} r_{gd} \tag{3.1}$$

where Q_V is the extinction efficiency of the dust (as defined by the dust grain composition, Draine & Lee, 1984).

The stellar effective temperature $T_{\rm eff}$ changes the position of the peak wavelength of

the SED. For NGC 884, the RSGs are of spectral types M0 - M3.5, corresponding to an approximate temperature range of 3600K - 4000K (taken from the temperature scale of Levesque et al., 2005). In contrast Gazak et al. (2014) found a narrower $T_{\rm eff}$ spread among the stars in χ Per, 3720K - 4040K. In this work, I have opted for a fiducial SED of 3900K for the analysis of this cluster, with the errors on $L_{\rm bol}$ found by rerunning the analysis with SEDs of temperatures $\pm$ 300K fully encompassing the observed range of both Gazak et al. (2014) and Levesque et al. (2005).

For the NGC 7419 RSGs, the spectral types range from M0 to M7.5 (Marco & Negueruela, 2013) corresponding to a temperature range of 3400 - 3800K. For this cluster, I chose to use a fiducial SED of 3600K with further analysis completed using SEDs at 3400K and 3800K.

To ensure the robustness of these $T_{\rm eff}$ assumptions I also systematically altered the fiducial value for each cluster and re-derived luminosities and $\dot{M}$. By doing this I found that altering the $T_{\rm eff}$ by $\pm$300K caused the value of $\dot{M}$ to change by $\pm$5%, while luminosity was affected by around 0.1 dex.

In this study, I have again allowed $T_{\rm in}$ and τ_V to be free parameters to be optimised by the fitting procedure. $T_{\rm in}$ defines the temperature of the inner dust shell (and hence its position, $R_{\rm in}$) while optical depth determines the dust shell mass. The fitting methodology is described in the next subsection.

3.3.2 Fitting methodology

I computed two grids of dust shell models for each SED spanning a range of inner temperatures and optical depths. The first grid spanned τ_V values of 0 - 1.3, while the second grid spanned τ_V values of 0 - 4, each having 50 grid points, and each having $T_{\rm in}$ values of 0 - 1200K in steps of 100K[2]. For each model output spectrum, I created synthetic photometry by convolving the model spectrum with the relevant filter profile. By using χ^2 minimisation I determined the best fitting model to the sample SED, as in

[2]For MY Cep, as the τ_V range in the initial model grid was not high enough to match the observed luminosity, I had to use a coarser model grid with a large range of τ_V values.

Section 2.2.2.

Some of the photometric points used in this study were upper limits, and therefore these data were used to exclude models for which the synthetic photometry exceeded these limits. As well as this, any photometric point that had an error of $<10\%$ had a blanket error of 10% applied to account for systematic errors. As with the previous chapter, the errors on the fitting results are defined as the minimum χ^2 value + 10, to allow stars with the lowest measured $\dot{M}$ values which were clearly consistent with non-detections to have $\dot{M}$ values that are upper limits only.

3.4 Modelling results

I ran the fitting procedure for all of the RSGs in this sample. The results for χ Per and NGC 7419 are shown in Table 3.2. Figure 3.1 shows the best-fit model for the brightest star in these clusters, SU Per, with all contributions to the output spectrum. The left panel of the plot shows the best fit model spectrum (green line), the models within the error range (blue dotted lines) as well as the photometric points, where the black crosses shown the real photometry and orange circles show the model photometry. The right hand panel shows the best-fit model located on a $T_{\rm in}$ - τ plane with the mass-loss rate isocontours overplotted.

Both clusters are affected by foreground reddening. To correct for this I used the published extinction laws for the 2MASS, MSX and WISE photometry (Koornneef, 1983; Messineo et al., 2005; Gontcharov, 2016). I adopted foreground V-band extinctions of 1.66 and 5.27 for the clusters χ Per and NGC 7419 respectively (Currie et al., 2010; Marco & Negueruela, 2013). There is evidence that differential extinction is present in each cluster. For χ Per, Currie et al. (2010) find a V-band dispersion of 0.09 mag (estimated from J-K colours), equivalent to $\sim$0.01 mag in $K_{\rm s}$. This level of differential extinction is smaller than the errors on the photometry and hence will not affect the modelling results. Similarly, the differential reddening across NGC 7419 is approximately 0.2 mag in $K_{\rm s}$ (Marco & Negueruela, 2013, where individual reddenings were

Figure 3.1: *Left panel:* Model plot for SU Per including all contributions to the spectrum. The "error models" are the models that fit within the minimum χ^2+10 limit. The silicate bump at 10μm is clearly visible on the spectra suggesting a large amount of circumstellar material. *Right panel:* Contour plot showing the degeneracy between χ^2 values and best fitting $\dot{M}$ values in units of 10^{-6} $M_\odot$ yr^{-1}. The red contour highlights the models within the minimum χ^2+10 limit.

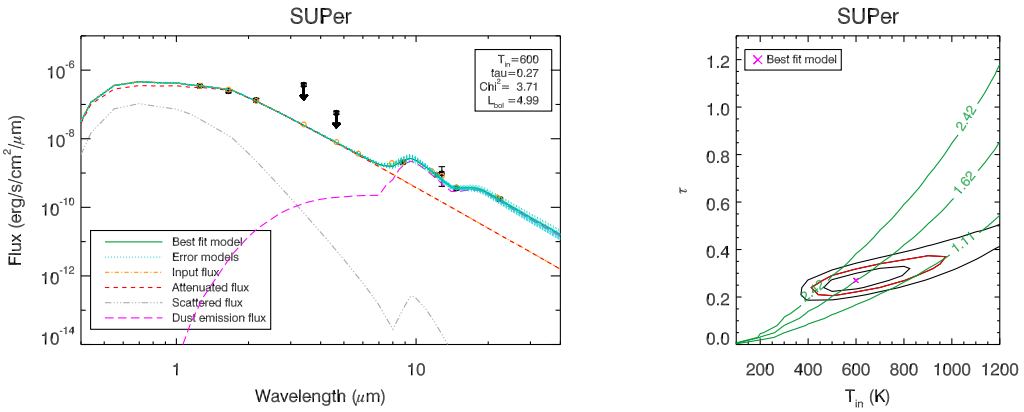

calculated for all cluster members), comparable to the photometric error.

The results of the modelling for all stars in the clusters are shown in Table 3.2. The luminosities are bolometric as found in Davies & Beasor (2017) where possible, otherwise they are calculated by integrating under the best fit spectra with errors on $L_{\rm bol}$ dominated by the uncertainty in $T_{\rm eff}$. It can be seen that the stars with the highest mass-loss rates have inner dust temperatures that are more constrained, while lower $\dot{M}$ stars show a larger spread in $T_{\rm in}$. I also find that the best fits were achieved when allowing $T_{\rm in}$ to vary from the dust sublimation temperature of 1200K. For the stars with the highest $\dot{M}$ $T_{\rm in}$ is typically around 600K rather than the canonical 1200K dust sublimation temperature. For B921, as I could only place an upper limit on the optical depth it was not possible to constrain an inner dust temperature, and hence I have plotted an upper limit for the value of $\dot{M}$.

When plotting $L_{\rm bol}$ versus $\dot{M}$ a clear positive correlation can be seen (see Fig. 3.2), demonstrating an increasing $\dot{M}$ with evolution. The Pearson correlation factors for χ Per and NGC 7419 are 0.66 and 0.97 respectively. I also include results from NGC 2100. Overplotted are also some commonly used $\dot{M}$ prescriptions (assuming a $T_{\rm eff}$ of 3900K), including; De Jager et al. (1988), Reimers (1975), Van Loon et al. (2005) and

Table 3.2: Fitting results for the RSGs in χ Per and NGC 7419. Bolometric luminosities are from Davies & Beasor (2017).

Star	$T_{\rm in}$ (K)	τ_V	$\dot{M}$ (10^{-6}M$_\odot$ yr^{-1})	$L_{\rm bol}$
FZ Per	1000^{+200}_{-400}	$0.19^{+0.08}_{-0.06}$	$0.30^{+0.18}_{-0.07}$	$4.64^{+0.06}_{-0.05}$
RS Per	600^{+200}_{-200}	$0.53^{+0.13}_{-0.08}$	$3.03^{+2.31}_{-0.94}$	$4.92^{+0.18}_{-0.07}$
AD Per	600^{+600}_{-100}	$0.21^{+0.16}_{-0.02}$	$0.97^{+0.33}_{-0.50}$	$4.80^{+0.08}_{-0.05}$
V439 Per	1200^{+0}_{-500}	$0.11^{+0.02}_{-0.03}$	$0.10^{+0.10}_{-0.01}$	$4.53^{+0.06}_{-0.05}$
V403 Per	1200^{+0}_{-400}	$0.08^{+0.00}_{-0.03}$	$0.06^{+0.02}_{-0.02}$	$4.41^{+0.06}_{-0.05}$
V441 Per	600^{+300}_{-200}	$0.21^{+0.08}_{-0.02}$	$0.93^{+0.72}_{-0.31}$	$4.75^{+0.10}_{-0.06}$
SU Per	600^{+300}_{-100}	$0.27^{+0.10}_{-0.06}$	$1.62^{+0.72}_{-0.63}$	$4.99^{+0.09}_{-0.05}$
BU Per	500^{+200}_{-100}	$0.56^{+0.10}_{-0.08}$	$3.24^{+1.53}_{-1.28}$	$4.67^{+0.07}_{-0.05}$
MY Cep	600^{+200}_{-100}	$2.04^{+0.41}_{-0.33}$	$18.04^{+7.15}_{-8.54}$	5.19 ± 0.07
BMD 139	900^{+300}_{-400}	$0.16^{+0.08}_{-0.00}$	$0.27^{+0.44}_{-0.05}$	4.55 ± 0.08
BMD 921=56	$-$	< 0.03	< 0.06	4.45 ± 0.10
BMD 696=122	700^{+500}_{-200}	$0.08^{+0.08}_{-0.00}$	$0.22^{+0.17}_{-0.04}$	4.63 ± 0.08
BMD 435	1100^{+100}_{-300}	$0.16^{+0.08}_{-0.00}$	$0.18^{+0.15}_{-0.04}$	4.54 ± 0.11

Goldman et al. (2017).

3.5 Discussion

3.5.1 The $\dot{M}$ - Luminosity Relation

There are many empirical studies of RSG mass-loss (e.g. Reimers, 1975; De Jager et al., 1988; Van Loon et al., 2005; De Beck et al., 2010; Bonanos et al., 2010; Goldman et al., 2017) all showing significant scatter. For example the calibration of Mauron & Josselin (2011) has a large peak-to-peak dispersion of a factor of $\sim$ 10. As these previous studies have focussed on field stars only, this internal scatter may be caused by inhomogeneity in the initial masses and/or metallicities of the stars in their samples (i.e. the stars are of different masses and ages at the same luminosity).

Goldman et al. (2017) studied RSG winds across a range of metallicities, stating that lower metallicity environments yield slower wind speeds for stars. As $\dot{M}$ is directly proportional to the expansion velocity of the wind (see Equation 3.1), a lower wind speed will result in a lower derived $\dot{M}$. Goldman et al. (2017) measure a relation be-

tween the expansion velocity of the wind and metallicity ($v_{\rm exp} \propto ZL^{0.4}$), with derived expansion velocities then being compared to mass-loss rates. From this I can estimate how large the effect of varying metallicity is on $\dot{M}$. It is therefore possible that the $v_{\rm exp}$ I have assumed for the RSGs in NGC 2100 (an LMC metallicity cluster) is systematically high. However, I estimate this would reduce the $\dot{M}$ values for these stars by around 25%, bringing these results into even better agreement with the Galactic clusters. The effect of varying metallicity is therefore unlikely to be enough to cause the factor of 10 scatter seen in previous relations.

The RSGs I have observed in NGC 2100, χ Per and NGC 7419 are all of a similar initial mass, but different metallicities (LMC, solar and solar, respectively). Despite this, there is still a tight correlation when all of the clusters are plotted together, Fig. 3.2, suggesting $\dot{M}$ is only weakly dependent on the metallicity[3]. Though the results are within an order or magnitude of the DJ88 law, this law overestimated $\dot{M}$ at low luminosities. The Van Loon et al. (2005) and Goldman et al. (2017) prescriptions both vastly overestimate $\dot{M}$ at all luminosities compared to the results presented here. This is likely due to these studies focussing on heavily dust enshrouded stars and/or maser emitters respectively, leaving their samples skewed to stars with the highest $\dot{M}$. These studies may be selecting stars near the end of their evolution, or with peculiar properties (for example, binarity). As the RSGs in this sample continue to evolve up the RSG branch, it is possible that they would eventually reach $\dot{M}$ values as high as those observed for the Goldman et al. (2017) and Van Loon et al. (2005) samples.

As all of the clusters I have looked at have been of a similar initial mass, I combine them to present a mass-loss rate prescription that will be applicable to stars of 16M$_{\odot}$ (Equation 3.2). As previously mentioned, this study suggests $\dot{M}$ is only weakly dependent on metallicity between solar and LMC and hence this relation depends principally on the luminosity of the star. A linear best-fit to the data yield the relation,

$$\log(\dot{M}/M_{\odot}yr^{-1}) = a + b\log(L_{\rm bol}/L_{\odot}) \tag{3.2}$$

[3]I have assumed a gas-to-dust ratios for each cluster, and I have also assumed the same expansion velocity for all clusters. This may be dependent on metallicity (Goldman et al., 2017).

Figure 3.2: $\dot{M}$ versus $L_{\rm bol}$ for all clusters studied. Also overplotted is the $\dot{M}$- luminosity relation for a 16M$_\odot$ star from several literature studies and this thesis.

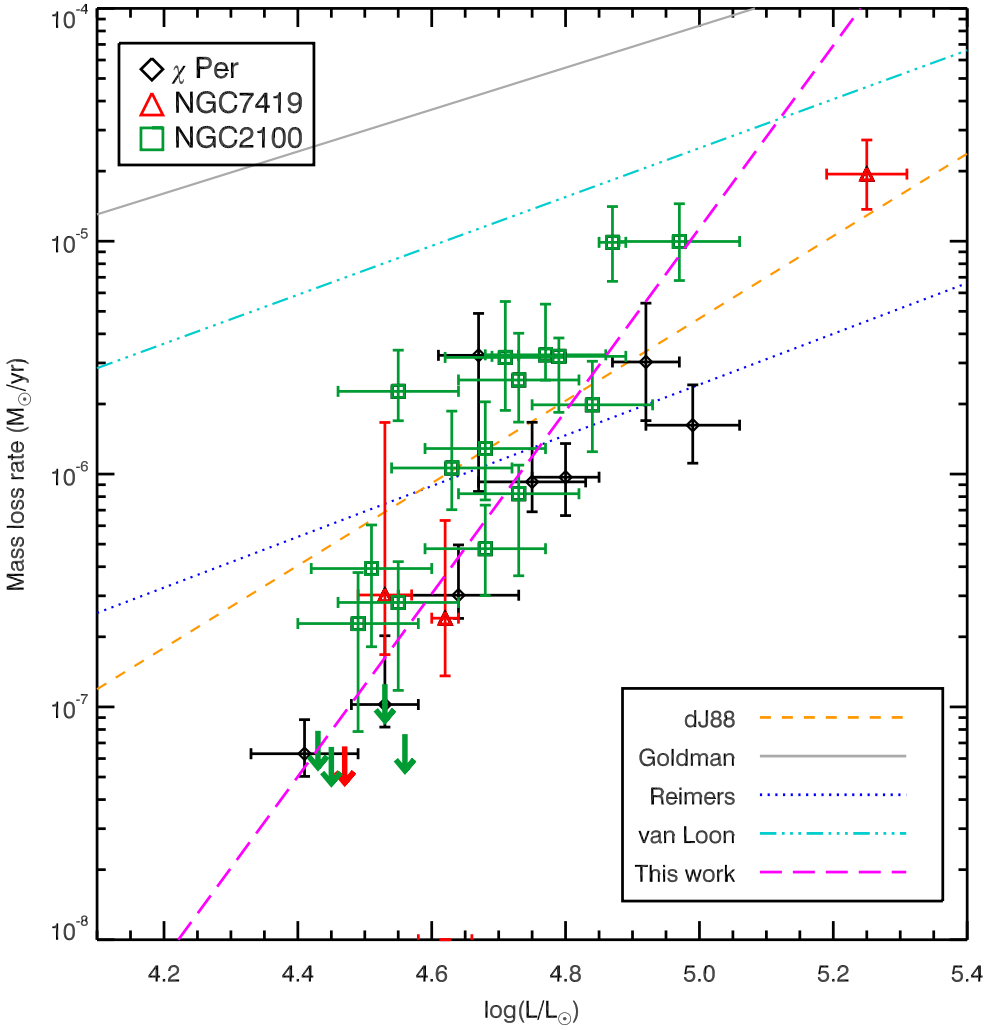

where a = -24.56 $\pm$ 1.65 and b = 3.92 $\pm$ 0.35, derived using IDL program FITEXY. I find a much steeper relation between mass-loss and luminosity than previous studies, with a root mean square scatter of $\pm$0.4 dex. The $\dot{M}$-$L_{\rm bol}$ relation found here suggests that when stars first join the RSG phase they have very low mass-loss rates, implied by the small amount of circumstellar material present. The mass-loss rate then increases by a factor of 100 throughout the RSG lifetime [4], while luminosity increases by only a factor of $\sim$5.

3.5.2 The luminosity distribution of RSGs

To determine the mass-loss rate at a given time-step, stellar evolution calculations use a mass-loss rate prescription (usually dJ88) in conjunction with the star's luminosity at that time step. If the luminosity is incorrectly estimated the adopted mass-loss rate during this phase will also be incorrect.

It is possible to test the implementation of $\dot{M}$ in evolutionary models by looking at luminosity distributions. Luminosity distributions were generated by uniformly sampling RSG masses from a standard Salpeter IMF and assuming a uniform age for all stars. I simulated a large number of stars (10^5) within the relevant mass range and then normalised the distribution to match the total number of stars across both MW clusters. I have also included the effect of measurement errors on the simulated luminosity distributions.

Figure 3.3 shows a comparison for the luminosity distribution of the RSGs[5] in the two MW clusters compared to the predicted luminosity distribution for 13 RSGs in the best fit Geneva non-rotating and Geneva rotating models (see Section 3.2.2). The observed luminosity distribution for the RSGs in the two clusters is peaked at a luminosity of log(L/L$_\odot$) $\sim$ 4.5, see the top panel of Fig. 3.3. As the age spread between the RSGs in this sample is likely to be small, I can say that the different luminosities show the stars

[4]Throughout this work I have assumed a constant gas-to-dust ratio for all stars in this sample. It is possible that this may change with evolution (e.g. Mauron & Josselin, 2011), altering the $\dot{M}$ - luminosity relation.

[5]Due to the difference in metallicity I have not included the NGC2100 stars in the luminosity distribution.

at slightly different stages of evolution. The concentration of stars in each luminosity bin indicates the relative amount of time the star spends at each interval. When comparing to the Geneva models, it can be seen that RSGs are predicted by Geneva to spend most of their lives at much higher luminosities than observed, between $\log(L/L_{\odot}) \sim$ 4.6 - 5.1, see Fig. 3.3. As $\dot{M}$ is scaled from luminosity in evolutionary models, this will lead to $\dot{M}$ being overestimated by models throughout the RSG phase.

As previously noted I have assumed a uniform age for all of the stars in the sample. However, given the errors on the age estimates for both clusters it is possible that an age spread exists between the RSGs. Currie et al. (2010) estimate the age error on χ Per to be $\pm$ 1Myr, while Marco & Negueruela (2013) estimate the age error on NGC 7419 to be $\pm$ 2Myr. These numbers provide an upper limit to the age spread that exists within the clusters.

I now investigate what effect a 2 Myr age spread would have on the observed luminosity distribution of the RSGs. I used Geneva isochrones and generated luminosity distributions for ages between 12 and 14 Myr (rotating models) at intervals of 0.1 Myr. I assumed a uniform age distribution, simulating a constant star formation rate for 2 Myr. This had no visible effect on the luminosity distribution, with the peak and width remaining the same. I could also have looked at what effect a Gaussian or exponentially declining star formation rate would have on the luminosity distribution, but as the constant rate would have the greatest impact it is unlikely either of these more complicated age spread functions would affect the conclusions. I can therefore rule out a non-instantaneous starburst as being the cause of the difference between the observed and predicted luminosity distributions.

Estimating the total mass lost during the RSG phase

Having determined $\dot{M}$ as a function of evolutionary phase, I now use the results to estimate the total mass lost as a $16M_{\odot}$ star evolves up the RSG branch. This is important as the amount of mass lost can affect the appearance of the resulting SN. For example, while theory predicts RSGs to be the progenitors to Type II-P SN, there is

Figure 3.3: Luminosity distributions for RSGs. Top panel: luminosity distribution for the 13 Galactic RSGs. Centre panel: luminosity distribution for RSGs in Geneva rotating models. Bottom panel: luminosity distribution for RSGs in Geneva non-rotating models.

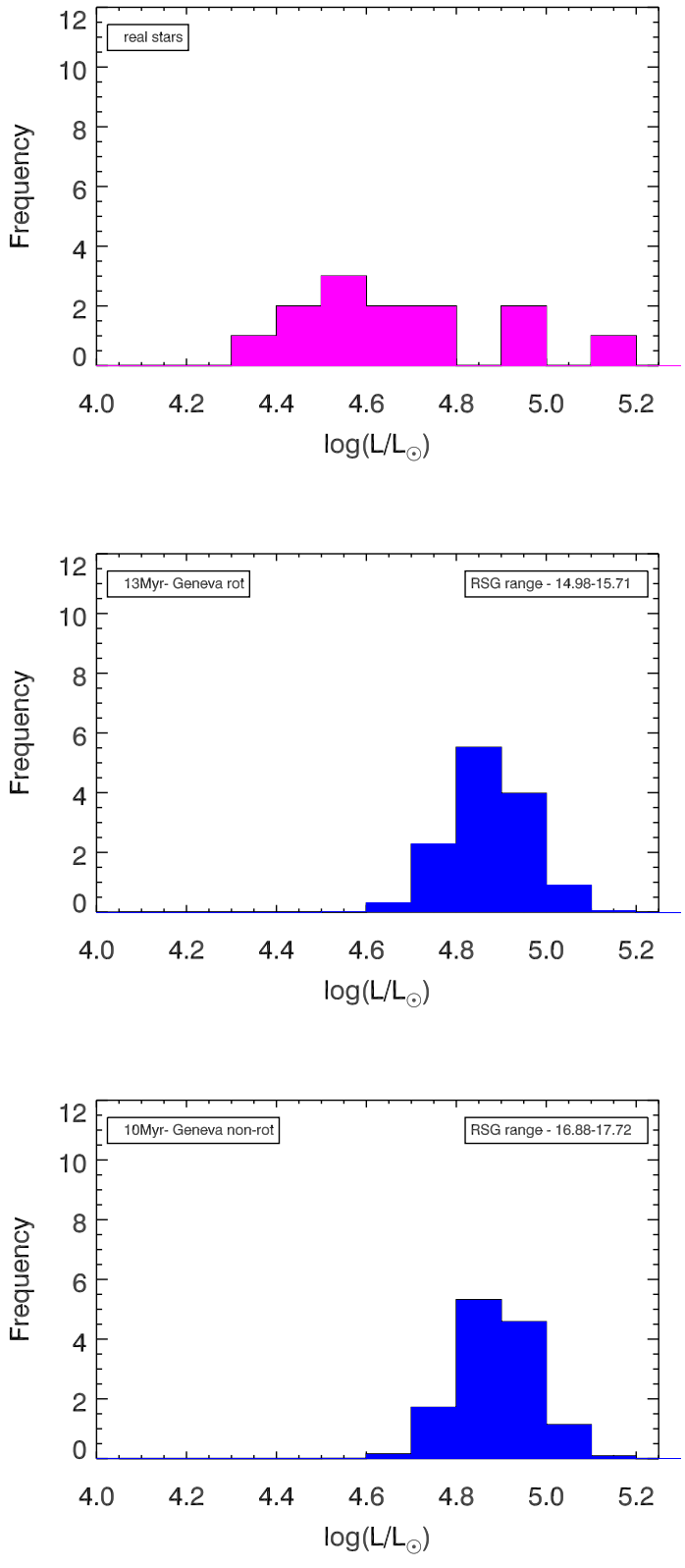

the possibility that if the star were to lose a large enough mass it would appear instead as a Type IIn SN (e.g. Smith et al., 2009, 2016). The narrow lines of a Type IIn SN are visible when a star explodes into a dense circumstellar medium, and for an RSG it would require $\sim$1M$_\odot$ material to be present around the star (Smith et al., 2009). There is increasing observational evidence for a continuum between II-L, IIn and II-P SN as opposed to the SN being produced by distinct progenitors. For example Morozova et al. (2017) found that II-L light curves could be fit by ordinary RSGs with dense CSM. Likewise, SN PTF11iqb showed narrow emission lines for its first two days before they weakened and the light curve quickly began to resemble a II-L and II-P SN (Smith et al., 2015), implying the progenitor experienced enhanced mass-loss in the years preceding the SN.

I now investigate the total mass lost during the RSG phase for a typical 16M$_\odot$ star based on the RSGs in the two MW clusters. For a 16M$_\odot$ star, all major evolutionary codes agree that the lifetime of the RSG phase is 1Myr $\pm$ 15% (Ekström et al., 2012; Eldridge & Stanway, 2009; Dotter, 2016). Using the luminosity distribution for the RSGs in χ Per and NGC 7419, I can deduce how much time an RSG spends at each evolutionary stage. As we know how $\dot{M}$ varies with luminosity, it is possible to determine how $\dot{M}$ varies with time. To convert luminosity into a time, I take the cumulative distribution of $L_{\rm bol}$ and interpolate this onto a time axis of 10^6 years. I then integrate $\dot{M}$ with respect to time and estimate the total amount of mass that would be lost during the RSG phase for a 16M$_\odot$ star.

To estimate the error, I used a Monte-Carlo (MC) method. For each star studied, I randomly sampled its $\dot{M}$ from an asymmetric Gaussian distribution centred on its best-fit value, with upper and lower 1-sigma widths determined by the upper and lower error bars. In each MC trial, I then integrated the $\dot{M}$ of all stars with respect to time to find the total mass lost in that trial. By repeating 10^4 times, it was possible to determine the most likely total mass lost and the upper and lower 68% confidence limits, comparable to a 1-sigma error bar.

From this I find a 16M$_\odot$ star would lose $0.61^{+0.92}_{-0.31}$M$_\odot$ throughout the RSG phase. As this mass is lost over a long period of time (10^6yrs) it is unlikely there would be enough

CSM close to the star to have an effect on the appearance of the resulting SN. Since the amount of envelope mass lost is small I can also expect there to be a long plateau in the SN light curve.

I now compare the measurement of the total mass lost with predictions from stellar evolutionary models. Figure 3.4 shows how much mass is lost during the RSG phase as a function of initial mass for Geneva, STARS and MIST models (Ekström et al., 2012; Eldridge & Stanway, 2009; Dotter, 2016). This figure shows that compared to my observations for a $16M_{\odot}$ star, all evolutionary models employ mass-loss rates that are too high, and hence over-predict the total mass lost during the RSG phase, with Geneva rotating models having the biggest offset from what is observed. In this figure we can also see that at $\sim 20M_{\odot}$ the predicted total mass lost during the RSG phase from Geneva models deviates from the STARS model by around a factor of 3. This could be due to the Geneva group artificially enhancing $\dot{M}$ by a factor of 3 for stars which exceed the Eddington limit in their evelopes by a factor of 5 (Ekström et al., 2012).

Figure 3.4 suggests that evolutionary models are in fact over-predicting mass-loss during the RSG phase, and increasing $\dot{M}$ (as suggested to solve the RSG problem, e.g. Georgy, 2012) would only exacerbate this. Instead, a reappraisal of $\dot{M}$ - prescriptions is needed to better inform stellar evolutionary models and allow more accurate predictions to be made. This is also a wider problem for massive star evolution, including hot star winds and luminous blue variables (LBVs, Smith, 2014). Future work will involve observing stars with different initial masses to fully understand the effect of $\dot{M}$ throughout the RSG phase, and hence determine a new $\dot{M}$ -luminosity relation.

However, I have also shown that the luminosity distributions used in models are skewed to higher luminosities than observed in χ Per and NGC 7419. It may therefore be necessary to find a new way to implement $\dot{M}$ in evolutionary models, since employing an empirical $\dot{M}$-luminosity relation will result in an $\dot{M}$ which is too high if the models are over-predicting the RSG luminosities.

Figure 3.4: Plot showing the amount of mass lost for a star of a given initial mass for various stellar evolution models. The single pink circle shows the total amount of mass lost during the RSG phase for a 16$M_\odot$ star, as derived in Section 3.5.2

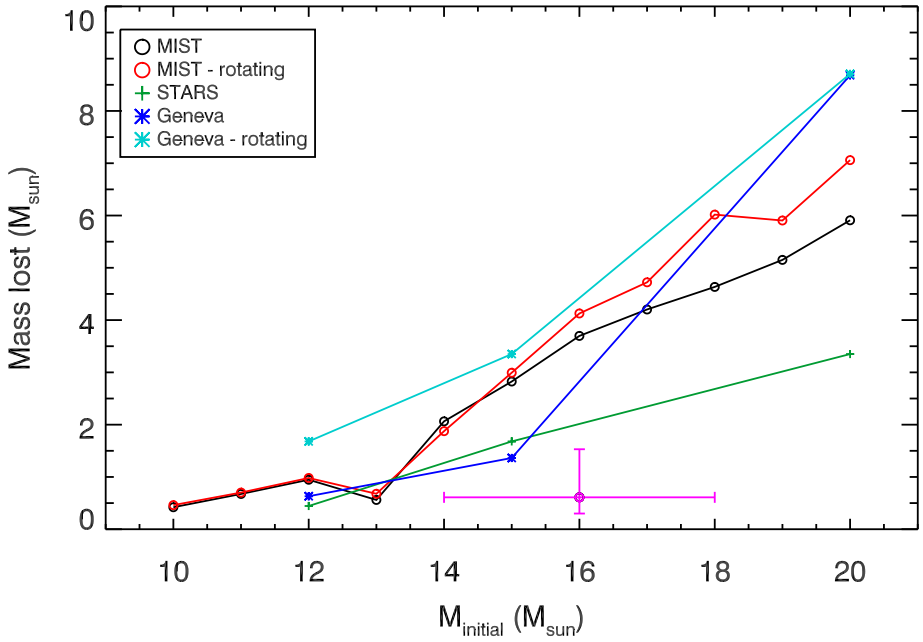

3.6 Conclusions

In this chapter I have re-appraised the $\dot{M}$-luminosity relation using stars in young massive clusters. By focussing on RSGs within clusters we are effectively seeing the same star at different stages of evolution and can therefore observe how $\dot{M}$ varies as the star evolves towards SN. I have determined $\dot{M}$ values and luminosities for RSGs in Galactic clusters NGC 7419 and χ Per, both of which are approximately the same age and hence it is possible to assume the RSGs are all of similar initial mass ($\sim$16$M_\odot$). From this study I can conclude the following:

1. At fixed initial mass $\dot{M}$ increases with time during the RSG evolution of the star, in a relation with little scatter. I suggest that the reason the correlation is tight compared to previous $\dot{M}$ prescriptions is due to keeping $M_{\rm initial}$ constrained. I also find that this relation does not depend on the metallicity of the star, as I have studied both Galactic and LMC clusters and still find a tight correlation. From

this I am able to present a new $\dot{M}$ prescription for stars with initial masses of $\sim$ 16M$_{\odot}$ that depends only on the luminosity of the star.

2. I have also compared the observed luminosity distribution for the RSGs in the two Galactic clusters to evolutionary models. I find that these models overpredict how much time the RSGs spend at high luminosities, and thus overpredict the total amount of mass-loss during the RSG phase.

Chapter 4

Age discrepancies in young clusters; evidence for mergers?

4.1 Introduction

This chapter presents work which has been published by Beasor et al. (2019). The data analysis and interpretation were conducted by E. R. Beasor. The distance estimates presented in Section 4.2.3 were calculated using the method described by B. Davies. The initial draft of the publication was written by E. R. Beasor, who then incorporated comments from co-authors and from an anonymous referee in the final draft.

In the previous chapters, I have derived $\dot{M}$-$L_{\rm bol}$ relations for RSGs of a similar initial mass. A primary aim of this thesis is to create a new $\dot{M}$-prescription applicable to RSGs across the full initial mass range, a process which itself relies on having accurate measurements of initial mass. In this chapter, I describe the potential risks of estimating cluster age from the main sequence turn-off, and propose a new method to determine more accurate RSG initial masses.

Historically, star clusters have been used as a benchmark for stellar evolution models, since it was assumed they were simple stellar populations (SSPs) of a single age and metallicity. However, modern observations of intermediate age and old globular clus-

ters reveal features not easily explained by SSPs, for example the presence of multiple main sequences (e.g. Marino et al., 2008; Piotto et al., 2015), extended main sequence (MS) turnoffs (e.g. Keller et al., 2011; Bastian et al., 2016) and abundance anticorrelations (e.g. Gratton et al., 2004, 2012). Within the literature there are a number of explanations for these peculiar features. Recent work suggests that the extended MS turnoff is an effect of stellar rotation, not age spreads as previously thought (see Bastian & Lardo, 2018, for a recent review). This can be understood as rotational mixing lengthens the MS lifetime by injecting more hydrogen into the core, also causing the terminal age MS stars to appear more luminous.

So far, extended main sequence turn-offs (eMSTOs) are found to exist in intermediate and old age clusters. If the eMSTO phenomenon is caused by stellar rotation, then young ($<$50Myr) clusters should also exhibit this feature, since rotation is thought to have a greater influence the evolution of more massive stars. Indeed, eMSTOs have been observed in clusters as young as 20-30Myrs (Li et al., 2017).

One other potential explanation for stars above the MSTO is rejuvenation, either via mergers or mass transfer (e.g. Schneider et al., 2014; Gosnell et al., 2015). It is now commonly believed that most massive stars exist in binaries ($\geq$ 70%, Sana et al., 2012) and the merger rate of these could be high (de Mink et al., 2014). For stars undergoing binary interaction, mass can be transferred from a secondary on to a primary (mass-gainer) or the two objects can merge entirely. Not only does the merger product gain mass and hence become more luminous, but its MS lifetime is extended by additional hydrogen being mixed into the core. Merger products would therefore appear as younger, brighter stars above the TO, much like blue straggler (BS) stars seen in globular clusters (Sandage, 1984; Knigge et al., 2009; Gosnell et al., 2015). BSs have been tentatively observed in the young cluster NGC 330 (Lennon et al., 1993; Evans et al., 2006) and in Westerlund 1 (Clark et al., 2018), but there has been no systematic study on whether they routinely exist in young clusters. If ubiquitous, the eMSTOs in young clusters would impact their age estimates in the literature.

In Chapters 2 & 3 I have determined the ages to young clusters using two different methods. The first, for NGC 2100, involved fitting the full observed luminosity range

of the red supergiants (RSGs, Beasor & Davies, 2016) with predictions from various stellar evolution models. In Beasor & Davies (2018) I used the previously determined ages for χ Per and NGC 7419, in both cases found by fitting isochrones to MS stars by eye (14 Myr for both, Currie et al., 2010; Marco & Negueruela, 2013). For both of these methods I assumed only single stellar evolution (no binaries, no mergers).

Each age estimation technique has its potential weaknesses. If the merger rate in young clusters is high (as suggested by de Mink et al., 2014), post-merger objects (i.e. an object resulting from the merging of two stars in a binary system) could affect the age determined in each method significantly, as they would appear as bright objects above the TO. Once these stars leave the MS, they could evolve to become RSGs which are anomalously bright compared to the single star population, again causing the observer to infer a younger age for the cluster.

In this chapter I compare ages for 4 young clusters using three different methods and attempt to reconcile these differences in terms of non-simple stellar evolution. In Section 4.3 I describe each of the three age determination methods in detail as well as the method for determining extinction towards the cluster. In Section 4.4 I discuss the results of this work and finally in Section 4.5 I discuss the implications of the results with respect to possible evidence for mergers.

4.2 Observations

4.2.1 Sample

For this work I require clusters for which it is possible to obtain age estimations from the MS turnoff *and* the RSGs. The clusters must therefore be spatially resolvable, and be young enough and massive enough to have a well-populated RSG branch. Based on this, I have chosen 2 young clusters from within the Galaxy (NGC 7419, χ Per) and 2 located in the LMC (NGC 2100, NGC 2004).

4.2.2 Photometry

The majority of the data used in this work is archival. I will now briefly describe the MS and RSG data for each cluster. The MS data for NGC 7419 is UBV photometry from Beauchamp et al. (1994). The RSG photometry includes $UBVRI$ from Joshi et al. (2008), and near and mid-infrared (IR) photometry from 2MASS (Skrutskie et al., 2006) and MSX (Price et al., 2001).

The main sequence photometry for χ Per is from Currie et al. (2010). As this catalogue contained data for both clusters in the h + χ Per complex, I simply included any star that was within 6 arcmin of the cluster centre, the distance to the edge of the complex. For the RSGs, I used archival photometry from Johnson et al. (1966); Kharchenko et al. (2009); Pickles & Depagne (2010) and MSX (Price et al., 2001). As described in Davies & Beasor (2018), there was an offset in the I-band between the Johnson and Pickles photometry which could not be explained. I have again taken an average of both the measurements and defined the error to be half the difference between the two.

For NGC 2004 and NGC 2100, I use the dereddened photometry from Niederhofer et al. (2015) for the MS stars, originally from Brocato et al. (2001). This photometry has been dereddened to mitigate the effect of differential extinction using the method described in Milone et al. (2012). The RSG photometry is compiled from Spitzer, MSX and WISE (Werner et al., 2004; Price et al., 2001; Wright et al., 2010).

4.2.3 Distances

To determine the distances to the two Galactic clusters, all hot star cluster member are isolated by searching the SIMBAD database for OB stars in the plane of each cluster. Next, Gaia DR2 parallaxes and proper motions for all stars are obtained. Following Aghakhanloo et al. (2019) the error on the parallax σ_i of each star i is defined to be $\sigma_i = \sqrt{(1.086\sigma_\pi)}$ where σ_π is the quoted error on π in $Gaia$ DR2. We then iteratively sigma-clip the sample by discarding those stars with proper motions outside 3σ of the mean for the whole cluster. Of the N remaining stars (140 for χ Per, 20

Table 4.1: Distances and extinctions for the clusters. The distances to the LMC clusters are taken from Pietrzyński et al. (2013).

Cluster	Distance (kpc)	Extinction (A_V)
NGC 7419	$2.93^{+0.32}_{-0.26}$	6.33 ± 0.22
χ Per	$2.25^{+0.18}_{-0.14}$	1.22 ± 0.22
NGC 2100	50±0.1	Differential, taken from Niederhofer et al. (2015)
NGC 2004	50±0.1	Differential, taken from Niederhofer et al. (2015)

for NGC 7419), we determine the sigma-weighted mean of the parallaxes $\bar{\pi}$ and the standard deviation $\sigma_{\bar{\pi}}$, and define the formal error on $\bar{\pi}$ to be $d\bar{\pi} = \sigma_{\bar{\pi}}/\sqrt{(N)}$.

The posterior probability distribution function P_r on the distance r to the cluster is determined from $P_r \propto \exp(-0.5z^2)$, where $z = (\bar{\pi} - \pi_{\rm ZP} - 1/r)/d\bar{\pi}$, and $\pi_{\rm ZP}$ is the zero-point parallax offset in Gaia DR2[1]. Various independent measurements of $\pi_{\rm ZP}$ have been made, with a global average seeming to converge on $\pi_{\rm ZP} = -0.05$mas (see Aghakhanloo et al., 2019, for a discussion). However, Lindegren et al. (2018) find that this value varies across the sky by ± 0.03mas on spatial scales of about a degree (i.e. larger than the cluster field of view). We therefore adopt a value of $\pi_{\rm ZP} = -0.05 \pm 0.03$mas, where this error on the zero-point offset must be added in quadrature to that of $\bar{\pi}$.

For χ Per and NGC 7419, we find average parallaxes of 0.448 ± 0.003mas and 0.333 ± 0.009mas respectively, not including the uncertainty on $\pi_{\rm ZP}$. These values are converted to distances and uncertainties by finding the mode and 68% confidence intervals of $P_r d$, finding $2.25^{+0.18}_{-0.14}$kpc and $2.93^{+0.32}_{-0.26}$ kpc for χ Per and NGC 7419 respectively. This analysis was done by B. Davies and for further discussion on the distances see the forthcoming paper by Davies & Beasor (accepted).

As NGC 2100 and NGC 2004 are both LMC clusters I take the distance of 50±0.1 kpc (Pietrzyński et al., 2013).

[1]Unlike several other studies of Gaia DR2 distances, we do not adopt any Bayesian prior.

4.3 Age estimations

I now describe how the extinction values are derived for each cluster, and detail each of the three independent age determination methods. As I am using the de-reddened photometry for NGC 2004 and NGC 2100 I assume the extinction on this data should be negligible (data taken from Niederhofer et al., 2015) .

4.3.1 Estimating the foreground extinction

To estimate foreground extinction I began by constructing a colour-magnitude diagram (CMD) for each cluster. To isolate the MS I make cuts in colour-magnitude space. For the magnitude cut, I cut any bright stars that sit more than 2 magnitudes from the main sequence. For the faint end of the MS, I cut any stars obviously fainter than the point at which the sample is no longer complete (i.e. the brightness at which the number of stars per magnitude bin starts to decrease). For the colour cut, I discount anything that is clearly too red to be a member of the MS.

To determine the best fitting extinction I employ population synthesis analysis, using a grid of MIST isochrones from ages 2Myrs to 100Myrs (Paxton et al., 2010, 2013, 2015; Dotter, 2016) at the approximate metallicity (+0.0 dex for Galactic clusters, -0.5 dex for LMC clusters). I begin by generating a population of 10000 stars between masses of 1.5 and 100$M_{\odot}$ sampled from the Salpeter initial mass function (IMF). I then interpolate the random stars onto the MIST mass-brightness function for whichever filters are appropriate for the photometry of the cluster being analysed. I adjust the synthetic photometry for the distance estimated in Sect 2.3 and a dummy input extinction value, according to the extinction law of Cardelli et al. (1988). I make the same cuts in magnitude and colour as I have done for the observed data.

Next, I take both the synthetic MS and the observed MS and bin the stars into 2D histograms in colour-magnitude space. I then normalise the model distribution such that the model and observed CMDs have the same number of stars above the magnitude cut. I then compute the χ^2 statistic between the observed and model histograms. This is

Figure 4.1: Hess diagram for NGC 7419. The black points indicate stars that were included in the analysis. The red dashed line shows the fainter magnitude cut.

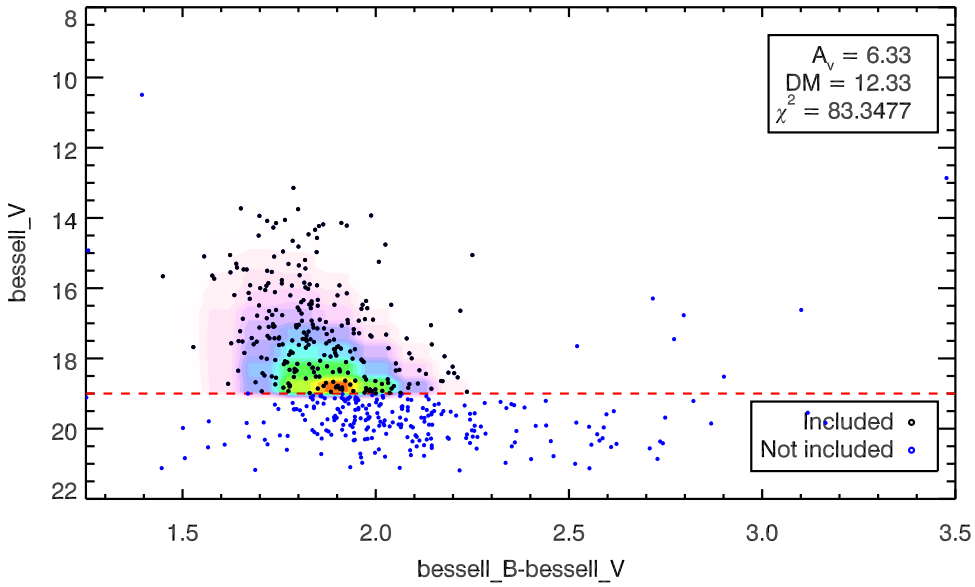

repeated for a grid of input extinctions and ages, with the best fit extinction determined from interpolating where the χ^2 goes to zero. Figure 4.1 shows a Hess diagram for NGC 7419. Extinction estimates are shown in Table 4.1.

Note that, in principle, I can obtain an age estimate from this analysis. However, since the cluster age and extinction are virtually orthogonal to each other in terms of how they displace the MS on the CMD, I chose to simplify the analysis and first fit for extinction then do a single-parameter fit for the age.

4.3.2 Brightest turn-off star method

The TO of a star cluster is defined as the most massive star that has yet to deplete H from its core. Since stellar mass and MS lifetime are strongly correlated, this can give an indication as to the cluster age. Once the Ms has been identified via the method described in Section 4.3.1 I then assume the brightest single star in this subsample is the TO point for the cluster. Next, I use a grid of MIST isochrones (ages ranging from 2Myrs to 100Myrs, repeated for both rotating and non-rotating models), corrected for

distance and extinction using the values found in the previous section, and identify the magnitude of the TO at each age (I assume the end of the MS is the point at which the central hydrogen mass fraction is less than 1x10^{-4}). From this I identify the theoretical TO magnitude-age relation. I then take the magnitude of the brightest TO star in the cluster and interpolate this onto the magnitude-age relation and hence derive an age for the cluster. Errors come from the photometric error on the magnitude. Results are shown in Table 4.2.

One obvious weakness of this method is the susceptibility to stochastic effects from sparsely sampling the IMF at the high mass end. I look to improve upon this in Section 4.3.3. In addition, the presence of an eMSTO or bright BS-like stars above the TO would cause a younger age to be inferred.

4.3.3 Luminosity function

A similar but slightly more sophisticated method to determine the age from the turn-off is to model the luminosity function (LF) of the brightest stars in the main sequence. I use population synthesis (as described in Section 4.3.1) and adjust the colour and magnitude of the synthetic stars to the distance of the cluster and redden the photometry using the extinction derived in Section 4.3.1. For each age, histograms are then created for both the real and the synthetic stars of the number of stars per magnitude bin. These distributions are then compared and the best fit age is found using χ^2 minimization (see below). Results are shown in Table 4.2 and an example best fit is shown for NGC 7419 in the top panel of Fig. 4.2.

The best fitting age and 1-sigma error range is determined following Avni (1976). Our fitting function, derived from our population synthesis, has two degrees of freedom: age t (which moves the LF left and right), and mass M (which affects the normalization). I find the optimal age by minimizing the function,

$$\chi^2 = \sum_i \frac{[O_i - E_i(t, M)]^2}{\sigma_i} \tag{4.1}$$

where O_i and E_i are the numbers of stars in the ith bin of the observed and model LFs respectively. The 68% confidence intervals on t are determined from those models with χ^2 within 2.3 of the minimum, see bottom panel of Fig. 4.2.

The advantage of qualitatively fitting the LF at the TO, rather than simply taking the magnitude of the brightest turn-off star, is that it attempts to compensate for stochastic sampling of the TO. However it will still be affected by the presence of BSSs and stellar rotation.

4.3.4 Lowest luminosity red supergiant

An independent method to determine the cluster age is to model the RSG population. Specifically, I use the bolometric luminosity ($L_{\rm bol}$) of the least luminous RSG in each cluster ($L_{\rm min}$). When a star crosses the HRD it does so at a nearly constant luminosity, and upon joining the RSG branch there is an initial decrease in $L_{\rm bol}$. Once the star has settled on the RSG branch it returns to a luminosity similar to that when it left the MS. For an isolated RSG, it is hard to know the evolutionary history, i.e. how evolved it is and whether or not it descended from a single star or from a BS type object. However, in a large cluster of stars all born at the same time, the RSG with the lowest $L_{\rm bol}$ is most likely that which has evolved as a single star and most recently joined the RSG branch.

To calculate $L_{\rm bol}$ I take all of the available photometry for a given star and integrate under the SED from blue to the mid-IR, as described in Davies et al. (2018). This method relies on the assumption that the flux emitted is spherically symmetric and as RSGs are known to have circumstellar extinction I also assume any flux lost at shorter ($<$U - band) wavelengths is reemitted at longer wavelengths. To account for any flux at shorter wavelengths I have extrapolated the SED using a blackbody temperature of 3500K, though in practice this region of the SED accounts for less than 0.01dex of the bolometric luminosity.

Due to the steepness of the IMF the number of RSGs in a given cluster is usually

Figure 4.2: *Top panel:* Best fitting luminosity function for NGC 7419. The black line shows the observed TO LF while the blue line shows the model. *Bottom panel:* Plot showing the error estimation for the LF method. The solid green line shows the best fitting age and the dashed green lines show the χ^2 acceptability limit, i.e. $\chi^2_{\rm min}$+2.3.

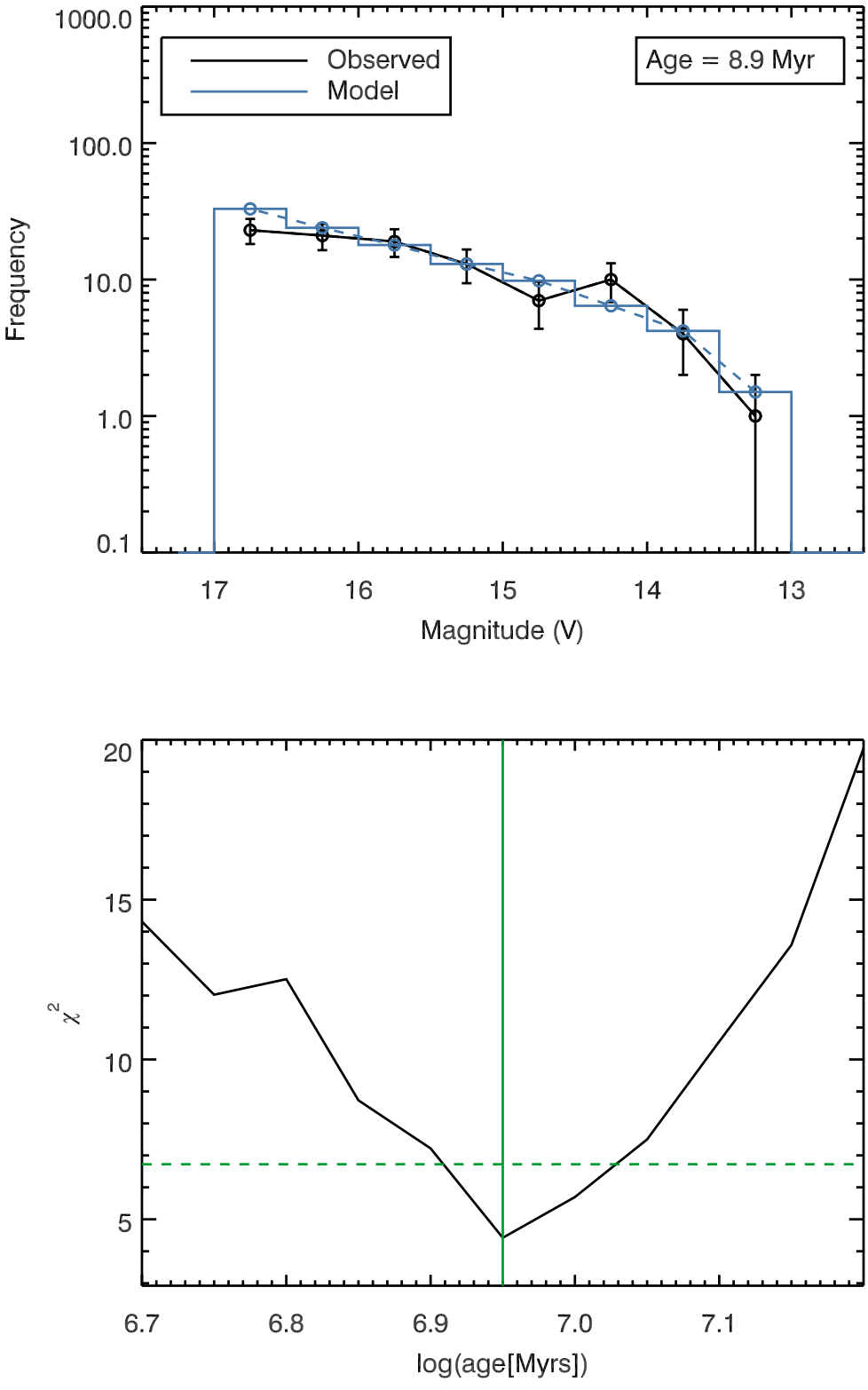

small, on the order of $\sim$10, leaving this method susceptible to the stochastic effects. Furthermore, the evolution through the early part of the RSG branch is very fast. In light of this, I correlate $L_{\rm min}$ with cluster age in a probabilistic sense using population synthesis.

I again utilise the MIST grid of isochrones. At each age, I identify the RSG phase as being where $T_{\rm eff} \leq$ 4500K and $\log(L/L_{\odot}) \geq 4$. Next, I identify the minimum and maximum stellar mass from the defined RSG phase and generate a sample of 500 synthetic stars following a Salpeter IMF, and then take a random subsample of these stars to match the number of real RSGs in a given cluster, e.g. for NGC 2100 there are 19 RSGs. At each trial, I determine the value of $L_{\rm min}$ and repeat 1000 times to get a probability density function. Figure 4.3 shows the most likely $L_{\rm min}$ values for a cluster containing 50 RSGs at each age in our grid. This process is repeated at each age, yielding a 2-D probability density function of age and $L_{\rm min}$. From this I interpolate the observed $L_{\rm min}$ for a cluster, which itself is randomly sampled 1000 times from a Gaussian distribution to take into account the errors, and derive an age distribution for the cluster. Results are shown in Table 4.2. As the errors on $L_{\rm bol}$ are small the error on age is taken from the nearest grid point.

4.4 Results

The age estimates for each cluster are listed in Table 2. Figure 4.4 shows the best fitting isochrones determined for each cluster via each of the methods described above. Note that often the RSGs were saturated in these filters and hence could not be shown. Due to the uncertainty in the colours of late-time stars the isochrones often do not sit where RSGs are observed. In these plots the red line shows the results from the lowest luminosity RSG method, the green line shows the result from fitting the luminosity function of the TO and the blue line shows the results from fitting the single brightest star at the MSTO. The solid portion of the line shows the MS. Each isochrone has been reddened using the extinctions determined in Section 4.3.1.1 and the extinction coefficients from Cardelli et al. (1988) (optical) and Koornneef (1983) (mid-IR).

Figure 4.3: Plot showing the most likely RSG $L_{\min}$ for a cluster at a given age containing 50 RSGs, from MIST non-rotating isochrones (Dotter, 2016). Each point represents the median $L_{\min}$ of 1000 trials while the error bars represent the 68% probability limits. For clusters with fewer RSGs the relation stays the same but there are more stochastic errors.

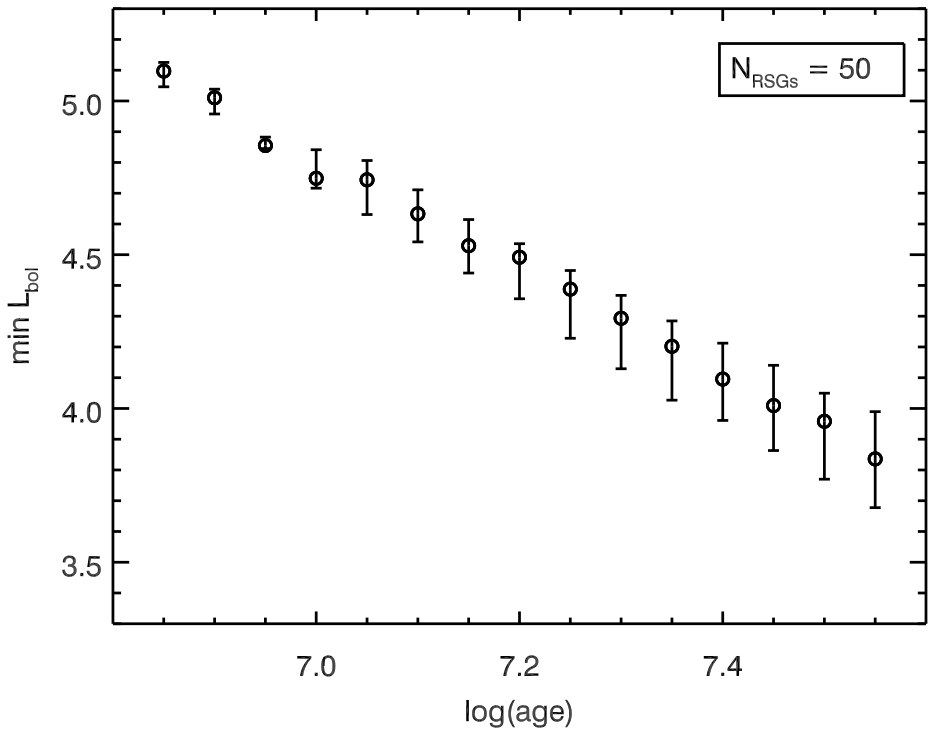

Figure 4.4: Plot showing best fitting isochrones from each of the three age estimators for the Galactic clusters. The solid portion of the isochrones represents the main sequence. The purple star symbol indicates the brightest TO star used for the age determination.

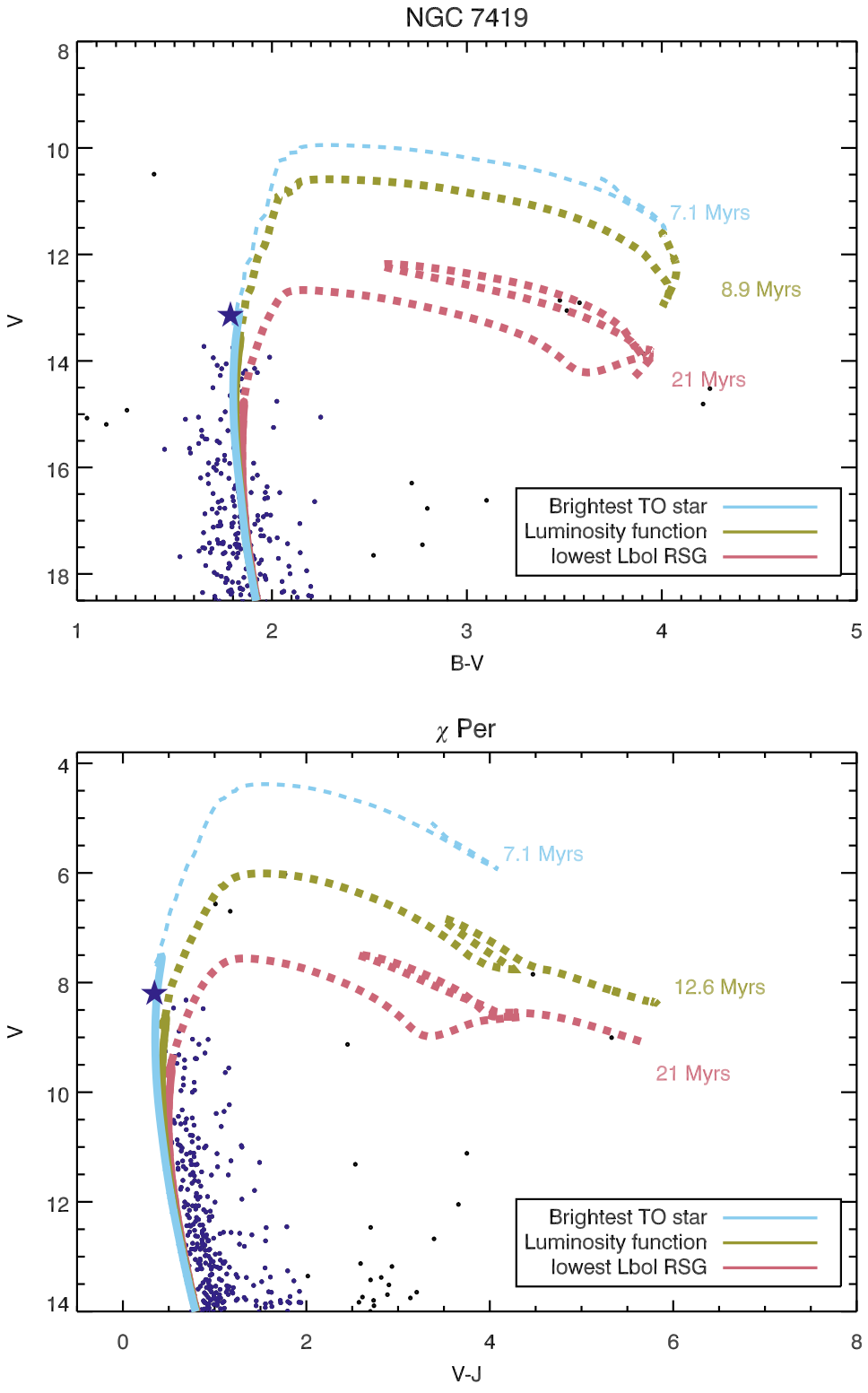

Figure 4.5: Same as Fig. 4.4 but for the two LMC clusters.

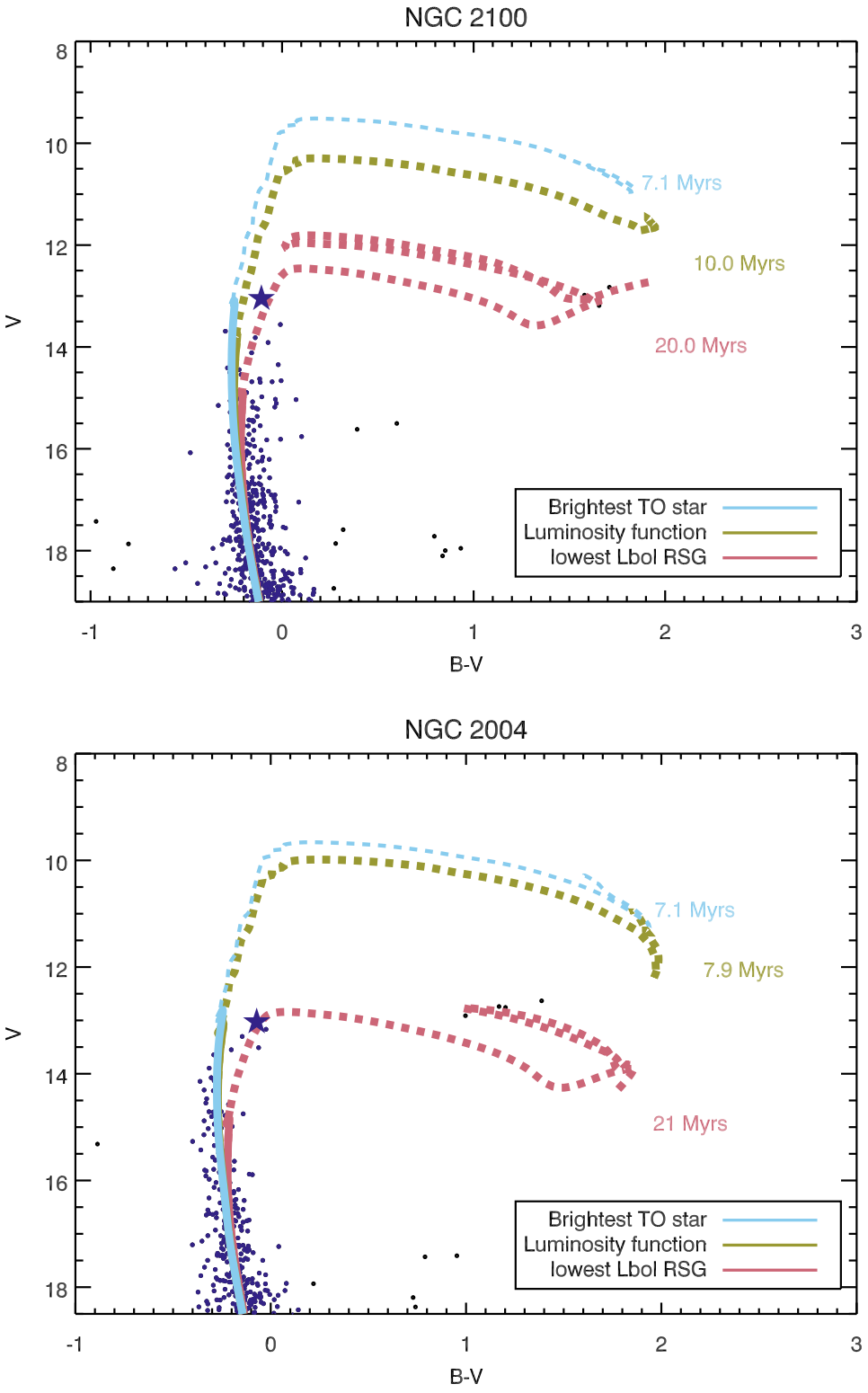

Table 4.2: Age estimations for each cluster found using the three different age determination methods. For the brightest TO method and the lowest $L_{\rm bol}$ RSG method, the errors on photometry were small and hence the errors presented here represent the grid spacing of of the ages.

Cluster	Age estimates (Myr)								
	Brightest TO star			Luminosity function		Lowest $L_{\rm bol}$ RSG			
	Magnitude	Rotating	Non-rotating	Rotating	Non-rotating	$N_{\rm RSGs}$	$L_{\rm bol}$	Rotating	Non-rotating
NGC 7419	13.14 (V)	8.3 ± 1	7.1 ± 1	9^{+1}_{-1}	9^{+2}_{-1}	5	4.37	21 ± 1	20 ± 1
χ Per	8.19 (V)	8.1 ± 1	7.9 ± 1	13^{+2}_{-2}	13^{+2}_{-2}	8	4.38	22 ± 1	21 ± 1
NGC 2100	13.05 (V)	7.1 ± 1	7.1 ± 1	10^{+1}_{-1}	10^{+1}_{-1}	19	4.43	22 ± 1	20 ± 1
NGC 2004	13.02 (V)	7.1 ± 1	6.3 ± 1	$8^{+1}_{-0.5}$	$8^{+1}_{-0.5}$	7	4.35	24 ± 1	22 ± 1

For all of the clusters, the difference between the ages determined using the brightest TO star and the luminosity function of the cluster TO is minimal and smaller than the difference between rotating and non-rotating models, at most the difference in best fit age varies by 0.5Myr, but they are all consistent to within the errors. The lowest luminosity RSG method always finds the cluster to be older than the cluster TO methods. The most extreme example of this is NGC 2004, for which the RSG method finds an age that is three times older. In the following sections I will discuss the results for each cluster in turn and compare to previous age estimates.

4.4.1 NGC 7419

This cluster has previously been studied by Marco & Negueruela (2013), who fit isochrones from Marigo et al. (2008) by eye to UBV data of the entire cluster, finding an age of 14Myr. The authors found that a 12Myr isochrone was a good fit to the TO once B stars were removed, but an older age of 15Myr also fit the apparent TO well while leaving some brighter stars above. Beasor & Davies (2018) found the previously best fitting age isochrone (14 Myr, Padova) found by (Marco & Negueruela, 2013) was equivalent to an age of 10-14 Myr if the Geneva isochrones were used to fit the same MSTO point.

In this study, the age estimates for NGC 7419 vary between methods by approximately 10 Myr for both rotating and non-rotating models. As with all the clusters, the brightest TO and the luminosity function of the TO methods (7-8 Myr) suggest the cluster is far younger than the age determined using the lowest $L_{\rm bol}$ RSG ($\sim$17 Myr). There is very little difference between the ages found for the cluster using the brightest TO star and the luminosity function of the TO. The previous age estimates for this cluster are approximately an average of the TO and RSG ages I present here, as previous studies have fit the TO and RSG branch diagnostics simultaneously.

4.4.2 χ Persei

This cluster is part of the h and χ Per Double Cluster, and has been studied before in detail by Currie et al. (2010). Using UBVI data, the age of the cluster was estimated by these authors a number of ways. Using the MS they find an age of 14 Myrs, and claim the M supergiants support this age. Using Padova isochrones they fit by eye to see which best fits the RSG range, however they use the full luminosity range to make a prediction, and as previously discussed due to evolution and the possibility of post-merger objects there is no unique relation for age and the brightest RSGs. In Beasor & Davies (2018) the best fitting Padova isochrone was again used to find a model dependent age for the cluster, finding again a Geneva age estimate of 10-14 Myr (for rotating and non-rotating models).

In this work I find ages ranging from 8 Myr to 18 Myr (with the TO method giving the youngest age estimate and the RSG method giving the oldest). Again the previously presented age estimates are somewhere in the middle of this. While Currie et al. (2010) did not fit the entire cluster (TO and M-supergiants) simultaneously I find the age given by the luminosity function method gives an age consistent with theirs. The cause for discrepancy when using the RSGs between Currie et al. and our work could be simply due to the previous authors using the entire luminosity range of the RSGs to estimate an age, rather than the lowest $L_{\rm bol}$RSG.

4.4.3 NGC 2100

There are a number of age estimations for LMC cluster NGC 2100 in the literature. Niederhofer et al. (2015) fit both the TO and the RSG branch simultaneously, giving an age of 21 Myr, in agreement with the age found from the lowest $L_{\rm bol}$ RSG method. It can again be seen that at this age the model Hess diagram cannot explain the brightest blue stars above the MSTO, and the authors claim this is an effect likely caused by stellar rotation (see Section 4.5. The age has been estimated since then by Beasor & Davies (2016) who used the full range of RSG luminosities and evolutionary mass

tracks (see Fig. 8 within the paper). This gave a younger age of $\sim$15 Myr.

In this work I find an age discrepancy of a factor of 2 between the brightest TO star method and the RSG method. I find using the MSTO gives an age of 7-10 Myr (for the single brightest TO star and LF respectively). For the lowest $L_{\rm bol}$ RSG method I find an age of 20-22Myr, older than found by Beasor & Davies (2016) by 5 Myr.

4.4.4 NGC 2004

This LMC cluster was studied in Niederhofer et al. (2015), in which the authors estimated the cluster age to be 20 Myr, but again the observed MS reached brighter magnitudes than predicted by the model. This age is also consistent with the age derived from the lowest $L_{\rm bol}$ RSG method, likely because the authors disfavour using the brightest stars in the TO as they believe them to be either BSSs or evidence for an extended main sequence TO (see Section 5.1). This cluster has the largest discrepancy in age estimations out of all the clusters in this sample, with the RSG method suggesting an age that is up to 4 times older than the TO method results.

4.5 Discussion

The analysis has shown that age estimates vary by up to a factor of 4 depending on which method is employed, see Fig. 4.4. The most dramatic difference is seen for NGC 2004, where the brightest TO star gives an age of 6 and 7 Myr for non-rotating and rotating models respectively, while the RSG method gives an age of 22 Myr or 24 Myr for non-rotating and rotating models respectively. I will now discuss possible causes for these age discrepancies in detail.

4.5.1 Possible causes for age discrepancies

Stellar rotation causes extra hydrogen to be mixed into the core of the star, prolonging the life of a star. Stars that rotate more rapidly spend longer on the MS than stars that rotate more slowly, making it difficult to explain all of the stars at the TO with a single age isochrone.

For young and intermediate age clusters (20Myr - $\sim$2Gyr, Bastian & de Mink, 2009), rotation has been used to explain the extended main sequence turn off (eMSTO) phenomenon, where the TO of a cluster appears brighter than expected in a colour magnitude diagram (e.g. Keller et al., 2011). In Niederhofer et al. (2015), rotating and non-rotating isochrones were used to determine what perceived age spread would be seen in a cluster due to stellar rotation. This study showed that as clusters increase in age, the apparent age spread due to the eMSTO increases (i.e. clusters with ages $<$100 Myr have small age spreads, on the order of tens of Myr, while clusters $\sim$ 1 Gyr have apparent age spreads on the order of a few hundred Myr). This age spread is proportional to the age of the isochrone. While this study implies the eMSTO effect is likely to be present in the clusters presented in this work, isochrones used in Niederhofer et al. (2015) were between 50 Myr - 1 Gyr, older than the 4 clusters presented in this study. Therefore the significance of the eMSTO at ages $<$ 50 Myr is not yet quantified.

To check whether rotation could have a significant effect on the ages determined for the clusters in this sample, I first used MIST rotating and non-rotating models for all ages; Table 4.1 shows the results for all methods. The rotating MIST models include stars with rotation at 0.4 of the critical velocity. We can see from the results that the difference in ages between rotating and non-rotating models is minimal ($\pm$10%). Therefore, stars rotating at this speed are not able to explain the differences in ages I obtain between the methods utilising the MSTO of the cluster and the method using the red stars. Therefore, to extend the MS by long enough to explain the age differences, stars would have to be rotating at speeds faster than 0.4 of the critical velocity.

To further investigate the impact of stellar rotation on inferred ages, I have re-analysed the data for NGC 2100 with the isochrones of Georgy et al. (2013), which have a much

sparser sampling in stellar mass but which explore a much greater range of initial rotation rates. Figure 4.6 shows the colour magnitude diagram for NGC 2100 with 3 isochrones overplotted. The first is the 10 Myr MESA isochrone, which I found to be the best fitting age when using the LF method, shown by the red line. The second is the 20Myr non-rotating isochrone from Georgy et al., the best fitting age found when using the lowest $L_{\rm bol}$ RSG, shown by the blue line. Finally, I also show the 10 Myr iscochrone where the stars are rotating at 0.95 of the critical velocity, shown by the yellow line. I have highlighted the tip of the TO according to each model with a circle.

Figure 4.6 shows the TO of the best fitting isochrone found from the LF method is 1.3 mag brighter than the TO of the best fitting isochrone from the RSG method, when there is no rotation. When stellar rotation is present, even with stars rotating at 0.95 of critical the difference in magnitude between the 10 Myr TO and the 20 Myr TO is 0.8 mag. These results argue that even extreme rotation rates cannot explain the age discrepancies found. Further to this, Marco & Negueruela (2013) counted the number of Be stars, objects showing Hα emission commonly thought to be fast rotators, within the MS of NGC 7419 and find the number of Be stars at the TO is approximately equal to the number of 'normal' objects (see Fig. 8 within their paper). Therefore, while stellar rotation is likely to have some effect on broadening the MSTO, it cannot fully account for the discrepancies I have observed. I speculate that stars above the TO of the fast rotating isochrone may be BS-like stars formed via binary interaction, i.e. merger products or mass gainers.

I now compare these results to the predictions of Schneider et al. (2015), who computed the evolution of single and close interacting binary stars. They predict the ratio of the number of blue stragglers expected in a cluster ($N_{\rm bss}$), to the number of stars 2 magnitudes below the TO (N_2) as a function of cluster age (see Fig. 14 within that paper). When taking the same diagnostics for NGC 2100 (using the TO from the Geneva rotating models as shown by the yellow dot in Fig. 4.6) I find an $N_{\rm bss}/N_2$ ratio of 0.11, in close agreement with the predictions of Schneider et al., who predict a ratio of 0.1-0.2 for a 20Myr cluster. All of the potential BS-star candidates[2] in NGC 2100

[2]The exact number of BS candidates changes slightly depending on which isochrones are used. Here

Figure 4.6: Plot showing the CMD for the stars in NGC 2100. Overplotted are isochrones from (Georgy et al., 2013) (the rotating and non-rotating 20 Myr, age from RSG method) and MIST (10 Myr, age from the luminosity function method). Filled coloured circles represent the MSTO for each isochrone.

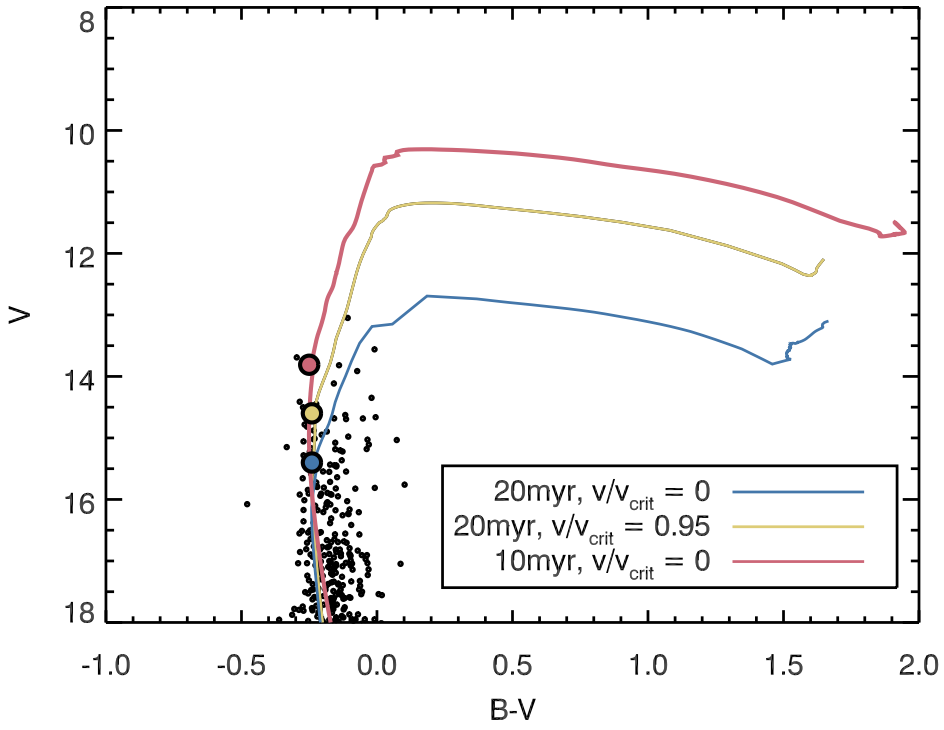

were found to be cluster members by Niederhofer et al. (2015). Further to this, Figure 16 in Schneider et al. (2015) shows the apparent stellar age, τ_*, of the most massive blue straggler star as a function of the true cluster age, $\tau_{\rm cl}$. For a 20Myr cluster, the most massive BSS would cause an inferred age of approximately 5-10Myr, again in good agreement with the findings presented here. It should be noted however that the predictions of Schneider et al. are based on theoretical clusters with a primordial binary fraction of 100%, so the age discrepancies and number of BSSs they present are upper limits. However, it is encouraging to see that these model predictions are comparable to the observations.

I have chosen to use the Geneva isochrones rotating at 0.95 of the critical velocity to set a lower limit on the number of BS candidates.

4.5.2 How should we determine ages for young clusters?

Initial masses for post-MS transitional objects such as luminous blue variables (LBVs), Wolf-Rayet stars and RSGs are often estimated by locating such objects in clusters, then determining the cluster age using the cluster TO and single rotation isochrones (e.g. Humphreys et al., 1985; Massey et al., 2000, 2001). Throughout this work I have shown that using the TO is likely to cause the age inferred to be too young, and hence the initial masses too high. I attribute this effect to BS-like stars above the TO, some of which may be explained by a distribution of rotation rates at ZAMS. To attempt to quantify this effect, and to determine which age estimation method provides the most accurate results, I repeat the analysis on synthetic clusters of a known age with a realistic rotation distribution, described below.

I now enlist synthetic clusters from Geneva (Ekström et al., 2012) to investigate the impact of using the cluster TO more thoroughly. I generated a 20 Myr old cluster at Solar metallicity (Z=0.014), where the stellar rotations follow the distribution of Huang et al. (2010). Next, the mass of the cluster is randomised between 0.5-5$\times10^4$M$_\odot$, typical of clusters known to contain RSGs. From this subsample, it is possible to identify the brightest TO star and the least luminous RSG (where the RSG phase is defined as where $T_{\rm eff} \leq 4500$K). To ensure I am comparing like-with-like, I use Geneva non-rotating isochrones to determine age estimations via the methods described in Section 4.3.3 and 4.3.4. The grid of Geneva models has ages from 6 to 25 Myrs. I repeat this for 1000 trials, where each trial generates a new cluster with varying cluster mass, thus allowing us to see how the age discrepancy between each method varies with total cluster mass (M$_{\rm tot}$).

Figure 4.7 shows the distribution of age estimations for each method as a function of cluster mass. The dashed line shows the true cluster age and the results of each trial are plotted with blue crosses (TO method) or red crosses (RSG method). For the RSG method in particular, the errors on age are larger at lower cluster masses. This is due to lower mass clusters perhaps only containing $\sim$1 RSG, leading to large stochastic errors.

The results found here demonstrate clearly that using the cluster TO method can cause a systematic underestimation in age by $\sim$25% due to rotation on the MS extending the lifetime of MS stars and causing them to appear more luminous. While there is also a systematic offset when using the lowest $L_{\rm bol}$ RSG method, this is a much smaller effect, on the order of $\sim$10%. This offset is due to numerical effects when interpolating mass tracks containing blue loops, causing the bottom of the RSG branch to appear more luminous. For a typical cluster where $M_{\rm tot} < 5\times10^4 M_\odot$ the random error is approximately 5-10%, comparable to the systematic offset.

I now repeat this experiment and include unresolved binaries with a binary fraction of 50%[3]. Figure 4.8 shows the determined ages for a cluster as a function of cluster mass with a binary fraction of 50%, as shown by the blue crosses. This illustrates that the inclusion of unresolved binaries further reduces the usefulness of the TO method, causing an even greater discrepancy ($\sim$ 6Myr), while the RSG method remains much less affected (note that the red crosses on the plot show the results for the RSG method from both the cluster containing only single stars, and the cluster with a binary fraction of 50%). This is because the RSGs are significantly more luminous than the companion stars and hence are unaffected by unresolved binaries. From this analysis I can conclude that using the lowest $L_{\rm bol}$ RSG method is the most reliable. Interestingly, the age discrepancies found by this experiment are far lower than the discrepancies observed in the real clusters. This supports the conclusions that the age discrepancies observed for the 4 real clusters cannot be caused by rotation on the MS alone, and are likely caused by a combination of rotation, unresolved binaries and binary products (such as mass gainers or mergers).

4.6 Conclusions

In this chapter I present age estimates for 2 Galactic clusters and 2 LMC clusters using 3 different methods. By doing this I have demonstrated a systematic offset between

[3]As the isochrones used to create each cluster rely on single star tracks it is not possible to account for the evolution of interacting binary systems (Georgy et al., 2014)

Figure 4.7: Ages derived from age fitting a 20Myr synthetic cluster containing only single stars using the TO method and the lowest $L_{\rm bol}$ RSG method. The dashed line shows the true age of the cluster.

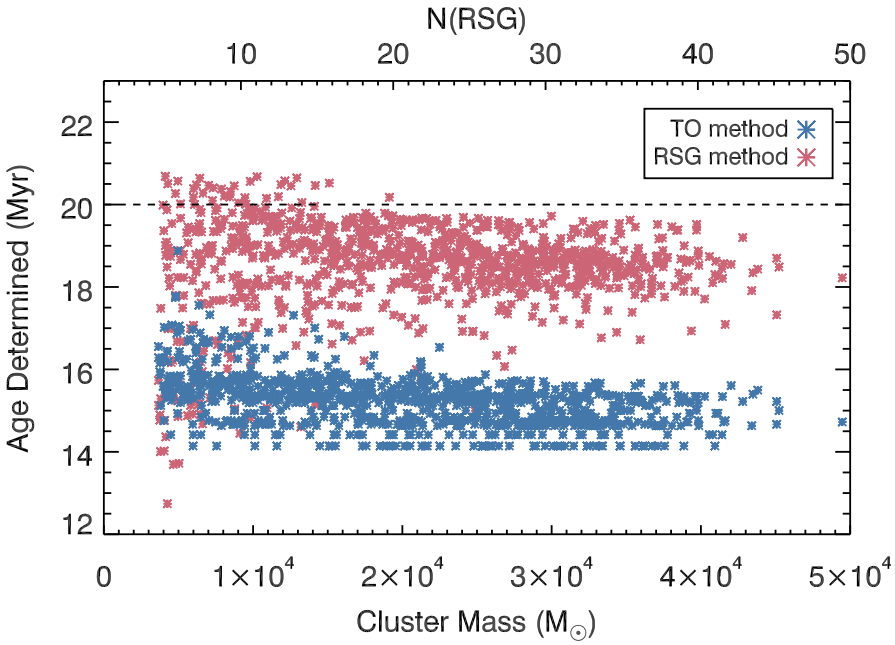

Figure 4.8: Ages derived from age fitting a 20Myr synthetic cluster using the TO method and the lowest $L_{\rm bol}$ RSG method. In this case, the synthetic cluster has a binary fraction of 50%. The dashed line shows the true age of the cluster.

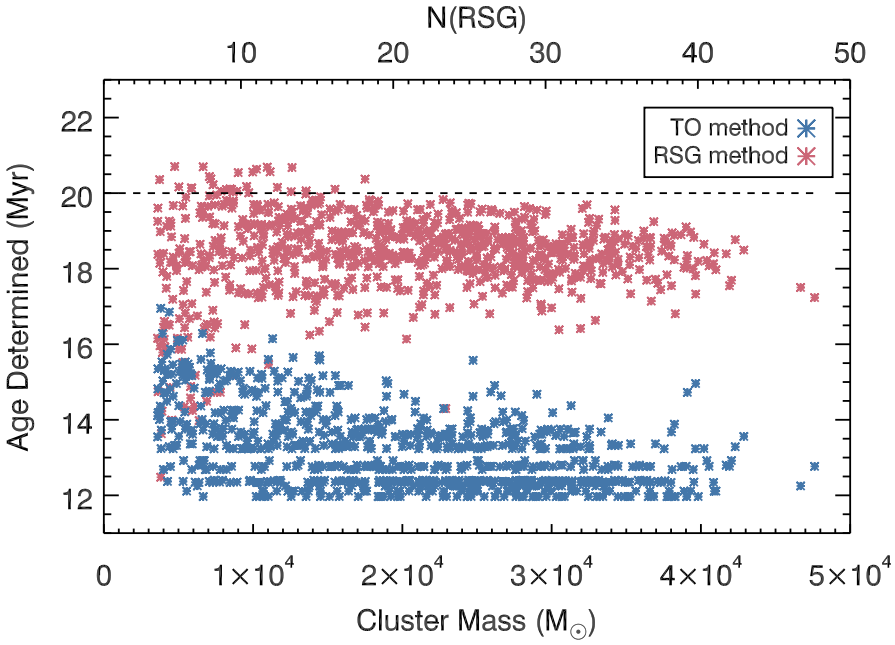

ages determined using the MS stars in a cluster and using the evolved RSGs. The results of this study cannot be explained by rotation on the MS alone, and instead I suggest that the age discrepancies are caused by a combination of rotation, unresolved binaries and binary products (e.g. mergers and mass gainers). I also demonstrate using synthetic clusters that using the lowest $L_{\rm bol}$ RSG method will yield the most reliable age estimation.

Chapter 5

The evolution of red supergiants to supernova III: A new mass-loss rate prescription for RSGs

5.1 Introduction

The ultimate aim of this thesis is to derive a new $\dot{M}$-prescription that can be implemented in stellar evolutionary models. In Chapters 2 and 3 I showed the dispersion on the $\dot{M}$-luminosity relation is greatly reduced when focusing on RSGs of a constrained initial mass. In light of this, using the previously studied clusters (NGC 2100, χ Per, NGC 7419) and two further RSG rich clusters (NGC 2004, RSGC1) and updated ages (see Chapter 4) I will derive an initial mass dependent mass-loss rate.

In Secton 5.2 I describe the sample of clusters and data used, in Section 5.3 I describe the dust shell models and fitting procedure, in Section 5.4 I discuss the results and describe the method of determining $L_{\rm bol}$, and finally in Section 5.5 I discuss the findings in relation to other mass-loss rate prescriptions, and consequences for stellar evolution.

Table 5.1: Cluster properties

Cluster	Distance (kpc)	Age (Myr)	Initial mass ($M_{\odot}$)	$A_{\rm V}$	References
NGC 2100	50±0.1	21 ± 1	10 ± 1	0.5	1,2,5
NGC 7419	$2.93^{+0.32}_{-0.26}$	20 ± 1	11 ± 1	6.33±0.22	2,3
χ Per	$2.25^{+0.16}_{-0.14}$	21 ± 1	11 ± 1	1.22±0.22	2,3
RSGC1	6.6±0.9	10 ± 1	19 ± 1	20.9±0.6	4
NGC 2004	50±0.1	23 ± 1	9 ± 1	0.07	1,2

[1]Pietrzyński et al. (2013), [2]Chapter 4, [3]Davies & Beasor (accepted), [4]Davies et al. (2008), [5]Niederhofer et al. (2015)

5.2 Observations

5.2.1 Sample selection

In previous sections it has been speculated that the cause for large dispersion in many $\dot{M}$-prescriptions is due to the studies' use of field stars, where parameters such as initial mass and metallicity are unconstrained. For this reason, in the study presented here I focus solely on RSGs in clusters, for which initial mass and metallicty are constrained. I also require clusters that span a range of ages, in order to see how the $\dot{M}$-luminosity relation changes as a function of initial mass, ideally across the full range of RSG masses. The sample comprises five RSG rich clusters of varying ages: NGC 2100, NGC 7419, χ Per, RSGC1 and NGC 2004 (see Table 5.1 for cluster properites). By including a younger cluster in our sample, I will be able to anchor down the $\dot{M}$-luminosity relation for high mass RSGs. As the RSG lifetime is very short relative to the MS lifetime, we can assume all of the RSGs currently in the RSG phase are very similar in initial mass, to within $\sim 1 M_{\odot}$(Georgy et al., 2013). Because of this, I will be able to derive an $\dot{M}$-luminosity relation dependent on the initial mass of the star. It can effectively be assumed that each RSG can be considered to be the same star at a different stage of evolution.

Clusters NGC 2100, NGC 7419, χ Per and NGC 2004 have all been discussed in detail in previous chapters 2,3 and 4.

RSGC1

First discovered in Figer et al. (2006), Galactic cluster RSGC1 was notable for its high number of RSGs. Davies et al. (2008) estimated the age of RSGC1 by placing isochrones over the full range of RSGs in the cluster, for which they determined $T_{\rm eff}$ and $L_{\rm bol}$. The kinematic distance to the cluster was found to be 6.60 $\pm$ 0.89 kpc.

Unlike the other clusters in this sample, RSGC1 has high foreground extinction that is non-negligible in the mid-IR ($A_{\rm K} \sim 2.09$). Indeed, the extinction is high enough that for many of the RSGs in the cluster the mid-IR bump at 10μm used to trace mass-loss (see Section 2.2.1) can appear inverted as flux lost at shorter wavelengths is re-emitted. For this reason, the extinction law has had to be carefully derived. To do this, I use an archival Spitzer/IRS spectrum of RSGC14[1] This is the lowest luminosity RSG in the cluster, with no detectable IR excess (Davies et al., 2008). It is assumed that this star has no infrared excess, and therefore the extinction law can be obtained by dividing the IRS spectrum through by an apropriate model atmosphere. This analysis was done by B. Davies, and will be described in Beasor, Davies, Smith et al. (in prep). As we are assuming RSGC14 has no circumstellar extinction, I take the value of reddening towards RSGC14 as the foreground extinction towards the cluster (see Table 5.1).

NGC 2004

NGC 2004 is an LMC cluster containing 7 RSGs, with their cluster membership confirmed by their rotational velocities ($\sim$300 km/s, Massey & Olsen, 2003). As this cluster is located in the LMC, it is unlikely to be severely affected by large amounts of foreground extinction. By comparing the colour-magnitude diagram of this cluster to `PARSEC` isochrones, Niederhofer et al. (2015) estimate a reddening value of $E(B-V)$ = 0.23. The age for NGC 2004 found in this study is older than suggested by Niederhofer et al. (2015),see Chapter 4 for more details.

[1] RSGC14 was outside of the field of view for the data collected here.

Table 5.2: Photometry for RSGC1 from SOFIA-FORCAST. All photometry is in Jy.

ID	5.5μm	7.7μm	11.1μm	25.3μm	31.5μm
F01	6.88 ± 0.05	5.33 ± 0.03	15.07 ± 0.10	12.86 ± 0.06	10.99 ± 0.06
F02	7.10 ± 0.05	5.88 ± 0.03	16.04 ± 0.10	14.74 ± 0.07	12.78 ± 0.08
F03	4.08 ± 0.05	4.44 ± 0.03	9.59 ± 0.10	8.07 ± 0.06	6.93 ± 0.05
F06	2.76 ± 0.05	2.96 ± 0.02	3.51 ± 0.10	1.89 ± 0.05	1.71 ± 0.05
F07	2.70 ± 0.05	2.42 ± 0.03	2.81 ± 0.10	1.28 ± 0.06	1.09 ± 0.07
F09	2.62 ± 0.05	2.56 ± 0.02	3.35 ± 0.10	1.54 ± 0.06	1.44 ± 0.05
F10	2.06 ± 0.05	2.10 ± 0.02	3.03 ± 0.10	1.80 ± 0.06	1.81 ± 0.05
F12	1.66 ± 0.05	1.60 ± 0.03	2.03 ± 0.10	1.17 ± 0.06	0.54 ± 0.06
F13	4.30 ± 0.05	3.18 ± 0.02	7.28 ± 0.10	8.12 ± 0.06	8.51 ± 0.05

5.2.2 Observations and data reduction

For RSGC1, I obtained new mid-IR photometry from SOFIA+FORCAST. The data was taken in Cycle 5 using FORCAST (Prog ID 05 0064, PI Nathan Smith). The cluster was observed in 5.5μm, 7.7μm 11.1μm 25.3μm and 31.5μm filters to cover the majority of the SED. In particular these wavelengths cover the infrared excess and 10μm silicate bump feature used to model the dust shells of the RSGs. The data was reduced using the SOFIA data pipeline `FORCAST Redux`. The data-products I use are the Level 3 flux-calibrated data. To extract the photometry, I used IDL program `starfinder` (Diolaiti et al., 2000) to extract photometry using point source function (PSF) fitting. Our PSF was made by combining the PSFs using median averaging of several isolated stars in the images. The PSF profiles then undergo halo smoothing in the outer regions. To extract photometry, the threshold for star detection is defined as 5-sigma above background (all RSGs have much greater significant than this limit). The errors are assumed to be dominated by the variance in the sky. The photometry for RSGC1 is shown in Table 5.2.

For NGC 2004 we used archival data from several archival sources, including the Magellanic Clouds Photometric Survey (MCPS, Zaritsky et al., 2004), DENIS (Cioni et al., 2000), 2MASS (Skrutskie et al., 2006), IRAC (Werner et al., 2004) and WISE (Wright et al., 2010).

5.2.3 Determining cluster ages

By studying RSGs in stellar clusters it is possible to determine ages and RSG initial massses ($M_{\rm ini}$) by fitting isochrones to observations. Many studies use the cluster main sequence turn off (MSTO) as an anchor point to determine the age. However as shown in Chapter 4, due to the presence of binary products (e.g. mergers or mass gainers) at the MSTO this can cause the age of the cluster to be underestimated, and suggest RSG masses that are too high. For this reason, it was necessary to develop a new age diagnostic for star clusters, insensitive to the effects of rotation or binary evolution. This is described in detail in the previous chapter.

Here, I use the lowest luminosity RSG method to determine an age for the cluster, discussed at length in Chapter 4. This method relies upon the assumption that the lowest luminosity RSG is that which is least susceptible to the effects of binary interaction and rotation. The ages found from the lowest $L_{\rm bol}$ RSG are shown in Table 5.1. The RSGs in this sample span initial masses between 8 and 19$M_{\odot}$, covering the majority of the initial mass range predicted to end their lives as Type IIP SN.

Note that the ages presented in this chapter supersede the results from Chapter 3. Previously, for NGC 7419 and χ Per, the ages were estimated by comparing isochrones to the MSTO of the cluster (Marco & Negueruela, 2013; Currie et al., 2010). In Chapter 4 I discussed at length the difficulties in determining ages for young stellar clusters using the MSTO, due to the presence of blue straggler-like objects (i.e. objects formed by mass-transfer or merging).

5.3 Spectral energy distribution modeling

The model setup has been described in detail in Beasor & Davies (2016) and again in Beasor & Davies (2018). Below I will briefly describe the model setup and chosen input parameters.

Throughout this work I use dust shell models from `DUSTY` (Ivezic et al., 1999), a

code which solves the radiative transfer equation for a star surrounded by a spherically symmetric layer of dust of a given optical depth ($\tau_{\rm V}$, optical depth at 0.55μm), inner dust temperature ($T_{\rm in}$) and radial density profile ($\rho_{\rm r}$).

Dust surrounding a star leaves signatures in the output spectrum, as the light is absorbed and re-processed. From this it is possible to determine the chemical composition of the dust surrounding the star, and how much of it there is. The 10μm silicon 'bump', indicative of oxygen rich dust, has been observed around many RSGs (e.g. Smith et al., 2009), and hence I opted for silicate dust as described by Draine & Lee (1984) with a fiducial grain size of 0.3μm (see Section 2.2.1). I assume a gas-to-dust ratio ($r_{\rm gd}$) of 200 for the MW clusters and 500 for the LMC cluster (Van Loon et al., 2005). For all stars I assumed a grain bulk density $\rho_{\rm d}$ of 3 g cm^{-3}. Together, these parameters allow a dust shell mass to be derived for each model.

To calculate $\dot{M}$, I also need to make assumptions about the density profile of the dust and the outflow velocity of the winds. As in the previous chapters, I have used a steady state wind with a density distribution that falls off with r^{-2}. The stars in this sample do not have measured outflow velocities, I therefore use a uniform speed of 25$\pm$5 km/s, consistent with measurements taken for other RSGs (Richards & Yates, 1998; Van Loon et al., 2001). With this, I can calculate $\dot{M}$ using the following equation

$$\dot{M} = \frac{16\pi}{3} \frac{R_{in} \tau_V \rho_d a v_\infty}{Q_V} r_{\rm gd} \tag{5.1}$$

where Q_V is the extinction efficiency of the dust (as defined by the dust grain composition, Draine & Lee, 1984).

It is also necessary to assume an effective temperature ($T_{\rm eff}$) for the RSGs. There is some controversy over the temperatures of RSGs (Levesque et al., 2005; Davies et al., 2013), and so this study explores a temperature range of 3600-4200K, with 3900K being the fiducial SED.

The fitting procedure has been described in detail in Chapters 2 and 3. In this chapter I have used a grid spanning inner dust temperatures of 0 - 1200K in steps of 100K and

Figure 5.1: *Left panel:* Model plot for F01 including all contributions to spectrum. The silicate bump at 10μm is clearly visible on the spectra suggesting a large amount of circumstellar material. *Right panel:* Contour plot showing the degeneracy between χ^2 values and best fitting $\dot{M}$ values in units of 10^{-6} M$_\odot$ yr^{-1}. The thickened contour highlights the models within the minimum χ^2+10 limit.

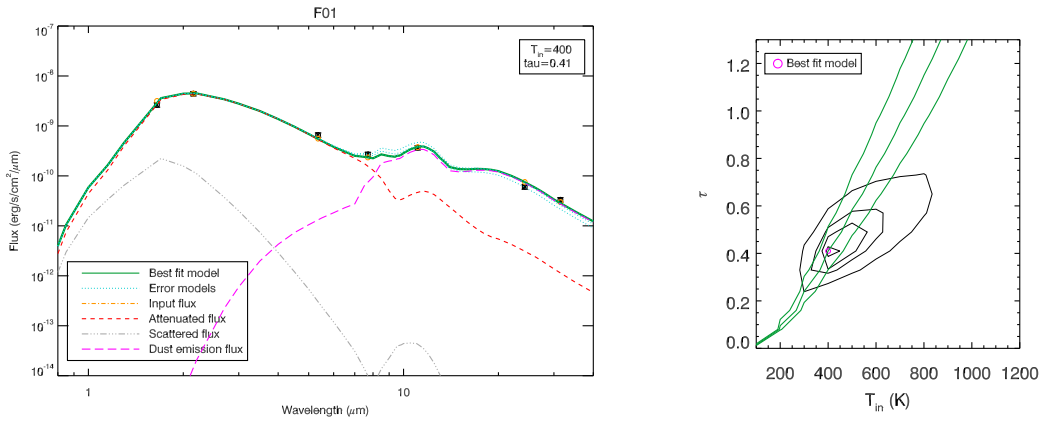

optical depth values of 0 - 4 in steps of $\sim$ 0.08. For each DUSTY model I compute synthetic photometry by interpolating the model flux onto the filter profiles. As in Section 2.2.2, χ^2 minimisation was used to determine the best fitting model.

5.4 Results

The mass-loss rates and luminosities for both clusters are shown in Table 5.3. Figure 5.1 shows the best fit model for the brightest RSG in the sample, F01. The left panel of the plot shows the best fit model spectra (green line), the models within the error range (blue dotted lines) as well as the photometric points, where the black crosses shown the real photometry and orange circles show the model photometry. This plot also shows all contributions to the output spectrum, including the dust emission flux and flux from scattered light. The right hand panel shows the best fit model located on a $T_{\rm in}$ - τ plane with the mass-loss rate isocontours overplotted, demonstrating the degeneracy between $T_{\rm in}$ and τ_V.

Figure 5.2 shows $L_{\rm bol}$ versus $\dot{M}$ for the two clusters presented here, from which we can see an increase in $\dot{M}$ with luminosity. I have also included the results from clusters in previous Chapters corrected for new distances and ages.

5.4.1 Luminosities

The luminosities for the RSGs in NGC 2004 were calculated by integrating under the observed spectral energy distribution (SED), as in Davies & Beasor (2018). I took all of the available photometry and integrated underneath the points using IDL routine `int_tabulated`. To include any flux that may be missing from shorter wavelengths, the SED was extrapolated using a blackbody curve that was fitted to the shortest wavelength available photometry, in this case B-band. Although it should be noted that the contribution to the overall luminosity from this region of the SED is extremely small ($<$0.01 dex).

For RSGC1, I did not estimate the luminosity from the SED. This is because the shortest wavelength photometry available was at 2MASS-J, and the extrapolated flux would contribute a large fraction to the luminosity estimate. For this reason I use the best fit model from `DUSTY` to extrapolate the fluxes below 1μm. Therefore, the errors are dominated by the uncertainty in $T_{\rm eff}$.

The star F13 is anomalously red compared to the other RSGs in the cluster Davies et al. (2008), either due to circumstellar extinction or additional foreground extinction. It is therefore likely $L_{\rm bol}$ will be underestimated as we have assumed the same extinction value for all stars. When taking into account the extra extinction ($A_{\rm K} \sim 0.9$[2]) the luminosity increases to $\log(L/L_{\odot})$=5.39 (from $\log(L/L_{\odot})$=5.01). Due to the uncertainty in the true luminosity of this star I have not included it in calculating an $\dot{M}$ - luminosity relation for the cluster (See Section 6.1), though when adopting the hgiher extinction value for this star it agrees perfectly with the other stars in the cluster.

For NGC 7419 and χ Per, due to updated distances from Gaia (Gaia Collaboration et al., 2018, , see Davies & Beasor, accepted) the luminosities have also changed since they were published in Beasor & Davies (2018), and are now lower by an average of 0.1 dex. The $\dot{M}$ values plotted are scaled in accordance with the updated luminosities.

[2]This extinction corresponds to an $A_{\rm V}$ of 9 mag. If this extinction was due to CSM it would imply an extreme $\dot{M}$, which itself is not consistent with the modest mid-IR excess observed. This extra extinction is therefore likely foreground.

Table 5.3: Fitting results for the RSGs in RSGC1 and NGC 2004.

Cluster	Star	$T_{\rm in}$ (K)	τ_V	$\dot{M}$ (10^{-6}M$_\odot$ yr^{-1})	$L_{\rm bol}$
RSGC1	F01	400^{+100}_{-0}	$0.41^{+0.08}_{-0.00}$	$7.94^{+2.22}_{-1.59}$	5.40 ± 0.12
	F02	400^{+100}_{-0}	$0.49^{+0.16}_{-0.08}$	$9.46^{+3.62}_{-2.44}$	5.38 ± 0.12
	F03	400^{+100}_{-0}	$0.33^{+0.16}_{-0.00}$	$5.33^{+2.79}_{-1.07}$	5.25 ± 0.07
	F06	600^{+300}_{-100}	$0.16^{+0.08}_{-0.00}$	$1.12^{+0.60}_{-0.22}$	5.14 ± 0.11
	F07	900^{+300}_{-500}	$0.16^{+0.08}_{-0.08}$	$0.57^{+0.31}_{-0.31}$	5.13 ± 0.11
	F09	900^{+300}_{-400}	$0.24^{+0.09}_{-0.08}$	$0.80^{+0.34}_{-0.31}$	5.06 ± 0.08
	F10	500^{+100}_{-0}	$0.16^{+0.00}_{-0.00}$	$1.39^{+0.28}_{-0.28}$	5.07 ± 0.11
	F12	600^{+500}_{-100}	$0.08^{+0.08}_{-0.00}$	$0.49^{+0.50}_{-0.10}$	5.04 ± 0.12
NGC 2004	SV* HV 2595	1200_{-200}	$1.39^{+0.81}_{-0.57}$	$43.29^{+28.71}_{-9.74}$	5.15 ± 0.04
	LHA 120-S 43	–	–	< 1.09	4.85 ± 0.05
	Cl* NGC 2004 E 33	–	–	< 0.84	4.35 ± 0.05
	W61 22-9	–	–	< 0.54	4.55 ± 0.05
	Cl* NGC 2004 BBBC 431	–	–	< 0.55	4.55 ± 0.05
	W61 18-13	–	–	< 1.96	4.58 ± 0.05

Figure 5.2 shows $\dot{M}$ versus luminosity for 4 of the clusters presented in this work. For RSGC1, the correlation between $\dot{M}$ and luminosity has a Pearson value of 0.96. For NGC 2004, only the most luminous star has an $\dot{M}$ measurement; the rest of the stars in this sample are upper limits only. I therefore choose not to include these objects in any further analysis.

5.5 Discussion

5.5.1 The $\dot{M}$-luminosity relation for red supergiants

Empirically derived $\dot{M}$- prescriptions are vital input for stellar evolutionary models. It is from the mass-loss that the onward evolution of RSGs is predicted, as the amount of mass lost determines where the star ends up on the HR diagram, which in turn determines the final fate of the star. The most commonly used prescription, that of De Jager et al. (1988), was determined by compiling $\dot{M}$ values for 271 field stars from various other studies. Of this sample, there are 15 RSGs included in the sample, with no constraints on initial mass. This prescription is dependent only on the luminosity of the star.

I have previously shown that by keeping $M_{\rm ini}$ constrained, the $\dot{M}$- luminosity relation is a tighter correlation with a dispersion of only 0.4 dex (Chapters 2 & 3). I now focus on different mass RSGs, including the higher mass RSGs in RSGC1, where the impact of mass-loss could be more significant. I cannot derive a relation for the RSGs in NGC 2004 as apart from the brightest star (SV* HV 2595) all of the measurements on $\dot{M}$ are upper limits. I now use `IDL` routine `FITEXY` to determine the $\dot{M}$-luminosity relations for all other clusters in the sample. From this I find a relation of

$$\log(\dot{M}/M_{\odot}yr^{-1}) = a + b\log(L_{\rm bol}/L_{\odot}) \tag{5.2}$$

where the values of a and b are shown in Table 5.4.

Figure 5.2: Plot showing $\dot{M}$ versus $L_{\rm bol}$ for all clusters studied here.

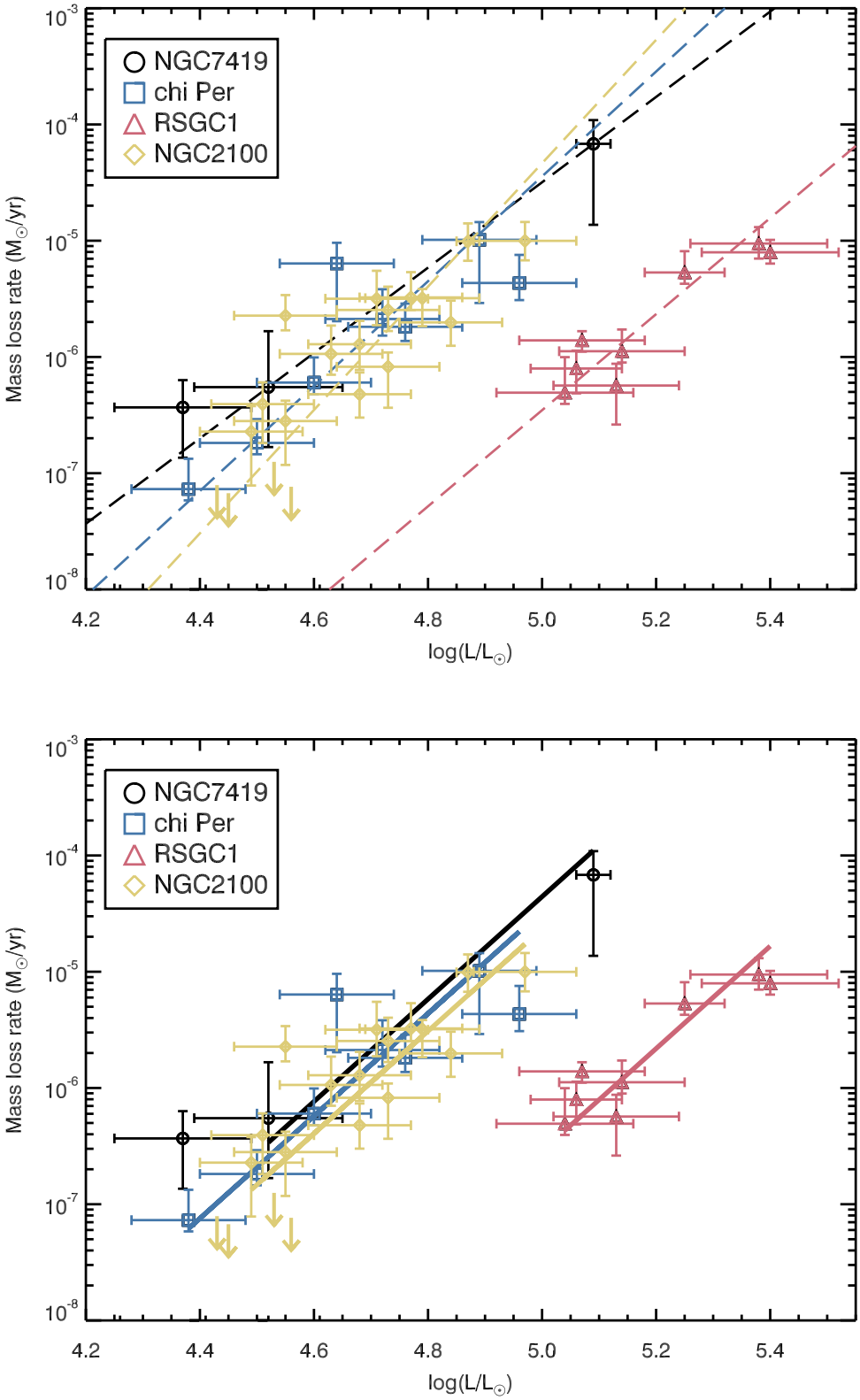

Table 5.4: $\dot{M}$ relation parameters for each cluster. The $\dot{M}$-luminosity relation is in the form $\log(\dot{M}/M_{\odot}yr^{-1}) = a + b\log(L_{\rm bol}/L_{\odot})$

Cluster	Offset (a)	Gradient (b)
NGC 2100	-30.9 ± 3.6	5.3 ± 0.8
NGC 7419	-22.9 ± 4.9	3.6 ± 1.7
χ Per	-27.0 ± 4.9	4.5 ± 1.0
RSGC1	-27.1 ± 7.0	4.1 ± 1.4

I now have $\dot{M}$-luminosity relations for RSGs across a range of initial masses. Using the updated cluster ages found in Chapter 4 I have rederived initial masses for RSGs, shown in Table 5.1. All of the $\dot{M}$-luminosity relations are shown in Fig. 5.2.

The gradients of each $\dot{M}$-luminosity relation are consistent to within the errors. Taking the average of these gradients, I now fix the gradient of the $\dot{M}$-luminosity relation for each cluster, see the bottom panel of Fig. 5.2. I choose to fix the gradient in order to reduce the number of degrees of freedom in the fit. By fixing the gradients, there is only one free parameter that needs to be calibrated, which in turn leads to more reliable results when extrapolating outside of the observed parameter space. With the gradient fixed, I find the mass-dependent offset. Figure 5.3 shows the relation of initial mass with offset, with a Pearson correlation coefficient of -0.97. It can be seen clearly from this plot that the offset of the relation is related to the initial mass of the RSGs, with the higher mass RSGs having the larger offsets.

From this, I am able to establish a new $\dot{M}$-prescription dependent on the initial mass of the star. A more general $\dot{M}$-luminosity relation can be derived,

$$\log(\dot{M}/M_{\odot}yr^{-1}) = (-23.9 - 0.25 \times M_{\rm ini}/M_{\odot}) + b\log(L_{\rm bol}/L_{\odot}) \tag{5.3}$$

where $b = 4.4 \pm 0.6$. This dependence of offset on initial mass explains why many other $\dot{M}$ prescriptions have such high dispersions, as changing $M_{\rm ini}$ causes the relation to become 'smeared' across luminosities. At fixed luminosity, RSGs have higher $\dot{M}$ at lower initial mass. This is to be expected, since lower mass implies lower surface gravity, which presumably makes winds easier to drive.

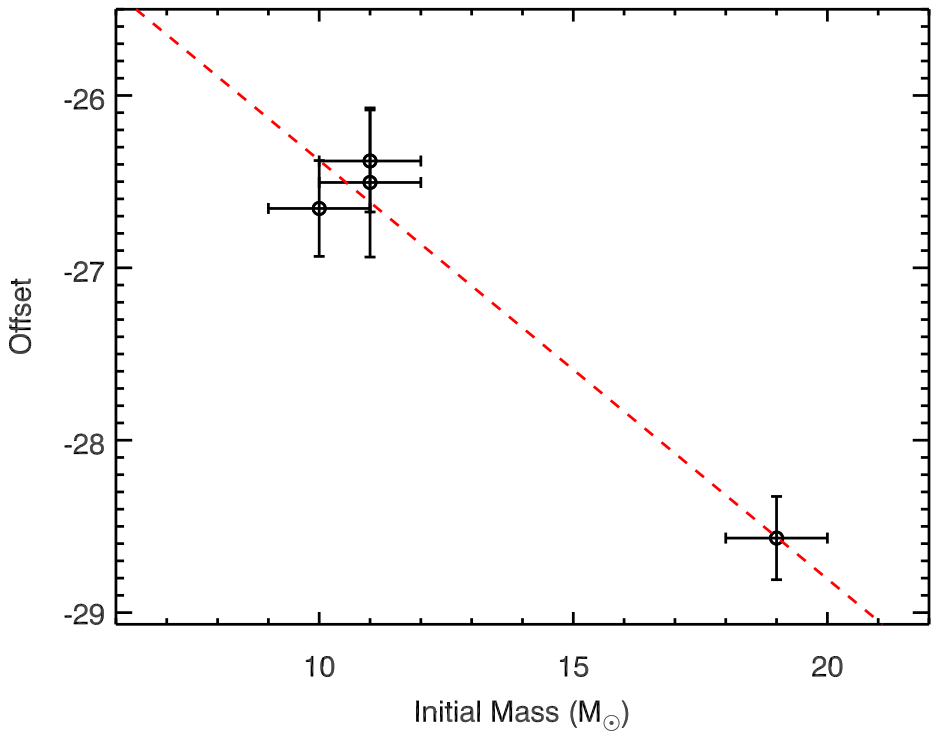

Figure 5.3: The relation between offset and initial mass.

5.5.2 Comparison to other $\dot{M}$-prescriptions

I now compare this new prescription to others commonly used in stellar evolutionary codes. To do this, I calculate the residuals for each prescription, by subtracting the mass-loss rate found from the relation to the measured value of $\dot{M}$. For comparison I compare the results to the de Jager prescription (De Jager et al., 1988), van Loon (Van Loon et al., 2005) and the more recent Goldman et al. (2017) prescription. Results are shown in Fig. 5.4, with the root mean square (RMS) and mean values shown in Table 5.4. To estimate RMS and offset I use only mass-loss rates higher than 10^{-6}M$_\odot yr^{-1}$, as below this the value of $\dot{M}$ is negligible. This prescription provides the most accurate results, with an RMS of $\pm$0.37 dex.

The dispersion on the De Jager et al. (1988) prescription is $\pm$0.47 dex where a systematic offset results in an average overprediction of $\dot{M}$ for a given star by 0.12 dex. It can be seen in Fig. 5.4 that this is particularly evident for the highest luminosity

Figure 5.4: Plot showing the residual $\dot{M}$ value for each star using the $\dot{M}$ prescriptions from this work, De Jager et al. (1988).

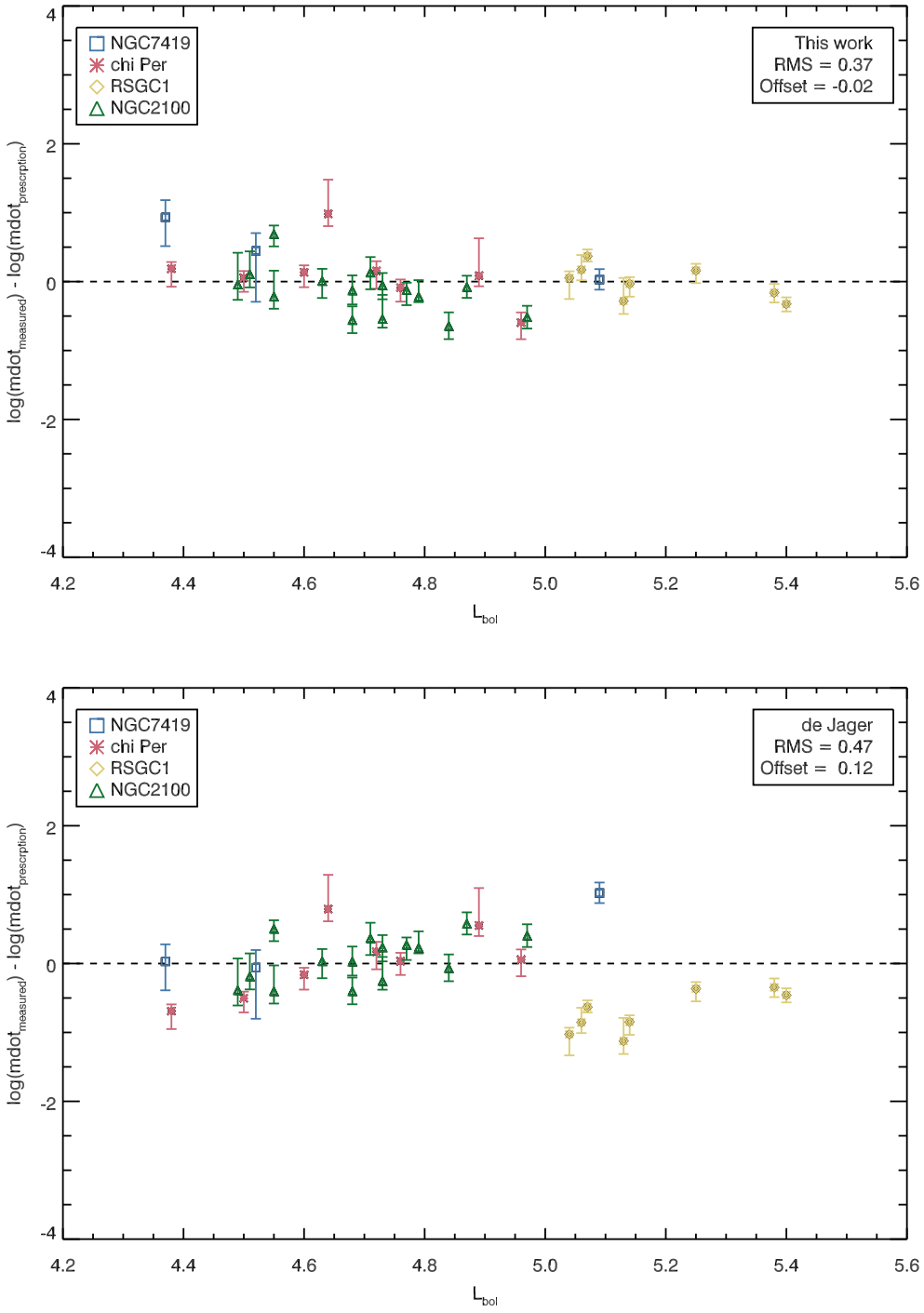

Figure 5.5: Same as above for $\dot{M}$-prescriptions from Van Loon et al. (2005) and Goldman et al. (2017).

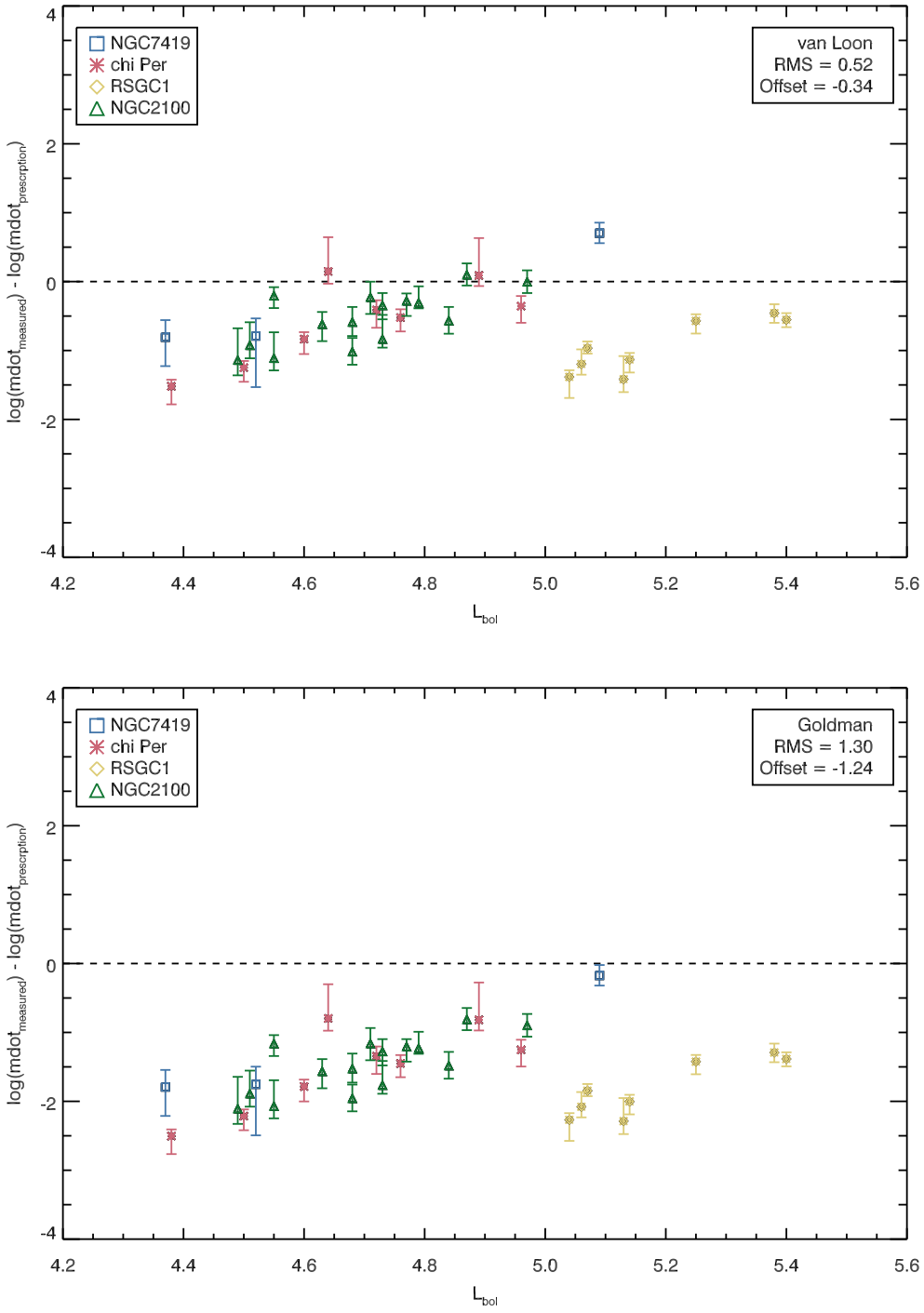

stars ($\log(L/L_{\odot}) > 5$), where the mass-loss rates are systematically overestimated by a factor of 10. The dJ88 prescription performs particularly badly for the highest $L_{\rm bol}$ (and hence $M_{\rm ini}$) RSGs, for which $\dot{M}$ presumably has the greatest potential effect.

The van Loon and Goldman prescriptions both lead to large dispersions ($\pm$ 0.52 dex and $\pm$ 1.30 dex respectively) and in all cases over predict the amount of mass lost, by factors of $\times$2 and $\times$16 respectively (see Fig. 5.5). As discussed in previous papers (Mauron & Josselin, 2011; Beasor & Davies, 2016, 2018) both studies select stars with enhanced mass-loss, by either selecting dust enshrouded objects (Van Loon et al., 2005) or maser emitters (Goldman et al., 2017). It is likely that the stars chosen in these studies, are at the later stages of evolution and are experiencing the highest levels of mass-loss, and hence aren't representative for RSGs in the earlier phases of evolution. Looking at the results (bottom two panels in Fig. 5.2), if one is to follow the residuals for a cluster, the dispersion at later stages of evolution (higher luminosities) is smaller, supporting the hypothesis that both the van Loon and Goldman prescriptions are applicable for RSGs at the end of their lives. While these prescriptions are perhaps not appropriate for input into stellar evolutionary models, they have the advantage of not requiring an initial mass, and so have the potential to be used to estimate $\dot{M}$ for stars with strong pulsations (e.g. Mira variables).

5.5.3 Total mass lost during the RSG phase

Knowing how much mass is lost by a star prior to explosion is an important constraint on the appearance of the eventual SN. It is predicted that stars with initial masses between 8 and 25M$_{\odot}$ will evolve through the RSG phase before exploding as a Type IIP SN, while stars above this mass range are predicted to shed their outer envelope and explode in the blue region of the HR diagram.

There is a maximum limit to how much mass an RSG can lose, determined by the mass of the H-rich envelope. If this is removed completely, the star cannot remain in the red of the HR diagram, and instead will evolve back to the blue. Using the MIST

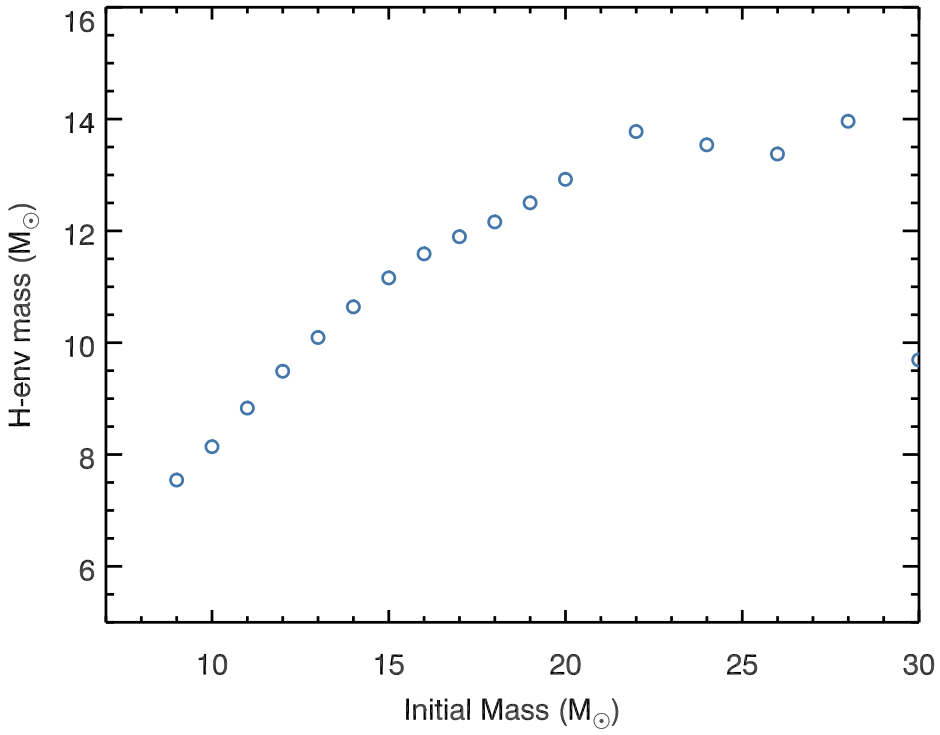

Figure 5.6: Mass of the H-rich envelope at the end of the MS for a star as a function of initial mass using the MIST mass tracks (see text for details).

models (Dotter, 2016; Choi et al., 2016; Paxton et al., 2010, 2013, 2015), it is possible to determine how envelope mass changes as a function of initial mass, see Fig. 5.6. This figure shows the envelope mass for a star of a given initial mass at the beginning of the RSG phase, where envelope mass is estimated by subtracting the helium core mass from the mass of the star at the end of the MS. For an RSG with an initial mass of $20M_{\odot}$ to evolve to the blue of the HR diagram, it would have to lose $\sim$13M$_{\odot}$ of mass during the RSG phase prior to explosion. If we assume the RSG phase is 10^6yrs, this would require an average sustained $\dot{M}$ of $10^{-5}M_{\odot}$ yr^{-1}, a mass-loss rate only observed for the brightest and most evolved RSGs in this sample.

I now compare the amount of mass lost for 12, 15, 20 and 25M$_{\odot}$ stars in the Geneva mass tracks[3]. For each mass track, I begin by plotting $\dot{M}$ as a function of luminosity,

[3]For the purposes of this study I compare thew new $\dot{M}$-prescription to Geneva models only as these models are optimised for massive stars in terms of how they are calibrated (for example overshooting and rotation). As well as this, they are also the most commonly used stellar evolutionary model in the field.

shown in Fig. 5.7. Note the increase in $\dot{M}$ by a factor of 3 at masses of $20M_{\odot}$ and over, this arbitrary inrease of $\dot{M}$ is implemented in the models when the stars become super-Eddington (Ekström et al., 2012) and contributes to a large fraction of the predicted mass-loss. For comparison, at each time step I recompute a value for mass-loss using our $\dot{M}$-prescription. In this case, I have not measured values of $\dot{M}$ below $\sim 10^{-7} \mathrm{M}_{\odot} yr^{-1}$ and so I regard this section of the plot as uncertain, although the contribution to overall mass lost in this region is negligible. I also caution that the $25M_{\odot}$ model lies outside of the empirical range of this study (9-19$M_{\odot}$), and so results here require an extrapolation of the $\dot{M}$-prescription. Figure 5.7 shows $\dot{M}$-prescription being implemented in the Geneva stellar models is dependent only on the currently luminosity of the star, leading to an over-prediction of the total mass lost during the RSG phase by up to a factor of 20. This result suggests stellar models could be over-predicting the number of stars that evolve to the blue of the HR, and hence *under-predict* the H-rich SN rate.

I now compare the predicted total amount of mass lost during the RSG phase (M_{tot}) from the Geneva models and the $\dot{M}$ prescription presented in this work, under the assumption that changing $\dot{M}$ does not change the core evolution (and hence luminosity evolution) of the star[4]. At each timestep a value for $\dot{M}$ is calculated using the L_{bol} and initial mass of the star. Figure 5.8 shows the mass of the star as a function of time (scaled by MS lifetime). The solid lines show the mass of the star directly taken from the Geneva mass tracks (i.e. dJ88) and the dashed lines show the results when using the new $\dot{M}$-prescription. The current $\dot{M}$ implementation in Geneva predicts a higher M_{tot} for all initial masses included here. Indeed, for the $20M_{\odot}$ star, I predict a total mass-loss through the RSG phase of $0.63M_{\odot}$ while the current $\dot{M}$ implementation predicts a total mass-loss of $9M_{\odot}$.

The factor which determines what kind of SN will be seen is the mass of the remaining H-rich envelope at core-collapse. For stars which retain their envelope, the resulting SN will appear as a Type II H-rich SN, while those that lose their envelope will evolve

[4]I plan to repeat the comparison of current $\dot{M}$ implementation in stellar models, recomputing the evolution of the star with the new $\dot{M}$-prescription using MESA, see Section 6.1.

to become WR stars before exploding as Type Ibc 'stripped' SN. The Geneva mass tracks do not provide a value for envelope mass ($M_{\rm env}$) explicitly, and so I derive a lower limit for $M_{\rm env}$ by subtracting the convective core mass at the end of the MS from the mass of the star. I now use this to estimate the mass lost as a fraction of the envelope mass prior to SN, see Fig. 5.9. In this figure, the MS is plotted. The point at which the dashed line becomes visible is the point at which the RSG mass-loss comes into effect. Our $\dot{M}$-prescription suggests that very little of the envelope mass is lost in the RSG phase, whereas the $\dot{M}$ currently implemented in the Geneva models suggests as much as 50% of the envelope can be lost during this period. It is this loss of envelope mass that drives the stars back to the blue of the HR diagram (see the $25 M_{\odot}$ track in Ekström et al., 2012).

The results of this study suggest that quiescent mass-loss during the RSG phase cannot be the sole evolutionary driver for massive stars. From the clusters studied here, there is no evidence for enhanced $\dot{M}$ during the RSG phase and there is no physical motivation for stellar evolutionary models to ramp up $\dot{M}$ in order to explain the RSG problem (e.g. Georgy et al., 2013).

5.5.4 Implications

LBVs as post-RSG objects

Another evolutionary stage during which massive stars can lose a considerable amount of H-envelope mass is the luminous blue variable (LBV) phase. LBVs are hot massive stars, which exhibit large variations in brightness and powerful episodic mass-loss events. It was thought for a long time that all massive stars experience a brief LBV phase (10^4yr) prior to becoming Wolf-Rayet stars, where the strong episodic mass-loss can remove the majority of the remaining H-rich envelope (Humphreys & Davidson, 1994). However, more recent work has claimed that the apparent isolation of LBVs (with respect to O stars) suggests that they are unlikely to be very massive (Smith, 2014). It was instead suggested that LBVs are likely products of binary evolution,

Figure 5.7: Plot showing $\dot{M}$ as a function of time using the Geneva mass tracks at 12, 15, 20 and $25 M_{\odot}$. At each timestep, I use the new $\dot{M}$-prescription derived here and calculate a new value for mass-loss.

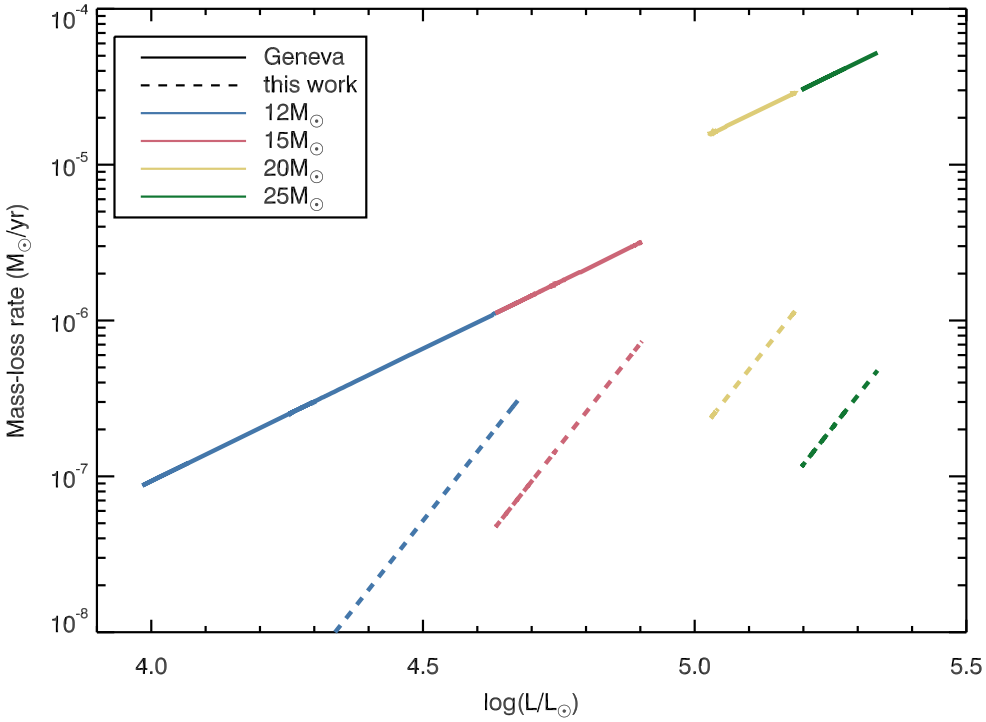

whereby the LBV is the mass-gainer of a system.

In another counter-claim, additional evidence for LBVs as post-RSG objects in single star evolution was presented by Groh et al. (2013). In this paper, stellar evolution models were coupled with radiative transfer modeling (using CMFGEN, Hillier & Lanz, 2001) to predict the appearance of SN progenitors prior to explosion. Using the De Jager et al. prescription for the RSG phase of evolution, the authors found that the 20 and $25 M_{\odot}$ pre-SN spectra of the progenitors looked remarkably similar to those of LBVs, implying previously unknown evolutionary paths for lower mass stars,

$20\mathrm{M}_{\odot} : RSG \longrightarrow BSG \longrightarrow LBV \longrightarrow SN;$

$25\mathrm{M}_{\odot} : RSG \longrightarrow WR \longrightarrow LBV \longrightarrow SN;$

Under this paradigm, following the RSG phase the star has shed enough mass to move back to the blue of the HR diagram and become a blue supergiant (BSG) before ex-

Figure 5.8: Change in current mass of 12, 15, 20 and 25$M_\odot$ stars as a function of time.

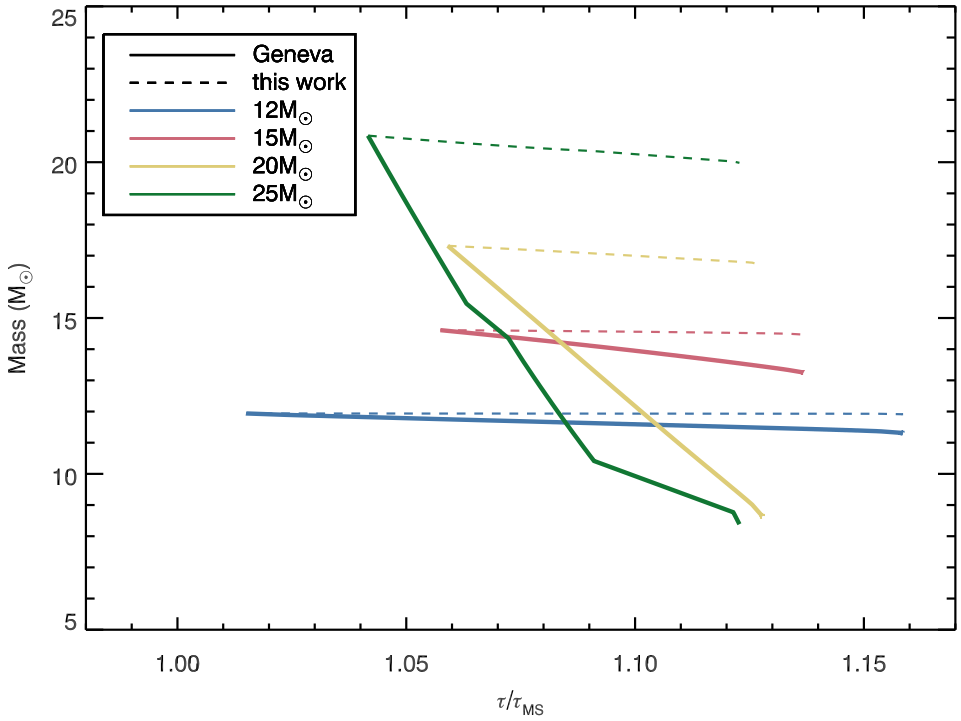

Figure 5.9: Total mass lost during the RSG phase compared to the mass of the envelope as a function of time.

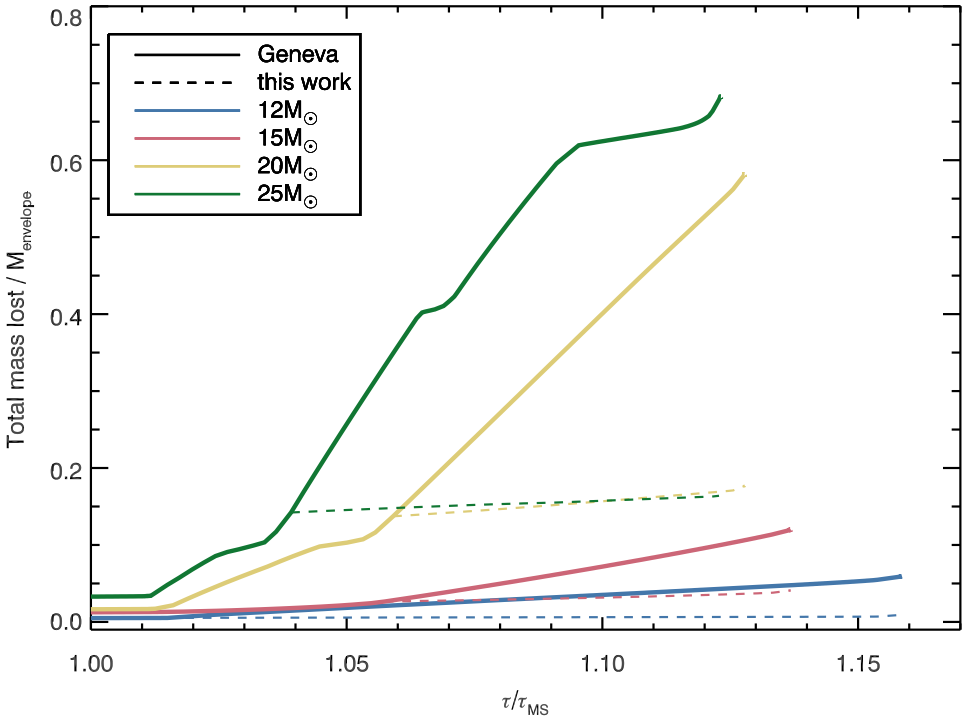

ploding as an LBV. A very similar path was predicted for the $25M_{\odot}$ model, but a Wolf-Rayet phase instead of a BSG phase.

The LBV as post RSGs scenario is only viable if the mass-loss during the RSG phase is sufficient enough to evolve the star back to the blue. At present, I find the implementation of mass-loss in the Geneva models over-predicts the total amount of envelope mass lost during the RSG phase. This is exacerbated by the increase of $\dot{M}$ by a factor of 3 (Ekström et al., 2012; Georgy et al., 2013) for stars with initial masses of $20M_{\odot}$ and above. The results of this thesis show clearly that for stars of $20M_{\odot}$ and below, mass-loss during the RSG phase is not enough to remove the H-envelope and cause blue-ward motion. Though admittedly the empirical range of this study is 8-19$M_{\odot}$, it is unlikely that the envelope of 20–30$M_{\odot}$ can be removed by quiescent RSG winds unless there is a large step change in $\dot{M}$ for more massive RSGs.

SN interaction with CSM

When IIP progenitors explode there is observational evidence showing they crash into a dense CSM, such as the slow rise time (e.g. Khazov et al., 2016) and brief IIn phase (e.g. Smith et al., 2015). In order to reproduce these observations, it has been claimed that the CSM must be very close to the star (i.e. within a stellar radius) and very dense (e.g. Morozova et al., 2017). This was modeled by Moriya et al. (2018), who suggest $\dot{M}$ values of 10^{-3}–$10^{-2}M_{\odot}$ yr^{-1} to explain rise times of 5–10 days in IIP SN. These mass-loss rates are substantially higher than we find for any object in our sample. In this work, I find that the amount of mass lost throughout the RSG phase (lasting approximately 10^6yrs) is very small even for the most massive progenitors. For a $25M_{\odot}$ RSG I predict only a total mass lost of $0.8M_{\odot}$, which would correspond to approximately $8\times10^{-4}M_{\odot}$ of material within 1 stellar radius. A level of mass-loss this low is unlikely to have an effect on the observed SN light curve Smith et al. (e.g. 2016). Of course, this does not take into account any mass lost during potential periods of enhanced mass-loss (see later).

To explain the apparent disagreement between the $\dot{M}$ values found here and those be-

ing claimed for SN progenitors, I will now explore the methodology of Moriya et al. (2018) in more detail. The authors modeled RSGs with an acceleration zone to explain the rise times of several Type IIP SN light curves. By adopting wind acceleration parameter (β) values between 1-5, the authors conclude that the slow acceleration of the wind results in a dense CSM lying in the vicinity of the progenitor star upon explosion. However, as the β-law describes wind acceleration for radiatively driven winds (Castor et al., 1975), it is unclear if there is any justification in applying this to RSGs which likely have a very different driving mechanism. Though Moriya et al. (2018) study slowly accelerating winds (β=5), even this is likely far too fast for RSGs, where wind accelerates so slowly that the CSM is likely almost static within the first couple of stellar radii (Harper et al., 2001).

Though I have shown that quiescent mass-loss is extremely ineffective at removing the envelope, I have not yet discussed how the envelope may be removed by a brief period of enhanced mass-loss, e.g. via binary envelope stripping or a short phase of enhanced mass-loss in the decades before explosion (e.g. Smith et al., 2016). Davies et al. (2018) estimated how long a period of enhanced mass-loss would need to last to remove a large fraction of the hydrogen envelope. Assuming any star undergoing this enhanced $\dot{M}$ would be visible as a maser emitter, Davies et al. (2018) found 4 OH/IR emitters in their total sample of 73 RSGs with $\log(L/L_{\odot}) > 5$. Assuming the RSG phase is $\sim$10^{6}yrs, this suggests any 'superwind' phase is on the order of 10^{4}yrs. If the $\dot{M}$ during this time is as high as the maser emitters in the Goldman et al. (2017) sample ($\sim 10^{-4} M_{\odot}\mathrm{yr}^{-1}$), several Solar masses of envelope could be lost.

5.6 Conclusions

The evolution of massive stars relies upon accurate knowledge of the mass-loss rates during the RSG phase. While an $\dot{M}$ relation found from first principles cannot be attained, models input empirically derived $\dot{M}$ recipes.

The work presented here has shown that there is no observationally motivated reason

to increase the value of $\dot{M}$ by factors of 3 or more in stellar evolution models. By doing so, models are underpredicting the amount of H-envelope remaining intact prior to explosion, and are also potentially underpredicting the rate of hydrogen rich SN. If the $\dot{M}$-prescription derived here were implemented into stellar evolution models, the maximum initial mass of RSGs would be found to be far higher than is currently suggested, with luminosities potentially reaching as high as $\log(L/L_{\odot})$=6. As we do not see RSGs above a luminosity of $\log(L/L_{\odot})$=5.5, this strongly implies another effect is causing this maximum luminosity.

Chapter 6

Conclusions and future work

The aim of this thesis has been to update and refine our understanding of RSG mass-loss. Many studies have shown that the impact of $\dot{M}$ on the evolution of massive stars can be huge, with the potential to divert a star from the RSG phase back to the blue, having a significant knock on effect to many astrophysical observables, such as supernova rates and the mass-metallicity relation for galaxies. Putting constraints on mass-loss during the RSG phase will result in more accurate predictions from stellar evolution models.

The $\dot{M}$-prescription currently used in most stellar evolution codes, the de Jager prescription (De Jager et al., 1988), is a purely empirical recipe derived by collating many observations of $\dot{M}$ and $L_{\rm bol}$ from previous studies, across the full spectral type range O-M. While this work has been a crucial anchor for models, the large dispersion on the relation mean that it is difficult to decipher the true impact of $\dot{M}$ for a given star. As well as this, my work has shown that dJ88 systematically overpredicts $\dot{M}$, particularly for the objects with the highest luminosities.

Here, I have derived a new prescription by focussing on RSGs in clusters, where the initial masses and metallicities are more constrained. Ultimately, in this thesis I have derived a new $\dot{M}$-prescription for RSGs across a range of initial masses (9-19$M_{\odot}$). The large dispersions seen in previous prescriptions is likely due to the use of field stars, causing the prescription to become 'smeared out' in $L_{\rm bol}$-space. The prescription

presented here shows a clear relation between initial mass and the offset. For example, if a star is observed to have a high level of mass-loss, but a relatively low $L_{\rm bol}$, it is likley to be a lower mass RSG nearing the end of its evolution, while an RSG with a relatively low level of mass-loss but a high $L_{\rm bol}$ is likely to be a higher mass RSG that has only recently joined the RSG branch. This is important, as stellar evolutionary models scale $\dot{M}$ off luminosity only, and do not take into account initial masses.

When comparing the level of mass-loss implemented by stellar models to the amount that would be predicted by this new prescription, I have found that the evolutionary models are drastically overpredicting mass-loss during the RSG phase. I have discussed the significant impact such an overprediction can make on our understanding of massive star evolution, with quiescent mass-loss being ineffective at removing the H-envelope. It is possible that a period of extremely high mass-loss in the final 10^4 years before a star explodes could provide a solution to this, but observing such a brief event will prove challenging.

6.1 Future work

The mass-loss rates of yellow supergiants

To truly understand the impact of stellar mass-loss on the evolution of a star, we need to be able to accurately characterise $\dot{M}$ at all evolutionary phases of a star's life. Prior to becoming RSGs, stars pass through the so-called "Yellow Void", another cool supergiant phase during which $\dot{M}$ can dominate evolution.

Arguably, our understanding of yellow supergiant (YSG, 5000K $< T_{\rm eff} <$ 10,000K) mass-loss is even worse than that of RSGs. The de Jager prescription for stars in the YSG phase is based on only seven stars. This sample provides the basis for the average mass-loss rate for the YSG phase, despite the fact these measurements have a dispersion of 3 dex with respect to the de Jager prescription. Furthermore, in evolutionary models the YSG phase is prolonged for stars above $15 M_{\odot}$(Ekström et al., 2012; Choi

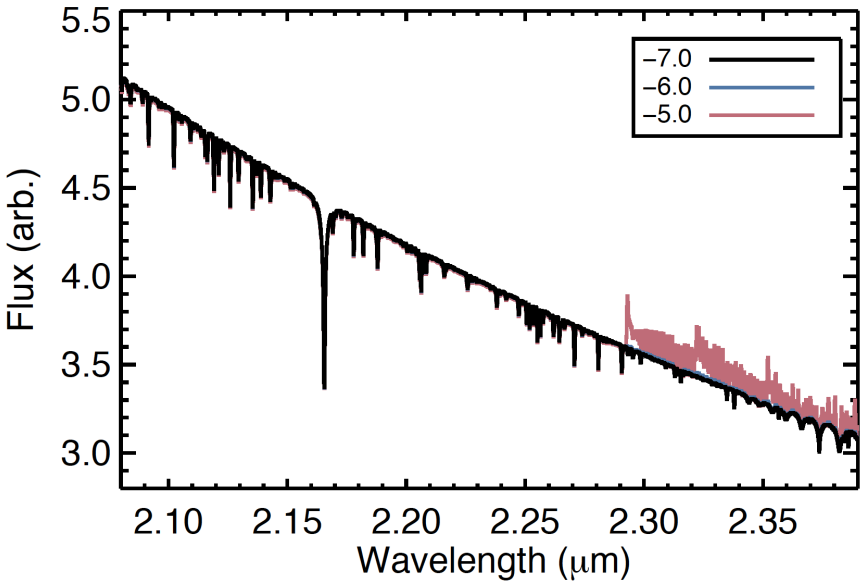

Figure 6.1: Model predictions of the spectral appearance of a YSG ($T_{\rm eff}$=6000K, log(g)=1.0) in the K-band, for 3 representative mass-loss rates. Using the full SED to contrain $T_{\rm eff}$ and $L_{\rm bol}$, the CO band at 2.3μm can be used to determine the mass-loss rate. Taken from Davies, Plez & Beasor (in prep).

et al., 2016). This means that a star with a moderate mass-loss rate of 10^{-5} $M_{\odot}$ yr^{-1}, undergoing a prolonged YSG phase (10^{5} yrs for a 15$M_{\odot}$ star), could easily peel off a substantial fraction if not all of the H-rich envelope. This would cause the star to evolve to become a hot Wolf-Rayet star, which eventually would explode as a H-poor SN (e.g. IIb OR Ibc). Therefore, reliable predictions of the progenitor star - SN connection require accurate mass-loss rates for YSGs as well as for RSGs.

Following on from my work on RSGs, I aim to provide badly-needed revisions to the YSG mass-loss rates. The observational diagnostics of wind density for stars in this temperature regime are molecular emission lines in the near-IR: as mass-loss rates increase throughout the YSG phase, molecules form in the inner part of the wind at density sufficient enough to be observed in the spectrum. Most notably, the CO band at 2.3um goes into emission at the relatively low mass-loss rate of $10^{-6}M_{\odot}$ yr^{-1}, see Fig 6.1. This is a common feature for YSGs (Davies et al., 2008).

For this work I will use archival and my own scheduled VLT+XSHOOTER observations, and model them using the radiative transfer code TURBOSPECTRUM which

has been updated to include the capability to model a wind (Zamora et al. 2014). The stars luminosity, effective temperature and mass-loss rate will be determined by simultaneously modelling the broad spectral energy distribution and the emission-line features of the wind. While the code I will use inevitably has some assumptions (e.g. LTE, radiative equilibrium temperature structure), the mass-loss rates derived here will still be the most reliable to date, far more so than those measurements included in de Jager which underpin modern stellar evolution calculations.

Implementing a new $\dot{M}$-prescription into stellar evolution codes

We know that varying the mass-loss rate prescriptions can cause vastly different outcomes for the evolving star in stellar evolution models, changing where the star will end its life on the HR diagram (e.g. Georgy, 2012), and what type of SN it will produce. The obvious next step of this project is to take the $\dot{M}$-prescriptions determined in this thesis and in the future YSG project and recompute the post-MS evolution of massive stars. To do this, I will build the new mass-loss rate prescription into the stellar evolutionary code MESA (Paxton et al., 2010, 2013, 2015) and compute the evolution of stars up to the end of their lives. This will be done for a range of initial masses, providing predictions for the final luminosities and effective temperatures, envelope masses, surface compositions as a function of initial mass. A grid will be created for ranges of e.g. rotation rates to determine the impact of systematic errors on results. These results will provide the definitive prediction of how single stars end their lives.

By computing new evolutionary models I will be able to derive a mass-luminosity relation for supernova progenitors and the cutoff in initial mass for stripped/unstripped SN, from which I can estimate expected SN rates. This work will also generate a prediction for the Humphreys-Davidson limit for cool supergiants (a key diagnostic of stellar evolution) and allow us to see how the upper luminosity limit is affected by e.g. metallicity and rotation. Stellar evolution codes such as `MESA` also output the surface abundances of a star at any given point. As I will be evolving the stars to the end of their lives, I will be able to predict the terminal surface abundances of SN progenitors,

which are detectable in very early SN spectra (e.g. Groh, 2014), providing another observable from which the progenitor properties may be estimated.

Bibliography

Adams S. M., Kochanek C. S., Gerke J. R., Stanek K. Z., Dai X., 2017, MNRAS, 468, 4968

Aghakhanloo M., Murphy J. W., Smith N., Parejko J., Díaz-Rodríguez M., Drout M. R., Groh J. H., Guzman J., Stassun K. G., 2019, arXiv e-prints

Avni Y., 1976, ApJ, 210, 642

Bastian N., de Mink S. E., 2009, MNRAS, 398, L11

Bastian N., Lardo C., 2018, ARA&A, 56, 83

Bastian N., Niederhofer F., Kozhurina-Platais V., Salaris M., Larsen S., Cabrera-Ziri I., Cordero M., Ekström S., Geisler D., Georgy C., Hilker M., Kacharov N., Li C., Mackey D., Mucciarelli A., Platais I., 2016, MNRAS, 460, L20

Beasor E. R., Davies B., 2016, Monthly Notices of the Royal Astronomical Society, 463, 1269

Beasor E. R., Davies B., 2018, Monthly Notices of the Royal Astronomical Society, 475, 55

Beasor E. R., Davies B., Smith N., Bastian N., 2019, arXiv e-prints

Beauchamp A., Moffat A. F., Drissen L., 1994, The Astrophysical Journal Supplement Series, 93, 187

Bedijn P., 1987, Astronomy and Astrophysics, 186, 136

Bennett P. D., 2010, in Leitherer C., Bennett P. D., Morris P. W., Van Loon J. T., eds, Hot and Cool: Bridging Gaps in Massive Star Evolution Vol. 425 of Astronomical Society of the Pacific Conference Series, Chromospheres and Winds of Red Supergiants: An Empirical Look at Outer Atmospheric Structure. p. 181

Bonanos A., Lennon D., Köhlinger F., van Loon J. T., Massa D., Sewilo M., Evans C., Panagia N., Babler B., Block M., et al., 2010, The Astronomical Journal, 140, 416

Bonanos A., Massa D., Sewilo M., Lennon D., Panagia N., Smith L., Meixner M., Babler B., Bracker S., Meade M., et al., 2009, The Astronomical Journal, 138, 1003

Brocato E., Di Carlo E., Menna G., 2001, A&A, 374, 523

Brott I., de Mink S. E., Cantiello M., Langer N., de Koter A., Evans C. J., Hunter I., Trundle C., Vink J. S., 2011, Astronomy & Astrophysics, 530, A115

Cardelli J. A., Clayton G. C., Mathis J. S., 1988, ApJl, 329, L33

Carney B. W., Janes K. A., Flower P. J., 1985, AJ, 90, 1196

Castor J. I., Abbott D. C., Klein R. I., 1975, ApJ, 195, 157

Chen Y., Bressan A., Girardi L., Marigo P., Kong X., Lanza A., 2015, Monthly Notices of the Royal Astronomical Society, 452, 1068

Chiosi C., Maeder A., 1986, Annual Review of Astronomy and Astrophysics, 24, 329

Chiosi C., Nasi E., Sreenivasan S. R., 1978, A&A, 63, 103

Choi J., Dotter A., Conroy C., Cantiello M., Paxton B., Johnson B. D., 2016, ApJ, 823, 102

Cioni M.-R., Loup C., Habing H., Fouqué P., Bertin E., Deul E., Egret D., Alard C., De Batz B., Borsenberger J., et al., 2000, Astronomy and Astrophysics Supplement Series, 144, 235

Clark J. S., Najarro F., Negueruela I., Ritchie B. W., Gonzalez-Fernandez C., Lohr M. E., 2018, arXiv e-prints

Cowley A. P., Dawson P., Hartwick F. D. A., 1979, PASP, 91, 628

Crain R. A., Bahé Y. M., Lagos C. d. P., Rahmati A., Schaye J., McCarthy I. G., Marasco A., Bower R. G., Schaller M., Theuns T., van der Hulst T., 2017, MNRAS, 464, 4204

Currie T., Hernandez J., Irwin J., Kenyon S. J., Tokarz S., Balog Z., Bragg A., Berlind P., Calkins M., 2010, The Astrophysical Journal Supplement Series, 186, 191

Danchi W., Bester M., Degiacomi C., Greenhill L., Townes C., 1994, The Astronomical Journal, 107, 1469

Davies B., Beasor E. R., , 2017

Davies B., Beasor E. R., 2018, Monthly Notices of the Royal Astronomical Society, 474, 2116

Davies B., Crowther P. A., Beasor E. R., 2018, Monthly Notices of the Royal Astronomical Society, 478, 3138

Davies B., Figer D. F., Law C. J., Kudritzki R.-P., Najarro F., Herrero A., MacKenty J. W., 2008, The Astrophysical Journal, 676, 1016

Davies B., Kudritzki R.-P., Plez B., Trager S., Lançon A., Gazak Z., Bergemann M., Evans C., Chiavassa A., 2013, The Astrophysical Journal, 767, 3

De Beck E., Decin L., de Koter A., Justtanont K., Verhoelst T., Kemper F., Menten K. M., 2010, Astronomy & Astrophysics, 523, A18

De Jager C., Nieuwenhuijzen H., Van Der Hucht K., 1988, Astronomy and Astrophysics Supplement Series, 72, 259

de Mink S. E., Sana H., Langer N., Izzard R. G., Schneider F. R. N., 2014, ApJ, 782, 7

de Wit W., Oudmaijer R., Fujiyoshi T., Hoare M., Honda M., Kataza H., Miyata T., Okamoto Y., Onaka T., Sako S., et al., 2008, The Astrophysical Journal Letters, 685, L75

Decin L., Hony S., de Koter A., Justtanont K., Tielens A. G. G. M., Waters L. B. F. M., 2006, A&A, 456, 549

Deutsch A. J., 1956, ApJ, 123, 210

Diolaiti E., Bendinelli O., Bonaccini D., Close L. M., Currie D. G., Parmeggiani G., 2000, in Adaptive Optical Systems Technology Vol. 4007, Starfinder: an idl gui-based code to analyze crowded fields with isoplanatic correcting psf fitting. pp 879–889

Doggett J., Branch D., 1985, The Astronomical Journal, 90, 2303

Dotter A., 2016, The Astrophysical Journal Supplement Series, 222, 8

Draine B., Lee H. M., 1984, The Astrophysical Journal, 285, 89

Dwarkadas V. V., 2014, Monthly Notices of the Royal Astronomical Society, 440, 1917

Eggleton P. P., 1971, Monthly Notices of the Royal Astronomical Society, 151, 351

Ekström S., Georgy C., Eggenberger P., Meynet G., Mowlavi N., Wyttenbach A., Granada A., Decressin T., Hirschi R., Frischknecht U., et al., 2012, Astronomy & Astrophysics, 537, A146

Eldridge J. J., Stanway E. R., 2009, Monthly Notices of the Royal Astronomical Society, 400, 1019

Elias J., Frogel J., Humphreys R., 1985, The Astrophysical Journal Supplement Series, 57, 91

Ercolano B., Barlow M., Storey P., 2005, Monthly Notices of the Royal Astronomical Society, 362, 1038

Ercolano B., Barlow M., Storey P., Liu X.-W., 2003, Monthly Notices of the Royal Astronomical Society, 340, 1136

Ercolano B., Young P. R., Drake J. J., Raymond J. C., 2008, The Astrophysical Journal Supplement Series, 175, 534

Evans C. J., Lennon D. J., Smartt S. J., Trundle C., 2006, A&A, 456, 623

Feast M., Whitelock P., 1992, Monthly Notices of the Royal Astronomical Society, 259, 6

Figer D. F., MacKenty J. W., Robberto M., Smith K., Najarro F., Kudritzki R. P., Herrero A., 2006, The Astrophysical Journal, 643, 1166

Fraser M., 2016, Monthly Notices of the Royal Astronomical Society: Letters, 456, L16

Gaia Collaboration Brown A. G. A., Vallenari A., Prusti T., de Bruijne J. H. J., Babusiaux C., Bailer-Jones C. A. L., 2018, ArXiv e-prints

Gazak J. Z., Davies B., Bastian N., Kudritzki R., Bergemann M., Plez B., Evans C., Patrick L., Bresolin F., Schinnerer E., 2014, ApJ, 787, 142

Gazak J. Z., Davies B., Kudritzki R., Bergemann M., Plez B., 2014, The Astrophysical Journal, 788, 58

Gehrz R., Woolf N., 1971, The Astrophysical Journal, 165, 285

Georgy C., 2012, Astronomy & Astrophysics, 538, L8

Georgy C., Ekström S., 2015, arXiv preprint arXiv:1508.04656

Georgy C., Ekström S., Eggenberger P., Meynet G., Haemmerlé L., Maeder A., Granada A., Groh J. H., Hirschi R., Mowlavi N., et al., 2013, Astronomy & Astrophysics, 558, A103

Georgy C., Ekström S., Granada A., Meynet G., Mowlavi N., Eggenberger P., Maeder A., 2013, Astronomy & Astrophysics, 553, A24

Georgy C., Granada A., Ekström S., Meynet G., Anderson R. I., Wyttenbach A., Eggenberger P., Maeder A., 2014, A&A, 566, A21

Gerke J. R., Kochanek C. S., Stanek K. Z., 2015, MNRAS, 450, 3289

Goldman S. R., van Loon J. T., Zijlstra A. A., Green J. A., Wood P. R., Nanni A., Imai H., Whitelock P. A., Matsuura M., Groenewegen M. A., et al., 2017, Monthly Notices of the Royal Astronomical Society, 465, 403

Gontcharov G., 2016, Astronomy Letters, 42, 445

Gosnell N. M., Mathieu R. D., Geller A. M., Sills A., Leigh N., Knigge C., 2015, ApJ, 814, 163

Gratton R., Sneden C., Carretta E., 2004, ARA&A, 42, 385

Gratton R. G., Lucatello S., Carretta E., Bragaglia A., D'Orazi V., Al Momany Y., Sollima A., Salaris M., Cassisi S., 2012, A&A, 539, A19

Groenewegen M., Sloan G., Soszyński I., Petersen E., 2009, Astronomy & Astrophysics, 506, 1277

Groenewegen M. A. T., 1994, A&A, 290, 531

Groenewegen M. A. T., 2012, A&A, 540, A32

Groh J. H., 2014, A&A, 572, L11

Groh J. H., Meynet G., Ekström S., 2013, A&A, 550, L7

Gustafsson B., Edvardsson B., Eriksson K., Jørgensen U. G., Nordlund Å., Plez B., 2008, Astronomy & Astrophysics, 486, 951

Harper G. M., Brown A., Lim J., 2001, The Astrophysical Journal, 551, 1073

Hartwick F. D. A., 1970, Astrophys. Lett., 7, 151

Hillier D. J., Lanz T., 2001, in Ferland G., Savin D. W., eds, Spectroscopic Challenges of Photoionized Plasmas Vol. 247 of Astronomical Society of the Pacific Conference Series, CMFGEN: A non-LTE Line-Blanketed Radiative Transfer Code for Modeling Hot Stars with Stellar Winds. p. 343

Höfner S., Olofsson H., 2018, The Astronomy and Astrophysics Review, 26, 1

Huang W., Gies D. R., McSwain M. V., 2010, ApJ, 722, 605

Humphreys R. M., 1983, ApJ, 265, 176

Humphreys R. M., Davidson K., 1979, ApJ, 232, 409

Humphreys R. M., Davidson K., 1979, The Astrophysical Journal, 232, 409

Humphreys R. M., Davidson K., 1994, Publications of the Astronomical Society of the Pacific, 106, 1025

Humphreys R. M., Helton L. A., Jones T. J., 2007, The Astronomical Journal, 133, 2716

Humphreys R. M., McElroy D. B., 1984, ApJ, 284, 565

Humphreys R. M., Nichols M., Massey P., 1985, AJ, 90, 101

Ivezic Z., Nenkova M., Elitzur M., 1999, Astrophysics Source Code Library, 1, 11001

Johnson H. L., Mendoza V. Eugenio E., 1966, Annales d'Astrophysique, 29, 525

Joshi H., Kumar B., Singh K., Sagar R., Sharma S., Pandey J., 2008, Monthly Notices of the Royal Astronomical Society, 391, 1279

Josselin E., Plez B., 2007, A&A, 469, 671

Keller S. C., Mackey A. D., Da Costa G. S., 2011, ApJ, 731, 22

Kervella P., Decin L., Richards A. M. S., Harper G. M., McDonald I., O'Gorman E., Montargès M., Homan W., Ohnaka K., 2018, A&A, 609, A67

Kharchenko N. V., Piskunov A. E., Röser S., Schilbach E., Scholz R.-D., Zinnecker H., 2009, A&A, 504, 681

Khazov D., Yaron O., Gal-Yam A., Manulis I., Rubin A., Kulkarni S., Arcavi I., Kasliwal M., Ofek E., Cao Y., et al., 2016, The Astrophysical Journal, 818, 3

Knapp G., Phillips T., Leighton R., Lo K., Wannier P., Wootten H., Huggins P., 1982, The Astrophysical Journal, 252, 616

Knapp G. R., Chang K. M., 1985, ApJ, 293, 281

Knigge C., Leigh N., Sills A., 2009, Nature, 457, 288

Kochanek C., Khan R., Dai X., 2012, The Astrophysical Journal, 759, 20

Kochanek C. S., Adams S. M., Belczynski K., 2014, MNRAS, 443, 1319

Kochanek C. S., Beacom J. F., Kistler M. D., Prieto J. L., Stanek K. Z., Thompson T. A., Yüksel H., 2008, The Astrophysical Journal, 684, 1336

Koornneef J., 1982, Astronomy and Astrophysics, 107, 247

Koornneef J., 1983, Astronomy and Astrophysics, 128, 84

Kudritzki R., Reimers D., 1978, Astronomy and Astrophysics, 70, 227

Langer N., Maeder A., 1995, A&A, 295, 685

Lennon D. J., Mazzali P. A., Pasian F., Bonifacio P., Castellani V., 1993, Space Sci. Rev., 66, 169

Levesque E., Massey P., Olsen K., Plez B., Maeder A., Meynet G., 2005, in Bulletin of the American Astronomical Society Vol. 37, The physical properties of red supergiants in the magellanic clouds: An abundance of effects. p. 1465

Levesque E. M., Massey P., Olsen K., Plez B., Josselin E., Maeder A., Meynet G., 2005, The Astrophysical Journal, 628, 973

Li C., de Grijs R., Deng L., Milone A. P., 2017, ApJ, 844, 119

Lindegren L., Hernández J., Bombrun A., Klioner S., Bastian U., Ramos-Lerate M., De Torres A., Steidelmüller H., Stephenson C., Hobbs D., et al., 2018, Astronomy & Astrophysics, 616, A2

López Ariste A., Mathias P., Tessore B., Lèbre A., Aurière M., Petit P., Ikhenache N., Josselin E., Morin J., Montargès M., 2018, A&A, 620, A199

Maeder A., 1981, A&A, 102, 401

Maeder A., 1981, Astronomy and Astrophysics, 99, 97

Maeder A., Meynet G., 2003, A&A, 411, 543

Marco A., Negueruela I., 2013, Astronomy & Astrophysics, 552, A92

Marigo P., Girardi L., Bressan A., Groenewegen M. A. T., Silva L., Granato G. L., 2008, A&A, 482, 883

Marino A. F., Villanova S., Piotto G., Milone A. P., Momany Y., Bedin L. R., Medling A. M., 2008, A&A, 490, 625

Marshall J. R., Van Loon J. T., Matsuura M., Wood P. R., Zijlstra A. A., Whitelock P. A., 2004, Monthly Notices of the Royal Astronomical Society, 355, 1348

Massey P., DeGioia-Eastwood K., Waterhouse E., 2001, AJ, 121, 1050

Massey P., Olsen K. A. G., 2003, AJ, 126, 2867

Massey P., Waterhouse E., DeGioia-Eastwood K., 2000, AJ, 119, 2214

Mathis J. S., Rumpl W., Nordsieck K. H., 1977, The Astrophysical Journal, 217, 425

Maund J. R., 2017, MNRAS, 469, 2202

Maund J. R., Fraser M., Ergon M., Pastorello A., Smartt S., Sollerman J., Benetti S., Botticella M.-T., Bufano F., Danziger I., et al., 2011, The Astrophysical Journal Letters, 739, L37

Maund J. R., Fraser M., Smartt S. J., Botticella M., Barbarino C., Childress M., Gal-Yam A., Inserra C., Pignata G., Reichart D., et al., 2013, Monthly Notices of the Royal Astronomical Society: Letters, p. slt017

Mauron N., Josselin E., 2011, Astronomy & Astrophysics, 526, A156

Meixner M., Panuzzo P., Roman-Duval J., Engelbracht C., Babler B., Seale J., Hony S., Montiel E., Sauvage M., Gordon K., et al., 2013, The Astronomical Journal, 146, 62

Messineo M., Habing H., Menten K., Omont A., Sjouwerman L., Bertoldi F., 2005, Astronomy & Astrophysics, 435, 575

Meylan G., Maeder A., 1982, A&A, 108, 148

Meynet G., Chomienne V., Ekström S., Georgy C., Granada A., Groh J., Maeder A., Eggenberger P., Levesque E., Massey P., 2015, Astronomy & Astrophysics, 575, A60

Meynet G., Maeder A., 2000, A&A, 361, 101

Meynet G., Maeder A., 2003, Astronomy & Astrophysics, 404, 975

Meynet G., Maeder A., Schaller G., Schaerer D., Charbonnel C., 1994, A&AS, 103, 97

Milone A., Piotto G., Bedin L., Aparicio A., Anderson J., Sarajedini A., Marino A., Moretti A., Davies M. B., Chaboyer B., et al., 2012, Astronomy & Astrophysics, 540, A16

Moriya T. J., Förster F., Yoon S.-C., Gräfener G., Blinnikov S. I., 2018, MNRAS, 476, 2840

Morozova V., Piro A. L., Valenti S., 2017, The Astrophysical Journal, 838, 28

Negueruela I., González-Fernández C., Dorda R., Marco A., Clark J. S., 2013, EAS Publications Series, 60, 279

Niederhofer F., Georgy C., Bastian N., Ekström S., 2015, MNRAS, 453, 2070

Niederhofer F., Hilker M., Bastian N., Silva-Villa E., 2015, Astronomy & Astrophysics, 575, A62

Nieuwenhuijzen H., De Jager C., 1990, Astronomy and Astrophysics, 231, 134

O'Gorman E., Vlemmings W., Richards A., Baudry A., De Beck E., Decin L., Harper G., Humphreys E., Kervella P., Khouri T., et al., 2015, Astronomy & Astrophysics, 573, L1

Ohnaka K., Driebe T., Hofmann K.-H., Weigelt G., Wittkowski M., 2008, Astronomy & Astrophysics, 484, 371

Olofsson H., 1993, in European Southern Observatory Conference and Workshop Proceedings Vol. 46, Molecular radio line observations of agb-stars, post-agb objects and planetary nebulae. p. 330

Ossenkopf V., Henning T., Mathis J., 1992, Astronomy and Astrophysics, 261, 567

Patrick L., Evans C., Davies B., Kudritzki R., Hénault-Brunet V., Bastian N., Lapenna E., Bergemann M., 2016, Monthly Notices of the Royal Astronomical Society, p. stw561

Paxton B., Bildsten L., Dotter A., Herwig F., Lesaffre P., Timmes F., 2010, The Astrophysical Journal Supplement Series, 192, 3

Paxton B., Cantiello M., Arras P., Bildsten L., Brown E. F., Dotter A., Mankovich C., Montgomery M., Stello D., Timmes F., et al., 2013, The Astrophysical Journal Supplement Series, 208, 4

Paxton B., Marchant P., Schwab J., Bauer E. B., Bildsten L., Cantiello M., Dessart L., Farmer R., Hu H., Langer N., et al., 2015, The Astrophysical Journal Supplement Series, 220, 15

Pickles A., Depagne É., 2010, PASP, 122, 1437

Pietrzyński G., Graczyk D., Gieren W., Thompson I., Pilecki B., Udalski A., Soszyński I., Kozłowski S., Konorski P., Suchomska K., et al., 2013, Nature, 495, 76

Piotto G., Milone A., Bedin L., Anderson J., King I., Marino A., Nardiello D., Aparicio A., Barbuy B., Bellini A., et al., 2015, The Astronomical Journal, 149, 91

Plez B., 2012, Astrophysics Source Code Library, 1, 05004

Price S. D., Egan M. P., Carey S. J., Mizuno D. R., Kuchar T. A., 2001, The Astronomical Journal, 121, 2819

Reimers D., 1975, Memoires of the Societe Royale des Sciences de Liege, 8, 369

Reimers D., 1977, A&A, 61, 217

Reynolds T. M., Fraser M., Gilmore G., 2015, Monthly Notices of the Royal Astronomical Society, 453, 2885

Richards A., Yates J., 1998, Irish Astronomical Journal, 25, 7

Robertson J., 1974, Astronomy and Astrophysics Supplement Series, 15, 261

Sana H., de Mink S. E., de Koter A., Langer N., Evans C. J., Gieles M., Gosset E., Izzard R. G., Le Bouquin J.-B., Schneider F. R. N., 2012, Science, 337, 444

Sandage A., 1984, AJ, 89, 621

Sandage A., Tammann G., 1974, The Astrophysical Journal, 191, 603

Sanner F., 1976, ApJS, 32, 115

Sargent B. A., Srinivasan S., Meixner M., 2011, ApJ, 728, 93

Sargent B. A., Srinivasan S., Meixner M., Kemper F., Tielens A., Speck A., Matsuura M., Bernard J.-P., Hony S., Gordon K. D., et al., 2010, The Astrophysical Journal, 716, 878

Schlegel D. J., Finkbeiner D. P., Davis M., 1998, The Astrophysical Journal, 500, 525

Schneider F. R. N., Izzard R. G., de Mink S. E., Langer N., Stolte A., de Koter A., Gvaramadze V. V., Hußmann B., Liermann A., Sana H., 2014, ApJ, 780, 117

Schneider F. R. N., Izzard R. G., Langer N., de Mink S. E., 2015, ApJ, 805, 20

Schöier F. L., Olofsson H., 2001, A&A, 368, 969

Schutte W., Tielens A., 1989, The Astrophysical Journal, 343, 369

Scicluna P., Siebenmorgen R., Wesson R., Blommaert J., Kasper M., Voshchinnikov N., Wolf S., 2015, Online Material p, 1

Shenoy D., Humphreys R. M., Jones T. J., Marengo M., Gehrz R. D., Helton L. A., Hoffmann W. F., Skemer A. J., Hinz P. M., 2016, The Astronomical Journal, 151, 51

Skrutskie M., Cutri R., Stiening R., Weinberg M., Schneider S., Carpenter J., Beichman C., Capps R., Chester T., Elias J., et al., 2006, The Astronomical Journal, 131, 1163

Smartt S., 2015, Publications of the Astronomical Society of Australia, 32, e016

Smartt S., Eldridge J., Crockett R., Maund J. R., 2009, Monthly Notices of the Royal Astronomical Society, 395, 1409

Smartt S. J., Gilmore G. F., Trentham N., Tout C. A., Frayn C. M., 2001, The Astrophysical Journal Letters, 556, L29

Smartt S. J., Maund J. R., Hendry M. A., Tout C. A., Gilmore G. F., Mattila S., Benn C. R., 2004, Science, 303, 499

Smith N., 2014, Annual Review of Astronomy and Astrophysics, 52, 487

Smith N., Hinkle K. H., Ryde N., 2009, The Astronomical Journal, 137, 3558

Smith N., Humphreys R. M., Davidson K., Gehrz R. D., Schuster M., Krautter J., 2001, The Astronomical Journal, 121, 1111

Smith N., Kilpatrick C. D., Mauerhan J. C., Andrews J. E., Margutti R., Fong W.-F., Graham M. L., Zheng W., Kelly P. L., Filippenko A. V., et al., 2016, Monthly Notices of the Royal Astronomical Society, p. stw3204

Smith N., Li W., Filippenko A. V., Chornock R., 2011, Monthly Notices of the Royal Astronomical Society, 412, 1522

Smith N., Mauerhan J. C., Cenko S. B., Kasliwal M. M., Silverman J. M., Filippenko A. V., Gal-Yam A., Clubb K. I., Graham M. L., Leonard D. C., et al., 2015, Monthly Notices of the Royal Astronomical Society, 449, 1876

Stothers R., 1969, The Astrophysical Journal, 155, 935

Stothers R., Chin C.-W., 1968, ApJ, 152, 225

Stothers R., Chin C.-W., 1978, ApJ, 226, 231

Tang J., Bressan A., Rosenfield P., Slemer A., Marigo P., Girardi L., Bianchi L., 2014, Monthly Notices of the Royal Astronomical Society, 445, 4287

Ueta T., Meixner M., 2003, ApJ, 586, 1338

van den Bergh S., Hagen G. L., 1968, AJ, 73, 569

Van Loon J. T., Cioni M.-R., Zijlstra A. A., Loup C., 2005, Astronomy & Astrophysics, 438, 273

Van Loon J. T., Cohen M., Oliveira J. M., Matsuura M., McDonald I., Sloan G. C., Wood P. R., Zijlstra A. A., 2008, Astronomy & Astrophysics, 487, 1055

Van Loon J. T., Zijlstra A. A., Bujarrabal V., Nyman L.-Å., 2001, Astronomy & Astrophysics, 368, 950

Walker M. F., 1964, AJ, 69, 744

Walmswell J. J., Eldridge J. J., 2012, Monthly Notices of the Royal Astronomical Society, 419, 2054

Werner M., Roellig T., Low F., Rieke G., Rieke M., Hoffmann W., Young E., Houck J., Brandl B., Fazio G., et al., 2004, The Astrophysical Journal Supplement Series, 154, 1

Westerlund B., 1961, The Astronomical Journal, 66, 57

Wilson O. C., 1960, ApJ, 132, 136

Wright E. L., Eisenhardt P. R., Mainzer A. K., Ressler M. E., Cutri R. M., Jarrett T., Kirkpatrick J. D., Padgett D., McMillan R. S., Skrutskie M., et al., 2010, The Astronomical Journal, 140, 1868

Yoon S.-C., Cantiello M., 2010, The Astrophysical Journal Letters, 717, L62

Zahid H. J., Dima G. I., Kudritzki R.-P., Kewley L. J., Geller M. J., Hwang H. S., Silverman J. D., Kashino D., 2014, ApJ, 791, 130

Zaritsky D., Harris J., Thompson I. B., Grebel E. K., 2004, AJ, 128, 1606